WAsP engineering 2000

Mann, J.; Ott, Søren; Jørgensen, B.H.; Frank, H.P.

Publication date:
2002

Document Version
Publisher's PDF, also known as Version of record

Risø–R–1356(EN)

WAsP Engineering 2000

Jakob Mann, Søren Ott, Bo Hoffmann Jørgensen & Helmuth P. Frank

Risø National Laboratory, Roskilde, Denmark
August 2002

Abstract This report summarizes the findings of the EFP project *WAsP Engineering Version 2000*. The main product of this project is the computer program *WAsP Engineering* which is used for the estimation of extreme wind speeds, wind shears, profiles, and turbulence in complex terrain. At the web page `http://www.waspengineering.dk` more information of the program can be obtained and a copy of the manual can be downloaded.

The reports contains a complete description of the turbulence modelling in moderately complex terrain, implemented in *WAsP Engineering*. Also experimental validation of the model together with comparison with spectra from engineering codes is done.

Some shortcomings of the linear flow model LINCOM, which is at the core of WAsP Engineering, is pointed out and modifications to eliminate the problem are presented.

The global database of meteorological "reanalysis" data from NCAP/NCEP are used to estimate the extreme wind climate around Denmark. Among various alternative physical parameters in the database, such as surface winds, wind at various pressure levels or geostrophic winds at various heights, the surface geostrophic wind seems to give the most realistic results. Because of spatial filtering and intermittent temporal sampling the 50 year winds are underestimated by approximately 12%. Whether the method applies to larger areas of the world remains to be seen.

The 50 year winds in Denmark is estimated from data using the flow model in *WAsP Engineering* and the values are approximately 1 m/s larger than previous analysis (Kristensen, Rathmann and Hansen 2000). A tool is developed to estimate crudely an extreme wind climate from a WAsP lib file.

This project was sponsored by the Danish Energy Authority under contract ENS–1363/00–0015.

ISBN 87–550–3094–7; 87–550–3095–5 (Internet)
ISSN 0106–2840

Print: Pitney Bowes Management Services Denmark A/S · 2002

Contents

1 Introduction

Wasp Engineering is a computer program for the estimation of extreme wind speeds, wind shears, profiles, and turbulence in complex terrain. The core algorithms were developed under the project called WAsP Engineering 1.0 DK sponsored by EFP (the Energy Research Programme under the Danish Energy Authority, project number ENS–1363/07–0004, (Mann, Astrup, Kristensen, Rathmann, Madsen and Heathfield 2000)). The ambition was to have a commercially available version ready at the end of the project (end of 1999). However, only a prototype of the program was achieved, and it was not stable and user friendly enough to be distributed.

Funded again by EFP (ENS–1363/00–0015) the work with the computer program continued and WAsP Engineering version 1.0 was finally released July 2001 at the European Wind Energy Conference and Exhibition in Copenhagen (see figure 1). The time from the production of the first prototype to the release of version 1.0, approximately 18 months, was used to reprogram the user interface almost completely, send a beta version out to 10 test users and fix a long list of bugs and installations problems.

Figure 1. The presentation of WAsP Engineering at the Risø stand at EWEC 2001 in the Bella Center, Copenhagen

Now, a year after the release, the program has been sold in almost 40 copies. A revised version (version 1.2) is distributed in August 2002 with a tool to estimate extreme wind climates from a WAsP lib file (see section 5.3 on page 82).

In November 2001 the first WAsP Engineering course was held at Risø (see figure 3 and 4). Many participant had not bought the program in advance, but generally they handled the user interface with ease. Thus we are satisfied with the basic functionality and layout. These courses have been attended by some 20 persons by now.

The next course was held in June 2002 and from both courses we got valuable information on what the users, mainly wind turbine manufactures and consulting engineers, would like in the future. Their wishes can be summaries as

1. A flow model that works in terrain steeper than 25%.
2. Calculation of extreme wind climates from measured time series.
3. Modelling of turbulence in wind turbine wakes.
4. More information on the mathematical models behind WAsP Engineering.

The first point is extraordinary difficult. A not very successful attempt using a atmospheric mesoscale model is presented in section 4. An attempt to improve the applicability of the

Figure 2. Room was sparse at the introduction of WAsP Engineering, June 2001.

Figure 3. Participants from Spain, England, Germany and Japan at the first WAsP Engineering course.

linear flow model is presented in section 3. The second point is indirectly in the Extreme Wind Climate Estimator described in section 5.3. Here the extreme wind climate is estimated from a climate file (a so-called lib file) from WAsP. A better way of doing the estimation would be to go back to the original time series and analyze that. Best strategy for doing this has been considered, although a final implementation into a smoothly running tool has not been completed. We have unfortunately not had sufficient time to develop and implement the third point. The fourth point is taken care of by a complete description of the turbulence modelling in WAsP Engineering is section 2.

In section 2 a complete description of the turbulence modelling in WAsP Engineering is presented. A spectral tensor model of turbulence over flat terrain is discussed in detail with experimental verification and comparison with spectra from engineering codes. Then the model is generalized to moderately complex terrain where the effects of orography and varying roughness is modelled. Finally, the tensor model is used as a basis of the simulation of turbulent fields implemented in WAsP Engineering.

The linear mean flow model currently used in WAsP Engineering has unrealistic flow angles very close to the surface. In section 3 a more correct formulation of the linearized equations is presented, which should improve on these flow angles. Further, new ideas on alternative formulations of the flow equations are presented.

In section 5.1 50 year winds close to Denmark are estimated from the NCEP/NCAR reanalysis data. Winds at 10 m, at the pressure level 850 hPa, and geostrophic winds at 850 hPa, 1000 hPa, and at the sea surface are analyzed. It turns out that the surface geostrophic wind gives most realistic values. At 10 m height the expected extreme wind with a return period of 50 years at the North Sea west of Denmark is 27 $\mathrm{m\,s^{-1}}$, based on the NCEP/NCAR reanalysis data. It is approximately 11 % less than estimates from observations. More research is needed in order to validate the method and see whether the spatial and temporal averaging inherent in the model can be corrected for.

A recalculation of the extreme wind climate based on data is done in section 5.2. Here WAsP Engineering is used instead of WAsP which has been used before (Kristensen et al. 2000). The analysis show that 50 year winds are roughly 1 m/s larger compared with the older analysis. Much of the difference is attributed to the increased roughness of water bodies at high wind speed, which is not modelled in WAsP.

Finally, section 5.3 shows a way to estimate extreme wind climates from WAsP lib files. This has been implemented in WAsP Engineering version 1.2 being released August 2002.

Figure 4. Course participants Felipe Sánchez and Ignacio Martín from Spain discuss WAsP Engineering with the teachers Jakob Mann and Søren Ott.

2 Flat and complex terrain turbulence

For wind turbines dynamic wind loading caused by the atmospheric turbulence is a serious concern for the designer. Knowledge of all three wind components and their spatial correlations are needed because the gusts are 'sampled' in a complicated way by the sweeping blades.

The purpose of this section is to describe a model for the *spectral tensor* of neutral atmospheric surface layer turbulence over flat, homogeneous terrain and the extension of this model to moderately complex terrain. The spectral tensor contains all information on spectra, cross-spectra and coherences, which usually are the input requested by wind turbine designer. Besides being implemented in the computer program WAsP Engineering the model (for flat terrain) is currently being incorporated into the code IEC 61400, which is used widely in the design work of wind turbines.

To model model turbulence over complex terrain is an extremely complicated task. However, in *moderately* complex terrain some of the techniques used for the flat terrain case can be extended. Both the effect of changing roughness and orography on the turbulence is modeled. The model is combined with the simple and fast flow model LINCOM (Astrup, Mikkelsen and Jensen 1997) and included into the software program *WAsP Engineering*.

What happens when the terrain is more than just moderately steep and how steep is that? We do not try to give definite answers to this, only a rule of thumb is given to guide the designer. In order to predict what happens in very steep terrain computationally much more difficult and expensive methods, such as LES (Large Eddy Simulation), must come into play. At present this is according to Wood (2000) too difficult for all but the most simple terrains. In section 4 some very preliminary attacks on the problem of steep terrain is presented.

We also to devise a general algorithm to simulate three-dimensional fields of all three components of the wind velocity fluctuations. Such simulations are particular useful for time domain simulations of gust loading of turbines, and core of the algorithm has been used since 1994 in the Department of Wind Energy at Risø mainly for load calculations on wind turbines with the program HAWC (see http://www.risoe.dk/vea-aed/aeroelas.htm).

In section 2.2 the tensor model for turbulence over flat terrain is presented. Despite the various assumptions and postulates the tensor model only contains three adjustable parameters: a length scale describing the size of the energy containing eddies, a non-dimensional number used in the parametrization of eddy lifetime, and the third parameter is a measure of the energy dissipation. These three parameters are estimated by comparing the model to measurements over flat terrain in section 2.2.5. In section 2.4, 2.5 and 2.6 it is sketched how the flat terrain model is extended to more complex terrain and the limitations are stated. Finally, in section 2.7 the spectral tensor is used in a numerical algorithm to simulate three-dimensional fields of all three components of the wind vector. Some of the material presented here has previously been reported in more detail in Mann (1994), Mann (1998), and Mann (2000).

2.1 Flat terrain turbulence

Definitions The atmospheric turbulent velocity field is denoted by $\tilde{\boldsymbol{u}}(\boldsymbol{x})$, where $\boldsymbol{x} = (x, y, z)$ is a right-handed coordinate system with the x-axis in the direction of the mean wind field and z as the vertical axis. The fluctuations around the mean wind, $\boldsymbol{u}(\boldsymbol{x}) = (u_1, u_2, u_3) = (u, v, w) = \tilde{\boldsymbol{u}}(\boldsymbol{x}) - (U(z), 0, 0)$, are assumed to be homogeneous in space, which is often the case in the horizontal directions but is only a crude approximation in the vertical. Since turbulence over flat terrain at high wind speeds is primarily shear-generated, the mean wind field is allowed to vary as a function of z. Because of

homogeneity, the covariance tensor

$$R_{ij}(\boldsymbol{r}) = \left\langle u_i(\boldsymbol{x}) u_j(\boldsymbol{x}+\boldsymbol{r}) \right\rangle \tag{1}$$

is only a function of the separation vector $\boldsymbol{r}$ ($\langle \quad \rangle$ denotes ensemble averaging).

We shall use *Taylor's frozen turbulence hypothesis* to interpret time series as 'space series' and to serve as a 'dispersion relation' between frequency and wave number (Panofsky and Dutton 1984). Therefore, we can suppress the time argument in $\boldsymbol{u}$.

We only aim at modelling the second order statistics of turbulence, such as variances, cross-spectra, etc. For simulation purposes the velocity field is otherwise assumed to be Gaussian (see section 2.7). It is still not clear how much influence the statistics of third order, such as skewness, has on load calculations.

All second order statistics can be derived from the covariance tensor or its Fourier transform, the spectral tensor:

$$\Phi_{ij}(\boldsymbol{k}) = \frac{1}{(2\pi)^3} \int R_{ij}(\boldsymbol{r}) \exp(-\mathrm{i}\boldsymbol{k}\cdot\boldsymbol{r}) \mathrm{d}\boldsymbol{r}, \tag{2}$$

where $\int \mathrm{d}\boldsymbol{r} \equiv \int_{-\infty}^{\infty}\int_{-\infty}^{\infty}\int_{-\infty}^{\infty} \mathrm{d}r_1\mathrm{d}r_2\mathrm{d}r_3$. The spectral tensor is the basis of the Fourier simulation in section 2.7. The stochastic velocity field can be represented in terms of a generalized stochastic Fourier-Stieltjes integral:

$$\boldsymbol{u}(\boldsymbol{x}) = \int \mathrm{e}^{\mathrm{i}\boldsymbol{k}\cdot\boldsymbol{x}} \mathrm{d}\boldsymbol{Z}(\boldsymbol{k}), \tag{3}$$

where the integration is over all wave number space. The orthogonal process $\boldsymbol{Z}$ is connected to the spectral tensor by

$$\left\langle \mathrm{d}Z_i^*(\boldsymbol{k}) \mathrm{d}Z_j(\boldsymbol{k}) \right\rangle = \Phi_{ij}(\boldsymbol{k}) \mathrm{d}k_1\mathrm{d}k_2\mathrm{d}k_3, \tag{4}$$

which is valid for infinitely small $\mathrm{d}k_i$ and where * denotes complex conjugation (Batchelor 1953).

Is it very difficult to measure the spectral tensor directly. Instead cross-spectra, defined as

$$\chi_{ij}(k_1, \Delta y, \Delta z) = \frac{1}{2\pi} \int_{-\infty}^{\infty} R_{ij}(x, \Delta y, \Delta z) \mathrm{e}^{-\mathrm{i}k_1 x} \mathrm{d}x \tag{5}$$

are often measured, say by two instruments separated by Δy in the horizontal direction perpendicular to the wind and Δz in the vertical, and are used in practical applications. The connection between the components of the spectral tensor and the cross-spectra is

$$\chi_{ij}(k_1, \Delta y, \Delta z) = \int_{-\infty}^{\infty}\int_{-\infty}^{\infty} \Phi_{ij}(\boldsymbol{k}) \mathrm{e}^{\mathrm{i}(k_2\Delta y + k_3 \Delta z)} \mathrm{d}k_2\mathrm{d}k_3. \tag{6}$$

When the two indices i and j are the same and $\Delta y = \Delta z = 0$ (6) becomes the one-point spectrum $F_i(k_1) = \chi_{ii}(k_1, 0, 0)$. This definition implies that spectra are *two-sided*, i.e. we get the variance by integrating from $-\infty$ to ∞.

To distinguish between spectra as functions of wave number k_1 ($= 2\pi f/U$) and frequency f we use F for the former and S for the latter, i.e. $S_i(f)\mathrm{d}f = F_i(k)\mathrm{d}k$.

The *coherence* is defined as

$$\mathrm{coh}_{ij}(k_1, \Delta y, \Delta x) = \frac{|\chi_{ij}(k_1, \Delta y, \Delta z)|^2}{F_i(k_1) F_j(k_1)}. \tag{7}$$

2.2 The 'sheared' spectral tensor for flat terrain

To model the spectral velocity tensor in a shear flow in flat, homogeneous terrain we linearize the Navier-Stokes equation to estimate the effect of the shear on the turbulence. If we assume the shear to be linear such that $\mathrm{d}U/\mathrm{d}z$ is constant, we obtain a simple linear differential equation for the time evolution of the spectral tensor or the 'stretching' of individual eddies. A sketch to guide the imagination of what this means is provided in figure 5.

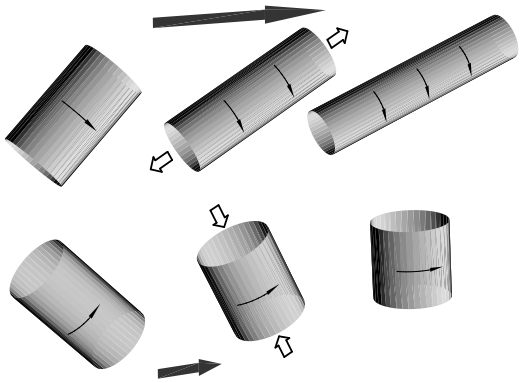

Figure 5. Interpretation of the interplay of shear and turbulence: Two differently oriented eddies are followed over three successive times. Shear stretches (along the axis of rotation) and speeds up the upper eddy while the lower eddy is compressed and slowed down.

2.2.1 Rapid distortion theory

The incompressible Navier-Stokes equation may be written as

$$\frac{\mathrm{D}\boldsymbol{u}}{\mathrm{D}t} + \boldsymbol{u}\cdot\boldsymbol{\nabla}\boldsymbol{U} = -\frac{1}{\rho}\boldsymbol{\nabla}p + \text{non-lin. and viscous terms}, \tag{8}$$

where p is the pressure, and $\mathrm{D}/\mathrm{D}t \equiv \partial/\partial t + \boldsymbol{U}\cdot\boldsymbol{\nabla}$ is the 'average Lagrangian derivative.' Assuming a linear shear ($\boldsymbol{\nabla}\boldsymbol{U}$ constant), taking the curl, and dropping the non-linear and viscous terms we get

$$\frac{\mathrm{D}\boldsymbol{\omega}}{\mathrm{D}t} = \boldsymbol{\Omega}\cdot\boldsymbol{\nabla}\boldsymbol{u} + \boldsymbol{\omega}\cdot\boldsymbol{\nabla}\boldsymbol{U}, \tag{9}$$

where $\boldsymbol{\Omega}$ and $\boldsymbol{\omega}$ are the mean and the fluctuating part of the vorticity. It is not at all clear that this linearization is permissible. For example, it can be shown that if the curl of (8) is used to estimate the change in mean square vorticity the non-linear terms will dominate the linear. However, Hunt and Carruthers (1990) argue that when used for the calculation of the response of velocity fluctuations ($\boldsymbol{u}$ or R_{ij}) to a sudden application of a large scale shearing or straining motion the linearization (9) is valid.

Physically, the last term on the right hand side of (9) may be interpreted as the stretching of vorticity by the mean shear (see figure 5). The first term is a distortion of the mean vorticity by velocity fluctuations.

In order to solve (9) we have to Fourier transform the equation. In order to do so, it is important to notice that wave fronts are advected by the mean flow i.e.

$$\frac{\mathrm{d}\boldsymbol{k}}{\mathrm{d}t} = -(\boldsymbol{\nabla}\boldsymbol{U})\boldsymbol{k}. \tag{10}$$

The solution to this wave front advection equation is

$$\boldsymbol{k}(t) = \exp(-\boldsymbol{\nabla}\boldsymbol{U}t)\boldsymbol{k}_0 \tag{11}$$

where exp means the matrix exponential.

For a general linear $\boldsymbol{U}$ (9) does not have analytic solution. However, for many simple situations such as unidirectional shear, non-rotational stretching or compression, etc. such solutions exists (Townsend 1980).

To get the velocity field from the vorticity we shall express $\mathrm{d}\boldsymbol{Z}$ in terms of $\mathrm{d}\boldsymbol{\Omega}$, which is the Fourier transform of $\boldsymbol{\omega}$ defined in parallel to (3):

$$\boldsymbol{\omega} = \boldsymbol{\nabla}\times\boldsymbol{u} \Rightarrow \mathrm{d}\boldsymbol{\Omega} = \mathrm{i}\boldsymbol{k}\times\mathrm{d}\boldsymbol{Z} \Rightarrow -\mathrm{i}\boldsymbol{k}\times\mathrm{d}\boldsymbol{\Omega} = \boldsymbol{k}\times(\boldsymbol{k}\times\mathrm{d}\boldsymbol{Z}). \tag{12}$$

Because of the general identity $\boldsymbol{A}\times(\boldsymbol{B}\times\boldsymbol{C})=\boldsymbol{B}(\boldsymbol{A}\cdot\boldsymbol{C})-\boldsymbol{C}(\boldsymbol{A}\cdot\boldsymbol{B})$ and that $\boldsymbol{k}\cdot\mathrm{d}\boldsymbol{Z}=0$ we get

$$-\mathrm{i}\boldsymbol{k}\times\mathrm{d}\boldsymbol{\Omega}=-k^2\mathrm{d}\boldsymbol{Z}\Rightarrow\mathrm{d}\boldsymbol{Z}=\mathrm{i}\frac{\boldsymbol{k}\times\mathrm{d}\boldsymbol{\Omega}}{k^2}. \tag{13}$$

We shall rederive (3.11) in Mann (1994), i.e. set up the equations of motion for

$$\boldsymbol{\nabla U}=\begin{pmatrix}0&0&0\\0&0&0\\\frac{\mathrm{d}U}{\mathrm{d}z}&0&0\end{pmatrix}. \tag{14}$$

In this case

$$\boldsymbol{k}(t)=\exp(-\boldsymbol{\nabla U}t)\boldsymbol{k}_0=\begin{pmatrix}1&0&0\\0&1&0\\-\frac{\mathrm{d}U}{\mathrm{d}z}t&0&1\end{pmatrix}\boldsymbol{k}_0, \tag{15}$$

in accordance with (3.13) of Mann, and $\boldsymbol{\Omega}=(0,\mathrm{d}U/\mathrm{d}z,0)$. The equations of motion (9) becomes

$$\frac{\mathrm{D}\boldsymbol{k}\times\mathrm{d}\boldsymbol{Z}}{\mathrm{D}\beta}=k_2\mathrm{d}\boldsymbol{Z}+\begin{pmatrix}\mathrm{d}\Omega_3\\0\\0\end{pmatrix}. \tag{16}$$

Taking the cross product with $\boldsymbol{k}$ and adding $\dot{\boldsymbol{k}}\times(\boldsymbol{k}\times\mathrm{d}\boldsymbol{Z})$ on both sides we get

$$\begin{aligned}-\frac{\mathrm{D}k^2\mathrm{d}\boldsymbol{Z}}{\mathrm{D}\beta}&=\frac{\mathrm{D}\boldsymbol{k}}{\mathrm{D}\beta}\times(\boldsymbol{k}\times\mathrm{d}\boldsymbol{Z})+\boldsymbol{k}\times\frac{\mathrm{D}\boldsymbol{k}\times\mathrm{d}\boldsymbol{Z}}{\mathrm{D}\beta}\\&=\frac{\mathrm{D}\boldsymbol{k}}{\mathrm{D}\beta}\times(\boldsymbol{k}\times\mathrm{d}\boldsymbol{Z})+k_2\boldsymbol{k}\times\mathrm{d}\boldsymbol{Z}+\begin{pmatrix}0\\k_3\\-k_2\end{pmatrix}\mathrm{d}\Omega_3.\end{aligned} \tag{17}$$

Writing this more explicitly we get

$$\frac{\mathrm{D}k^2\mathrm{d}\boldsymbol{Z}}{\mathrm{D}\beta}=\begin{pmatrix}(k_1^2-k_2^2-k_3^2)\mathrm{d}Z_3-2k_1k_3\mathrm{d}Z_1\\2k_1(k_2\mathrm{d}Z_3-k_3\mathrm{d}Z_2)\\0\end{pmatrix} \tag{18}$$

and using $\mathrm{D}k^2/\mathrm{D}\beta=-2k_1k_3$ from (15) this can be shown to be equivalent to (3.11) in Mann (1994).

The differential equations (18) are easily solved given the initial conditions $\boldsymbol{k}(0)=\boldsymbol{k}_0=(k_1,k_2,k_{30})$ and $\mathrm{d}\boldsymbol{Z}(\boldsymbol{k}_0,0)$. Instead of time, t, we shall use the non-dimensional time, β, defined as

$$\beta=\frac{\mathrm{d}U}{\mathrm{d}z}t. \tag{19}$$

The solution to (18) is

$$\mathrm{d}\boldsymbol{Z}(\boldsymbol{k},\beta)=\begin{bmatrix}1&0&\zeta_1\\0&1&\zeta_2\\0&0&k_0^2/k^2\end{bmatrix}\mathrm{d}\boldsymbol{Z}(\boldsymbol{k}_0,0), \tag{20}$$

where

$$\zeta_1=\left[C_1-\frac{k_2}{k_1}C_2\right]\quad,\quad\zeta_2=\left[\frac{k_2}{k_1}C_1+C_2\right] \tag{21}$$

with

$$C_1=\frac{\beta k_1^2(k_0^2-2k_{30}^2+\beta k_1k_{30})}{k^2(k_1^2+k_2^2)} \tag{22}$$

and

$$C_2=\frac{k_2k_0^2}{(k_1^2+k_2^2)^{\frac{3}{2}}}\arctan\left[\frac{\beta k_1(k_1^2+k_2^2)^{\frac{1}{2}}}{k_0^2-k_{30}k_1\beta}\right]. \tag{23}$$

The equations (15) and (20) give the temporal evolution of individual Fourier modes.

2.2.2 RDT and surface layer turbulence

Now we discuss the connection between RDT and stationary surface-layer turbulence, then the key concept of eddy lifetime (section 2.2.3), and finally we combine the different parts to obtain the spectral tensor model (section 2.2.4).

The theory in the previous section describes how turbulence react to a sudden and fast application of a linear shear. It is natural to ask what this has to do with turbulence in the surface layer.

If the initial conditions can be represented by the isotropic von Kármán tensor,

$$\Phi_{ij}(\boldsymbol{k}) = \frac{E(k)}{4\pi k^4}\left(\delta_{ij}k^2 - k_i k_j\right), \tag{24}$$

with the energy spectrum

$$E(k) = \alpha\varepsilon^{\frac{2}{3}}L^{\frac{5}{3}}\frac{(Lk)^4}{(1+(Lk)^2)^{\frac{17}{6}}}, \tag{25}$$

then the tensor $\Phi_{ij}(\boldsymbol{k},t)$ will become more and more 'anisotropic' with time.

The linearization implied by RDT is unrealistic, and at some point (in time) the stretched eddies will break up. We postulate that eddies of linear dimension $\approx |\boldsymbol{k}|^{-1}$ (or more precisely the Fourier modes) are stretched by the shear over a time which is proportional to their lifetime. The lifetime τ is

$$\tau(k) \propto \varepsilon^{-\frac{1}{3}}k^{-\frac{2}{3}} \tag{26}$$

pertaining, at least in the inertial subrange, to eddies with wave vector magnitude $k = |\boldsymbol{k}|$ (Landau & Lifshitz 1987, § 33).

The basic *postulate* is that the *stationary* spectral tensor

$$\Phi_{ij}(\boldsymbol{k}) \equiv \Phi_{ij}\left(\boldsymbol{k},\tau(k)\right) \tag{27}$$

describes the surface layer turbulence well. The combination of RDT and scale dependent eddy lifetimes has previously been used by (Derbyshire and Hunt 1993).

Maxey (1982) has described a similar model with the exception that the lifetime τ was assumed to be constant for all wavevectors. ($\tau \mathrm{d}U/\mathrm{d}z$ is called 'the equilibrium value of the effective distortion strain' by Maxey.) Maxey's model gives a reasonable, but not perfect, description of the ratios between σ_u^2, σ_v^2, σ_w^2 and $\langle uw\rangle$ for turbulent shear flows. There are, however, two grave drawbacks when the model of Maxey (1982) is used to calculate spectra:

1. The uw-cross-spectrum in the inertial subrange decays as $k_1^{-\frac{5}{3}}$ whereas Wyngaard & Coté (1972) observe and give scaling arguments for $k_1^{-\frac{7}{3}}$.
2. For typical values of the effective distortion strain the model predicts $F_u/F_w \approx 7$ in the inertial subrange whereas it should be $F_u/F_w = \frac{3}{4}$.

The model presented here does not suffer from these shortcomings.

2.2.3 Eddy lifetimes

At scales larger than the inertial subrange (26) is not necessarily valid. We construct an alternative model for the 'eddy lifetime' assuming that the destruction of an eddy with size k^{-1} is mainly due to eddies comparable to or smaller than k^{-1}. The characteristic velocity of these eddies may be written as $\left(\int_k^\infty E(p)\mathrm{d}p\right)^{\frac{1}{2}}$, and we simply assume the lifetime to be proportional to the size k^{-1} divided by this velocity:

$$\begin{aligned}\tau(k) &\propto k^{-1}\left(\int_k^\infty E(p)\mathrm{d}p\right)^{-\frac{1}{2}} \\ &\propto k^{-\frac{2}{3}}\left[{}_2F_1\left(\frac{1}{3},\frac{17}{6};\frac{4}{3};-(kL)^{-2}\right)\right]^{-\frac{1}{2}} \propto \begin{cases} k^{-\frac{2}{3}} & \text{for } k\to\infty \\ k^{-1} & \text{for } k\to 0 \end{cases}\end{aligned} \tag{28}$$

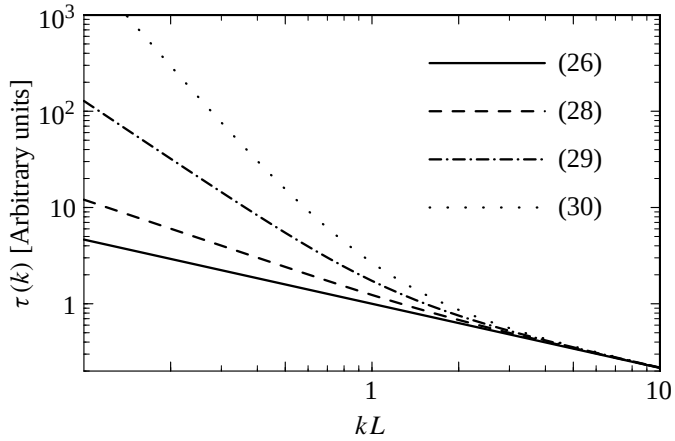

Figure 6. Eddy lifetimes as functions of the magnitude of the wave vector. The lifetimes given by (28) give the most realistic results.

where we have chosen E as the von Kármán energy spectrum (25) and where ${}_2F_1$ is the hypergeometric function.

Comte-Bellot and Corrsin (1971) give another lifetime model which has the right asymptotic behaviour for $k \to \infty$, the 'coherence-destroying diffusion time' :

$$\begin{aligned} \tau_D(k) &\propto k^{-2}\left[\int_k^\infty p^{-2}E(p)\mathrm{d}p\right]^{-\frac{1}{2}} \\ &\propto k^{-\frac{2}{3}}\left[{}_2F_1\left(\frac{4}{3},\frac{17}{6};\frac{7}{3};-(kL)^{-2}\right)\right]^{-\frac{1}{2}} \propto \begin{cases} k^{-\frac{2}{3}} & \text{for } k\to\infty \\ k^{-2} & \text{for } k\to 0 \end{cases} \end{aligned} \tag{29}$$

which was constructed as the square of the eddy size divided by a k-dependent 'turbulent viscosity'.

Further, the inverse 'eddy-damping rate'

$$\tau_E(k) \propto \left(k^3E(k)\right)^{-\frac{1}{2}} \propto \begin{cases} k^{-\frac{2}{3}} & \text{for } k\to\infty \\ k^{-\frac{7}{2}} & \text{for } k\to 0 \end{cases} \tag{30}$$

is used by Lesieur (1987) in eddy-damped quasi-normal theories of turbulence as a characteristic non-linear relaxation time.

All lifetime models are shown in figure 6 normalized such that they coincide in the inertial subrange. It turns out that σ_u^2 becomes infinite using (29) or (30), while (26) and (28) give reasonable results. It also turns out that the spectra calculated from (28) fit the data better than (26) for which reason (28) is used. Some support for (28) may be found in Panofsky, Larko, Lipschutz, Stone, Bradley, Bowen and Højstrup (1982) who measured eddy 'response times' of eddies in the neutral atmospheric surface-layer. Also Kristensen and Kirkegaard (1987) were in their theoretical model of the growth of a puff in a turbulent fluid compelled to use (28) rather than (29) or (30).

It is convenient to write (28) as

$$\tau(k) = \Gamma\left(\frac{\mathrm{d}U}{\mathrm{d}z}\right)^{-1}(kL)^{-\frac{2}{3}}\left[{}_2F_1\left(\frac{1}{3},\frac{17}{6};\frac{4}{3};-(kL)^{-2}\right)\right]^{-\frac{1}{2}}, \tag{31}$$

where Γ is a parameter to be determined. Wilson (1998) has reformulated this expression in terms of the incomplete beta function.

It should be emphasized that at low wavenumbers the assumptions made so far are not valid. F.ex. the assumptions of linear shear is only valid over small distances, i.e. for large

k. Similarly, homogeneity is a dubious assumption for large vertical separations. Finally, despite talking about eddy lifetimes, there is no real modelling of the decay process, because there is no equation describing the non-linear transfer of energy among various wavevectors.

In an attempt to relax the assumption of vertical homogeneity Mann (1994) modelled the influence of the blocking of the surface in addition to shear. This gave slightly better coherence predictions than the present model, but greatly complicated the mathematics and had also other negative consequences.

2.2.4 The uniform shear model

To make a stationary model we use (31) and (27) discussed in section 2.2.2, i.e. we substitute t with τ given by (31). For the 33-component we get

$$\Phi_{33}(\boldsymbol{k}) = \Phi_{33}^{\text{iso}}(\boldsymbol{k}_0)\frac{k_0^4}{k^4} = \frac{E(k_0)}{4\pi k^4}(k_1^2 + k_2^2), \tag{32}$$

where Φ_{33}^{iso} refers to the isotropic von Kármán tensor and E to the energy spectrum (25). The other components become

$$\Phi_{11}(\boldsymbol{k}) = \frac{E(k_0)}{4\pi k_0^4}\left(k_0^2 - k_1^2 - 2k_1k_{30}\zeta_1 + (k_1^2 + k_2^2)\zeta_1^2\right) \tag{33}$$

$$\Phi_{22}(\boldsymbol{k}) = \frac{E(k_0)}{4\pi k_0^4}\left(k_0^2 - k_2^2 - 2k_2k_{30}\zeta_2 + (k_1^2 + k_2^2)\zeta_2^2\right) \tag{34}$$

$$\Phi_{12}(\boldsymbol{k}) = \frac{E(k_0)}{4\pi k_0^4}\left(-k_1k_2 - k_1k_{30}\zeta_2 - k_2k_{30}\zeta_1 + (k_1^2 + k_2^2)\zeta_1\zeta_2\right) \tag{35}$$

$$\Phi_{13}(\boldsymbol{k}) = \frac{E(k_0)}{4\pi k_0^2k^2}\left(-k_1k_{30} + (k_1^2 + k_2^2)\zeta_1\right) \tag{36}$$

and

$$\Phi_{23}(\boldsymbol{k}) = \frac{E(k_0)}{4\pi k_0^2k^2}\left(-k_2k_{30} + (k_1^2 + k_2^2)\zeta_2\right). \tag{37}$$

The equations (32) to (37) with (31) constitute the Uniform Shear model (US).

These equations have two differences from the expressions of Townsend (1976) for plane shearing of homogeneous turbulence. The first is the elimination of time by (31) and the second and related difference is that we do not use the turbulent viscosity of Townsend, which would make the decay time for all eddies equal, independent of their sizes.

2.2.5 Fitting spectra to observations

First the uncertainties on estimated spectra are discussed. These are either caused by variations in atmospheric stability, which persists evern at high wind speeds ($>$ 16 m/s) over water, or by statistical variations. Secondly, the measured neutral spectra are fitted to the spectral tensor model. Based on this fit the coherences are finally predicted and compared to the measurements.

Uncertainties on spectra Often raw spectral estimates are averaged over, say, n consecutive frequencies or wavenumbers to decrease the random error of the estimate (Bendat and Piersol 1986). Alternatively, the time series could be divided into n segments of equal duration. Each segment is then Fourier transformed and the spectrum determined as the average of the absolute square of these Fourier transforms. For either definition the statistical uncertainty on spectral density F calculated from a stationary time series is (under the assumption that the time series is long compared to the time scale of the process)

$$\frac{\sigma(F)}{\langle F\rangle} = \frac{1}{n^{\frac{1}{2}}} \tag{38}$$

(Koopmans 1974, Bendat and Piersol 1986).

Figure 7 shows the result of an analysis of 22 two-hour time series from the Great Belt (see also table 2 on page 30). The series have mean speeds U between 16 and 20 m/s and the mean directions are within a narrow range around South where there is an uninterrupted fetch over water for at least 20 km.

Assuming the stability to be neutral, the variation of spectral densities should obey (38) and the standard deviation at the lowest wavenumbers should be around 25% and 5% at $k_1 = 0.1$ m^{-1}. The observed rms variations are clearly larger, at least 50% at the lowest frequencies and maybe 20% at higher frequencies. Most noticeably, there are spectra with only 10% of the spectral density of the others.

This variation is due to the stability of the atmosphere not being neutral. The case with suppressed turbulence is slightly stable and has $U = 16$ m/s.

Unstable stratification also alters the spectrum. Though none of the spectra from the Great Belt are obtained under very unstable situations, an analysis of unstable, high-wind spectra on the west coast of Norway indicate that the spectra are mainly enhanced (by more than 100%) at *very* low frequencies ($f < 0.02$ Hz). These might be relevant for various off-shore production units (Mann 1992).

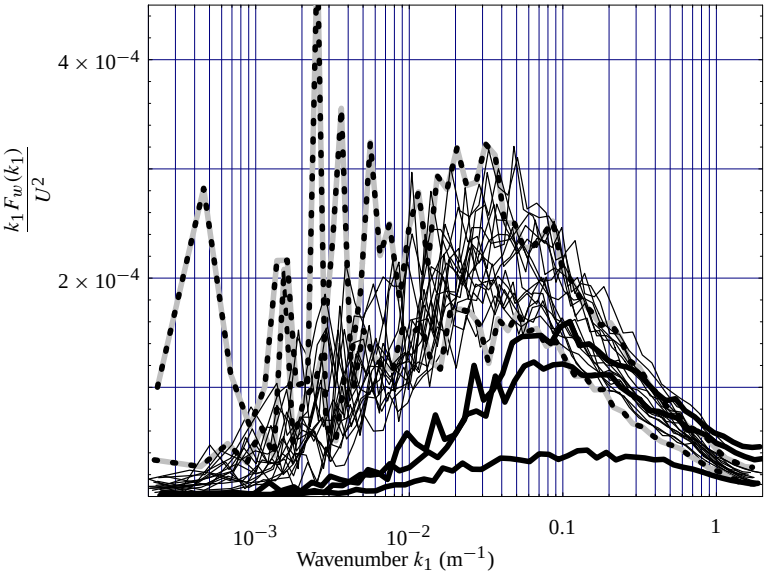

Figure 7. Spectra of w from the Great Belt Coherence Experiment. Mean wind speeds are between 16 and 20 m/s and directions are in a narrow interval around the South (see table 2 on page 30 for a definition of the interval). Dashed spectra have slightly unstable stratification, gray have stable, and the thin have neutral.

2.2.6 Spectral fitting and prediction of coherences

In order to conduct simultaneous measurements of spectra and coherence over the sea a 70 m high mast was erected 40 m from an existing mast on the easterly spit of Sprogø, an island in the midst of the Great Belt separating the two Danish islands Funen and Zealand. A 15 m long horizontal boom was mounted symmetrically at the top of the new mast so that the whole construction has the form of a letter "T". A Kaijo-Denki DAT-300 omni-directional sonic anemometer was installed at each end of the boom and at the top of the old mast, providing 15.0, 32.5 and 47.5 m horizontal separations between the three co-linear instruments. The mast array is shown in figure 9. More details about the experiment including correction for flow distortion by the sonic anemometers may be

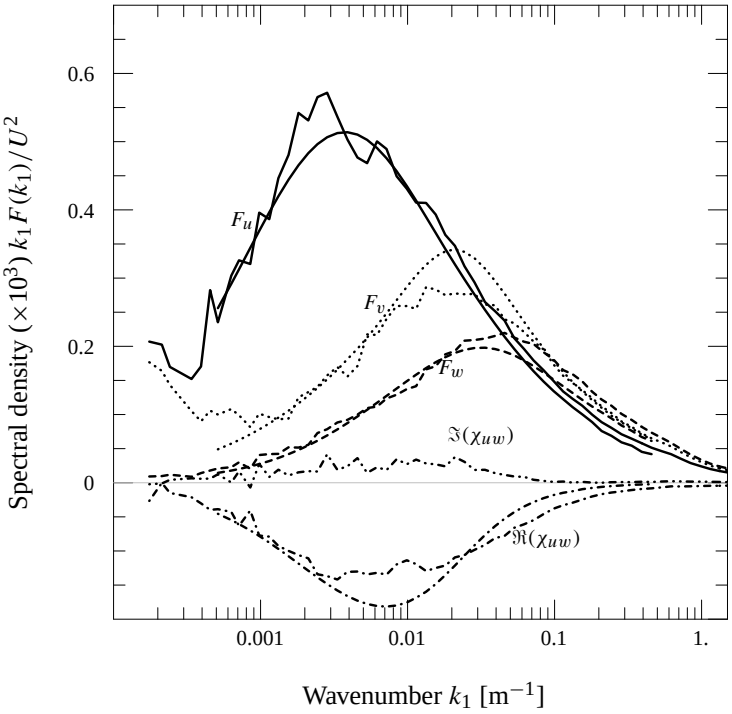

Figure 8. Average u-, v-, w-, and cross-spectra of all the neutral *runs present in figure 7. The ragged curves are meansurements while the smooth are the model spectra. The model has zero imaginary part of the cross-spectrum (quadrature spectrum).*

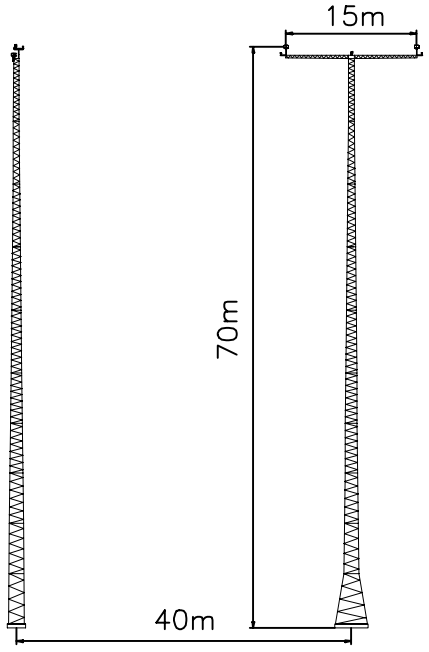

Figure 9. The mast array on Sprogø viewed from SSE. The tiny dots at the top of the masts are the omni-directional sonic anemometers.

found in (Mann, Kristensen and Courtney 1991).

The measured spectra shown in figure 8 are an average of 16 *neutral* two hour runs with wind speeds between 16 and 20 m/s. The smooth curves are model spectra derived from the spectral tensor model, (32) — (37), with the parameters $\Gamma = 3.2$, $L = 61$ m, and $\alpha\varepsilon^{2/3}/U^2 = 1.810^{-4}$ m$^{-2/3}$, which are taken from Mann (1994), who used fewer two hour runs but slightly higher wind speeds.

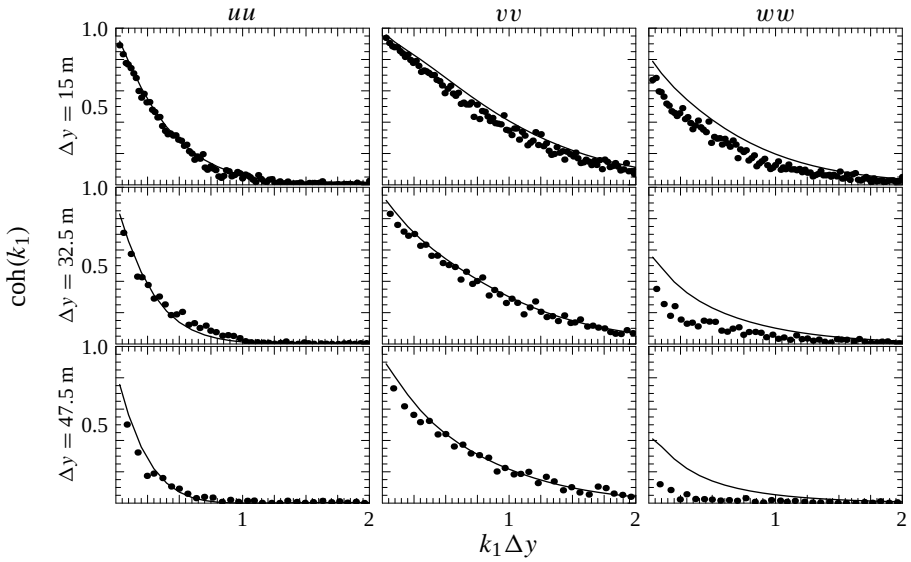

Figure 10. The dots are measured coherences from the same set of data as used for figure 8 for various horizontal separations Δy and for all three velocity components. The lines are the coherences predicted by the model.

These parameters are in turn used to predict the coherences through (6), (7) and (32) — (37) as shown in figure 10. As seen from this figure the predictions agree well with the measurements except for the w coherence, especially at the largest separation.

2.3 Parameters from code spectra

Here we compare the tensor model of section 2.2 to spectra and coherences from the literature. We will not give an exhaustive review of spectral models but select a few modern models which the author believes is used in wind engineering. The purpose is to estimate the parameters Γ, L and $\alpha\varepsilon^{2/3}$ for a given mean wind speed U and height above the water surface z.

The logarithmic mean wind profile defines the roughness length:

$$U(z) = \frac{u_*}{\kappa}\ln(z/z_0), \tag{39}$$

where $u_* \equiv (-\langle uw\rangle)^{1/2}_{z\to 0}$ is the friction velocity and $\kappa = 0.40$ the von Kármán constant (Landau and Lifshitz 1987, Panofsky and Dutton 1984).

ESDU International (1982) gives a slightly more accurate wind profile:

$$U(z) = \frac{u_*}{\kappa}\left(\ln(z/z_0) + 34.5 f z/u_*\right) \tag{40}$$

with the Coriolis parameter $f \equiv 2\Omega\sin\phi$, where Ω is the angular velocity in rad s^{-1} of the Earth and ϕ the geographical latitude. The profile (40) is valid up to $z = 300$ m, below 30 m (39) is a good approximation to (40). Throughout this comparison we use $f = 10^{-4}$ s^{-1}.

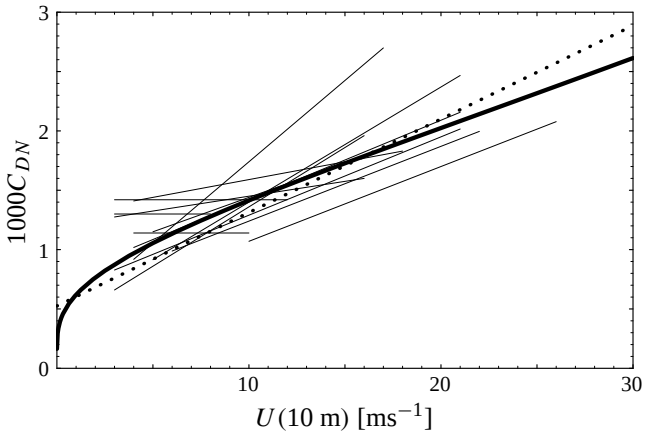

Figure 11. The neutral drag coefficient C_{DN} as a function of mean wind speed at $z = 10$ m. The broad line is from Charnock's relation (41) and (39). The thin lines are empirical relations from (Geernaert 1987) and the dotted line is from NDP (1998), see (50).

Charnock (1955) argued that over the sea the roughness length is related to $g = 9.8\ \text{ms}^{-2}$ the acceleration due to gravity and the friction velocity by

$$z_0 = A\frac{u_*^2}{g} \tag{41}$$

where A, the Charnock constant, must be determined experimentally. On basis of an extensive literature study of ocean data Garratt (1977) found that the best fit of (41) is $A = 0.0144$. A slightly newer value is given by ESDU International (1982):

$$A = 0.0167, \tag{42}$$

which will be used here. Over the ocean the neutral drag coefficient

$$C_{DN} = \left(\frac{u_*}{U(10\text{ m})}\right)^2 \tag{43}$$

increases monotonicly with U as can be seen by solving (41) and (39). This is shown in figure 11 as a broad line together with several recent empirical relations. The figure gives a good impression of the uncertainty in estimates of drag coefficients. Among the various reasons for this variability are atmospheric stability, surface currents, 'wave age', length of the fetch over water, and water depth (Garratt 1977, Geernaert 1987, Brown and Swail 1991). The spectral density of velocity fluctuations is in general proportional to the drag coefficient so the uncertainty of the former is probably of the same order of the latter.

2.3.1 Code and textbook spectra

Surface layer scaling is used in many spectral models, implying that length scales are proportional to z and that variances are proportional to u_*^2. Therefore, it is convenient to normalize the spectra with u_*^2 and present them as functions of either $n \equiv fz/U$ or $k_1 z$.

The spectra of Kaimal are (Kaimal, Wyngaard, Izumi and Coté 1972, Kaimal and Finnigan 1994)

$$\frac{fS_u(f)}{u_*^2} = \frac{k_1 F_u(k_1)}{u_*^2} = \frac{52.5n}{(1+33n)^{5/3}}, \tag{44}$$

$$\frac{fS_v(f)}{u_*^2} = \frac{8.5n}{(1+9.5n)^{5/3}}, \tag{45}$$

and

$$\frac{fS_w(f)}{u_*^2} = \frac{1.05n}{1+5.3n^{5/3}}. \tag{46}$$

Kaimal's spectra are based on measurements over flat homogeneous terrain in Kansas.

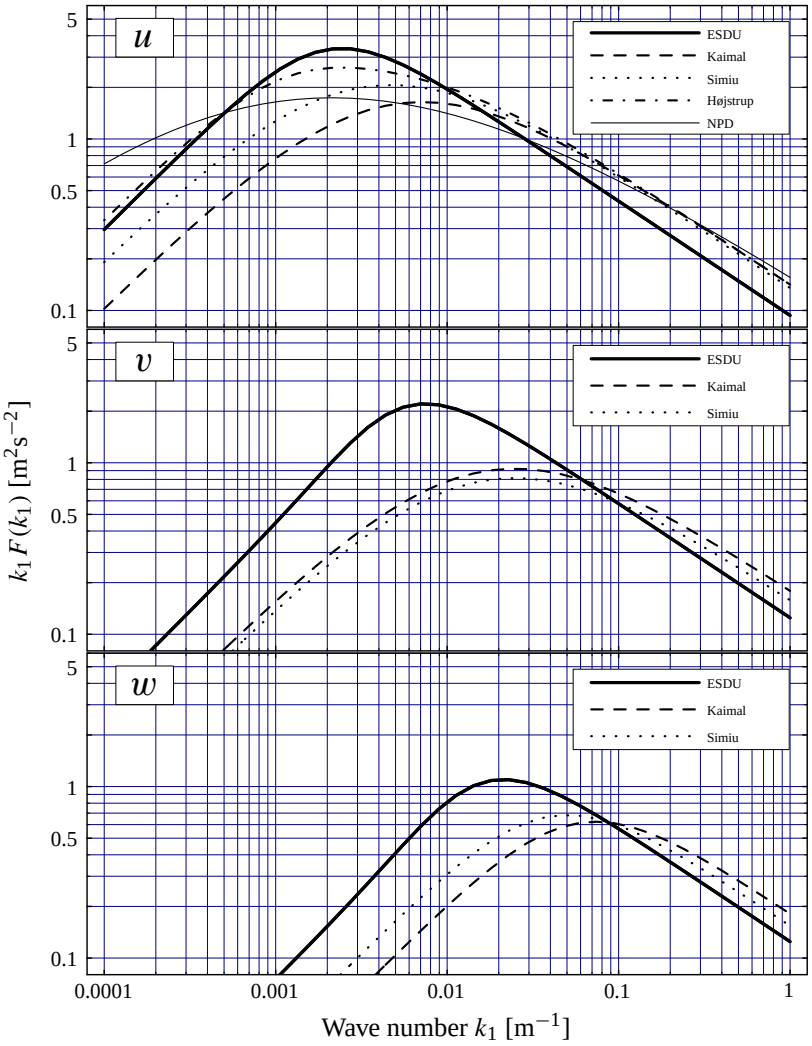

Figure 12. Comparison of spectral models. For the comparison $z = 40$ m and $U = 40$ m/s (over the sea) is chosen. For u ESDU International (1985), (44), (47), (57), (53) are used. For v and w ESDU International (1985), (45) and (48), and ESDU International (1985), (46) and (49), respectively. Eq. (40) together with (41) gives $u_* = 1.78$ m/s and $z_0 = 0.0054$ m.

The spectra of Simiu and Scanlan (1996) have the same functional shapes as Kaimal's but the numerical constants are different:

$$\frac{fS_u(f)}{u_*^2} = \frac{100n}{(1+50n)^{5/3}}, \tag{47}$$

$$\frac{fS_v(f)}{u_*^2} = \frac{7.5n}{(1+9.5n)^{5/3}}, \tag{48}$$

and

$$\frac{fS_w(f)}{u_*^2} = \frac{1.68n}{1+10n^{5/3}}. \tag{49}$$

Deviations from surface layer scaling are found in the model spectra from ESDU International (1985). Also the spectra of Norwegian Petroleum Directorate (NDP 1998) and Højstrup, Larsen and Madsen (1990) do not obey surface layer scaling, but they are only limited to u-spectra.

The Engineering Science Data Unit (ESDU) wind profile, spectra and coherences (ESDU International, 1982, 1985 and 1986) are derived from many sources from all over the world during several decades. ESDU proposes that the turbulence intensities and length scales in the surface layer are dependent on mean wind speed. The argument is that the boundary layer depth increases with increasing wind speed implying larger scales of the turbulence. The other models, relying on surface layer scaling do not contain any information on the boundary layer depth and they contain no explicit reference to the mean wind speed. The equations of ESDU are, compared to all other spectral models discussed here, by far the most complicated. Therefore we shall not cite them explicitly. The most important input parameters are, as for the other spectral models, the height above the surface z, and the mean wind speed at some height. Of less important input is the Coriolis parameter which, as mentioned previously, is taken to be $f = 10^{-4}\ \mathrm{s}^{-1}$. The models we use are valid for the neutral atmosphere.

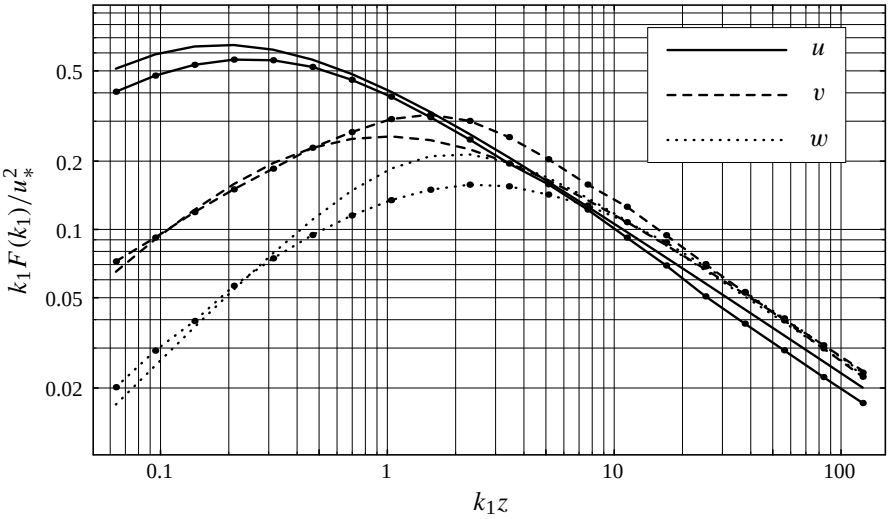

Figure 13. The 'sheared spectral tensor' of section 2.2 (curves with dots) fitted to the models by Simiu and Scanlan (47) – (49). The result is given by (60).

The u-spectrum of NDP (1998) applies to winds over oceans and assumes the drag coefficient to be

$$C_{DN} = 0.525 \times 10^{-3}(1 + 0.15U_{10}), \tag{50}$$

see figure 11. Integrating $\mathrm{d}U/\mathrm{d}z = u_*/(\kappa z) = \sqrt{C_{DN}}U_{10}/(\kappa z)$ (50) implies that

$$U(z) = U_{10}\left(1 + C\ln\frac{z}{10\ \mathrm{m}}\right) \tag{51}$$

with

$$C = 0.0573(1 + 0.15U_{10})^{1/2} \tag{52}$$

where U_{10} has to be measured in meters per second. While discussing the NPD spectrum we also assume the unit of z to be meter, f is Hz and S_u is $\mathrm{m}^2\mathrm{s}^{-2}\mathrm{Hz}^{-1}$. The spectral density of the longitudinal wind component is

$$S_u(f) = \frac{160\left(\frac{U_{10}}{10}\right)^2\left(\frac{z}{10}\right)^{0.45}}{\left(1 + \tilde{f}^n\right)^{\frac{5}{3n}}} \tag{53}$$

with

$$\tilde{f} = 172f\left(\frac{z}{10}\right)^{2/3}\left(\frac{U_{10}}{10}\right)^{-3/4} \tag{54}$$

and $n = 0.468$. This spectrum implies that the variance

$$\sigma_u^2 = 0.00309 \frac{U_{10}^{2.75}}{z^{0.217}} \tag{55}$$

will decrease with height and not constant as implied by surface layer scaling. Furthermore, the integral length scale

$$\text{length scale} \propto z^{2/3} U_{10}^{1/4} \tag{56}$$

will not be proportional with height but will grow somewhat slower and it will also increase a little with wind speed. This is not consistent with surface layer scaling where it under neutral conditions is constant with wind speed.

Højstrup et al. (1990) suggested that spectra at low frequencies do not obey surface layer scaling because the low frequency part scales with the height of the boundary layer, not z. To verify their model they used data selected for neutrality and high wind speeds ($11 < U < 23$ ms^{-1}) from both over sea and land sites in Denmark. The u-model is[1]

$$\frac{f S_u(f)}{u_*^2} = \left(\frac{2.5 n_t}{1 + 2.2 n_t^{5/3}} + \frac{52.5 n}{(1 + 33n)^{5/3}} \right) \frac{1}{1 + 7.4(z/A)^{2/3}} \tag{57}$$

where the 'neutral length scale' $A = 3000$ m and $n_t = fA/U$. The second term in the parenthesis is the Kaimal spectrum (44).

All spectral model are compared in figure 12 for a specific choice of U and z. Generally, ESDU has larger length scales compared to those by Kaimal and by Simiu & Scanlan, which are similar. NPD and Højstrup support ESDU's large u-scale. ESDU, though, has the most peaked spectra and, at high wave numbers, slightly lower spectral densities. All spectra agree fairly well at high wave numbers but have substantial scatter at low wave numbers.

2.3.2 Comparison with the spectral tensor model

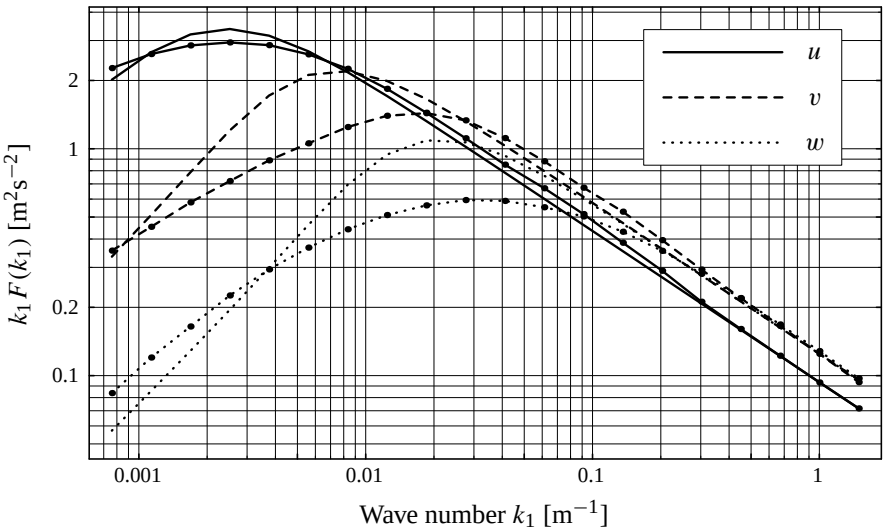

Figure 14. Example with $z = 40$ m and $U = 40$ m/s of the fit of the spectral tensor model (curves with dots) to the ESDU models.

Here we fit the spectral tensor of section 2.2 to models that describe all three component spectra, namely the ones by Kaimal, Simiu & Scanlan and ESDU.

[1] Højstrup, Larsen and Madsen (1990) also gives a model for the v spectrum, but it was never compared with data, so it will not be discussed here.

We obtain the parameters Γ, L and $\alpha\varepsilon^{2/3}$ by making a simultaneous least squares fit to the u-, v- and w-model spectra for wave numbers in the range $0.05 < k_1 L < 100$. For the Kaimal spectra we get

$$\begin{aligned} \Gamma &= 3.9 \\ L &= 0.59z \\ \alpha\varepsilon^{2/3} &= 3.2\frac{u_*^2}{z^{2/3}}, \end{aligned} \tag{58}$$

where the dependence on z is a consequence of surface layer scaling. For the Simiu & Scanlan spectra, where the fir is shown in figure 13, we get

$$\begin{aligned} \Gamma &= 3.8 \\ L &= 0.79z \\ \alpha\varepsilon^{2/3} &= 2.8\frac{u_*^2}{z^{2/3}} \end{aligned} \tag{59}$$

and for both models u_* can be obtained from figure 11.

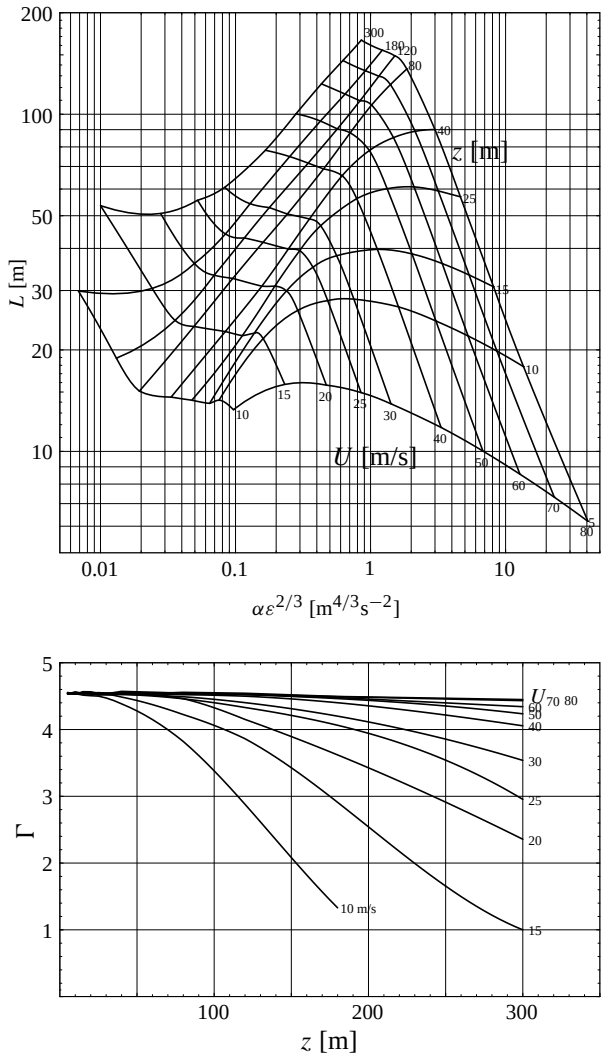

Figure 15. The parameters of the spectral tensor model derived from fits to the ESDU model spectra for turbulence over the sea. Given U and z, all three parameters can be extracted from these plots.

It is more complicated to get the parameters from the ESDU models because the spectra no longer depend on U and z in a simple way. For each set $\{U, z\}$, a fit to the tensor model has to be calculated. We do that on a mesh limited by $10 < U < 80$ m/s, $5 < z < 300$ m over the sea. The result is shown in figure 15. As an example of use of these graphs, suppose that the parameters for $U(z = 80\text{ m}) = 20$ m/s are wanted. From the upper plot of figure 15 we get $L = 33$ m and $\alpha\varepsilon^{2/3} = 0.1\ \text{m}^{4/3}\text{s}^{-2}$. The lower plot gives $\Gamma = 4.5$.

Table 1. Parameters of the spectral tensor derived from different sources for $U(40\ m) = 40$ m/s at sea.

	Γ	L [m]	$\alpha\varepsilon^{2/3}$ [$\text{m}^{4/3}\text{s}^{-2}$]
Great Belt	3.2	35	0.79
Kaimal	3.9	24	0.86
Simiu	3.8	31	0.76
ESDU	4.5	66	0.62

Another example is shown in table 1 where the Great Belt data from (Mann 1994) are extrapolated using neutral surface layer scaling to $U(40\text{ m}) = 40$ m/s. The spectral fit for these values of U and z is shown in figure 14.

Literature coherences and coherences derived from the spectral tensor by (6) and (7) are compared in Mann (1998). Generally, the agreement is good.

In WAsP Engineering the spectral tensor for flat terrain is used as basis for the modeling of turbulence in moderately complex terrain as described in the following sections. The three different ways to estimate the parameters of the tensor in flat terrain (eqs. (59), (60) or from the ESDU) are all implemented and may be chosen by the user.

2.4 Turbulence in complex terrain

As indicated in the previous sections a lot is known about turbulence over flat terrain. The purpose of this section, section 2.5 and 2.6 is to describe models that take into account the influence of roughness changes and gentle hills on the turbulence statistics. The turbulence model used input from the mean flow model LINCOM and is implemented in the computer program WAsP Engineering. The following text is largely based on Mann (2000).

The modeling of the turbulence structure is divided into two parts: Roughness variations and orography. For the second rapid distortion theory (RDT) is used. Effects of both on the turbulence are treated as perturbations to the homogeneous terrain turbulence model of section 2.2. The model is restricted to neutral atmospheric stratification, which may be a severe restriction sites close to the sea and at large heights above the surface.

The modeling of the change of turbulence due to orography is limited to the so-called outer layer. For a simple isolated hill the height of the inner layer is estimated by

$$\frac{\ell}{L}\ln^2\left(\frac{\ell}{z_0}\right) = 2\kappa^2, \tag{60}$$

where z_0 is the roughness length, L the upwind distance where the elevation is half the hill height and $\kappa \approx 0.4$ the von Kármán constant (Jensen, Petersen and Troen 1984). At heights lower than ℓ there is approximately local equilibrium between production and dissipation of turbulent kinetic energy, and above ℓ the perturbations caused by the hill are approximately inviscid. The inner layer height is also approximately equal to the height above which the travel time over the hill is shorter than the Lagrangian time scale or the eddy 'turn-over' time scale.

Inner scales derived from (60) compare well with measurements from Askervein (Walmsley and Taylor 1996). With $L = 100$ m and $z_0 = 0.03$ m (60) gives $\ell = 2$ m, $\ell = 4$ m with

$L = 100$ m, $z_0 = 0.3$ m, and $\ell = 10$ m with $L = 1000$ m, $z_0 = 0.03$ m. The lower limit of the applicability of the model depends thus on the terrain.

The modeling of turbulence changes due to roughness variations does not have this limitation, and should apply all the way down to the roughness sub-layer which is very close to the ground. The flow disturbances produced by roughness changes are by nature viscous and thus much "slower" than RDT. We use and modify the idea that eddies respond to roughness changes on the order of "the eddy turn-over time scale" (Panofsky et al. 1982, Højstrup 1981). A consequence of this is that the low frequency end of the spectrum responds very slowly to roughness changes while small eddies quickly become in equilibrium with the underlying surface.

Releted work may be found in Frank (1996), which considers spectra over a single hill with constant roughness.

The basic limitation of the model is embodied in the following rule of thumb:

> *If there are extended areas within a radius of 3 to 4 km from the site of interest with slopes of more than 20° to 25°, then turbulence may be much larger than calculated. In this situation measurements at the site may be required.*

2.4.1 The linear flow model LINCOM

Within the concept of linearized flow models originally introduced by Jackson and Hunt (1975), Troen and de Baas (1986) developed a relatively simple model for neutrally stable flow over hilly terrain. The model was later named LINCOM, an acronym for LINearized COMputation. The base of this version of the code, giving the influence of the topography on the flow of a neutrally stratified atmosphere, has been extended with a model for the influence of varying surface roughness also over water (Astrup et al. 1997, Astrup and Larsen 1999, Astrup, Larsen, Rathmann and Madsen 1999). Later the model has been extended to calculate spatial derivatives of the mean wind field, such as the vertical shear $\partial U/\partial z$, which is used in the turbulence modeling.

LINCOM is based on an analytical solution in Fourier space to a set of linear equations derived from the normal nonlinear mass- and momentum equations for incompressible fluid flows. The linear equations describe the perturbations in velocity and pressure which the real terrain induces in an equilibrium flow corresponding to a flat terrain with uniform surface roughness. The perturbations caused by horizontal gradients in ground elevation and surface roughness are determined separately and added as a first order approximation to the combined perturbation.

In section 3 some unwanted properties of the LINCOM flow model are resolved, but not yet implemented in WAsP Engineering, and thoughts on the further development of linearized flow models are presented.

2.4.2 Nomenclature

The instantaneous wind speed as a function of space and time $\tilde{\boldsymbol{U}} = \tilde{\boldsymbol{U}}(\boldsymbol{x}, t)$ is decomposed into the ensemble mean and fluctuations:

$$\tilde{\boldsymbol{U}} = \boldsymbol{U} + \boldsymbol{u}, \tag{61}$$

$U \equiv |\boldsymbol{U}|$. The unperturbed stationary velocity field is denoted by $\boldsymbol{U}^0$ and is only dependent on the height above the surface z. The unperturbed fluctuations are denoted by $\boldsymbol{u}^0$.

The correlation and spectral tensors $R_{ij}(\boldsymbol{r})$ and $\Phi_{ij}(\boldsymbol{k})$ are defined by (1) on page 9 and (2). However, it should be noted that the turbulence is not homogeneous, not even in the horizontal directions, so the tensors are meant as approximations to the real inhomogeneous correlation structure. The corresponding unperturbed tensors which equal those for flat terrain have a superscript 0.

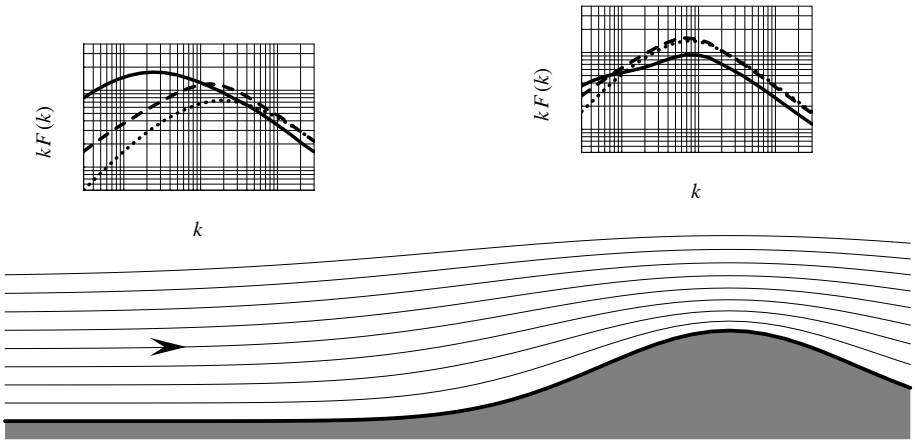

Figure 16. Qualitative sketch of the action of a ridge on the turbulence according to the RDT model. The fluctuations in the u-component of the turbulence are attenuated, as seen from the u-spectrum (solid curve), the v-fluctuations are not changed much (dashed curve), while the w-fluctuations are amplified (dotted curve).

Since the flow model LINCOM is linear the perturbation to the mean flow can be written as a sum of two terms

$$\boldsymbol{U} - \boldsymbol{U}^0 = \boldsymbol{U}^r + \boldsymbol{U}^t, \tag{62}$$

where $\boldsymbol{U}^r$ refers to flow perturbations due to roughness variation and $\boldsymbol{U}^t$ due to variations in the height of the terrain.

2.5 Variable roughness

Højstrup's model concerning the adjustment of velocity spectra downstream of an abrupt change of roughness is the starting point of a more general model for the spectral tensor downstream of any slowly varying or abrupt change of roughness (Højstrup 1981).

2.5.1 Outline of the model by Højstrup

In the special case of neutral stability, which is the only concern here, it is assumed in Højstrup (1981) that the height z^{top} separating air which has or has not felt the abrupt change of roughness is governed by the differential equation:

$$\frac{\mathrm{d}z^{\text{top}}}{\mathrm{d}x} = D\frac{\sigma_w}{U} = D\frac{\kappa 1.22}{\log(z^{\text{top}}/z_0)}, \tag{63}$$

where z_0 refers to the downstream value of the roughness and D is a constant of the order of one. Figure 17 shows z^{top} for a landscape with an abrupt change of roughness for every 12.5 km together with the mean flow field calculated by LINCOM.

When an eddy hits the upper edge of this internal boundary layer its energy is supposed to change according to

$$\frac{\mathrm{d}E_e(k_1)}{\mathrm{d}t} = \frac{E_{e2}(k_1) - E_e(k_1)}{\tau(k_1)}, \tag{64}$$

where $E_e(k_1)$ the energy of the eddy with wavenumber k_1 and $E_{e2}(k_1)$ is the energy the eddy would have had being above a homogeneous surface having the downstream roughness.

Comparison of eddy time scales in the two models In the equation for the change of energy (64) above the time scale τ has to be determined. This 'eddy time scale' is in Højstrup written as

$$\tau(k_1) = A\frac{2\pi}{k_1\sqrt{E_e(k_1)}} \tag{65}$$

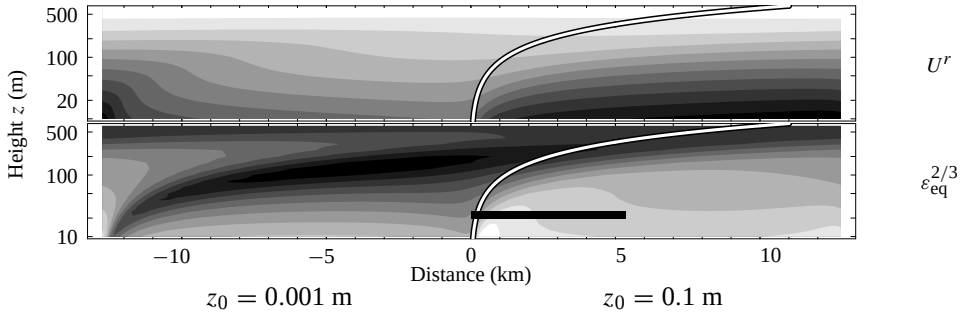

Figure 17. The mean velocity field U^r due to an abrupt change of roughness according to LINCOM (top, darker means lower values). Lower plot: Expected intensity of small scale turbulence according to (71). White lines: Internal boundary layer according to (Højstrup 1981). Spectra shown in figure 18 are calculated along the black horizontal line.

with $A = 0.13$ and $E_e(k_1) \equiv k_1 F_u(k_1)$, where F_u is the spectrum of fluctuations in the direction of the mean wind. In the inertial subrange he estimates the eddy time scale to be $\tau(k_1) = B\alpha_1 \varepsilon^{-1/3} k_1^{-2/3}$ with $B = 2.3$. Since the Kolmogorov constant for the one-dimensional spectrum $\alpha_1 \approx 0.5$, the time scale of Højstrup is in inertial subrange

$$\tau(k_1) = C_1 \varepsilon^{-1/3} k_1^{-2/3} \quad \text{with} \quad C_1 = 1.15. \tag{66}$$

The time scale discussed in section 2.2.3 is a function of $k = |\boldsymbol{k}|$ and in the inertial subrange it is

$$\tau(k) = C\varepsilon^{-1/3} k^{-2/3} \tag{67}$$

with $C = 1.8$ in the Great Belt Experiment and 1.5 in the Lammefjord Experiment (Mann 1994). In order to relate these two constants C and C_1 in the inertial subrange we assume that $\tau(k_1)$ can be expressed as an weighted average of $\tau(k)$ over all wavevectors that contribute to the energy at the horizontal wavenumber k_1:

$$\tau(k_1) = \frac{\int \Phi_{ii}(\boldsymbol{k})\tau(k)\mathrm{d}\boldsymbol{k}_\perp}{\int \Phi_{ii}(\boldsymbol{k})\mathrm{d}\boldsymbol{k}_\perp} = C\varepsilon^{1/3}\frac{5}{7}k_1^{-2/3} \tag{68}$$

where $\int \mathrm{d}\boldsymbol{k}_\perp$ means $\int_{-\infty}^{\infty}\int_{-\infty}^{\infty} \mathrm{d}k_2\mathrm{d}k_3$ and summation over repeated indices is assumed, so

$$C = \frac{7}{5}C_1 \tag{69}$$

implying that $C = 1.61$ for the data analysed by Højstrup. So, even though the eddy time scales of (Højstrup 1981) and (Mann 1994) appear in different contexts they are of comparable magnitude.

At smaller wavenumbers outside the inertial subrange both models behave asymptotically as $\tau \propto k^{-1}$.

2.5.2 Spectral tensor model: Roughness

As a generalization of (64) we propose that the three-dimensional spectral energy density (or the spectral tensor) approaches some equilibrium spectral tensor $\Phi_{ij}^{\rm eq}$ according to the equation

$$\frac{\mathrm{d}}{\mathrm{d}t}\Phi_{ij}(\boldsymbol{k}) = \frac{\Phi_{ij}^{\rm eq}(\boldsymbol{k}) - \Phi_{ij}(\boldsymbol{k})}{\tau(k)}, \tag{70}$$

where $\frac{\mathrm{d}}{\mathrm{d}t}$ is a Lagrangian derivative. The time scale τ is the "the eddy turn-over time scale" as defined by (31). To simplify things we suppose k, and all parameters describing

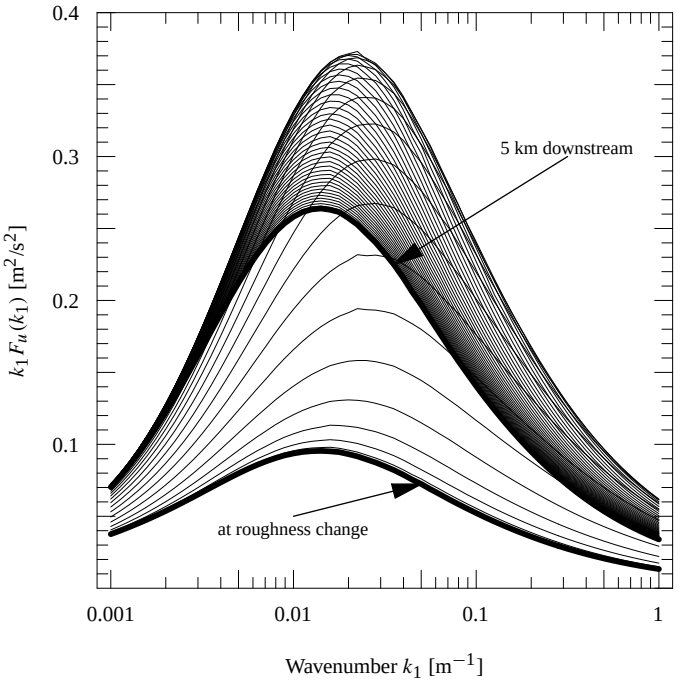

Figure 18. Calculated u-spectra for every 100 m at $z = 20$ m as indicated in figure 17. Notice how turbulence "overshoots" after the roughness change before becoming in equilibrium with the new surface.

the tensor, except the energy dissipation ε, are constants as the turbulence is advected over varying roughness and that the equilibrium energy dissipation is given by

$$\varepsilon_{\text{eq}} = \kappa^2 z^2 \left(\frac{\mathrm{d}U^r}{\mathrm{d}z} \right)^3 , \tag{71}$$

where κ is the von Kármán constant (the superscript r on the mean velocity U refers to the part of the mean velocity perturbation that is due to roughness changes). Then (70) can be written as

$$\frac{\mathrm{d}}{\mathrm{d}t} \varepsilon^{2/3} = \frac{\varepsilon_{\text{eq}}^{2/3} - \varepsilon^{2/3}}{\tau(k)}, \tag{72}$$

where ε is no longer the instantaneous energy dissipation, but merely a spectral multiplier dependent on k.

This equation is derived in the same spirit as done in (Højstrup 1981) but uses the calculated flow field U^r as given by LINCOM and does not require explicit calculations of the positions of internal boundary layers. This formulation should be advantageous when dealing with a terrain with an arbitrarily complex roughness distribution, and not just simple changes along lines in the terrain.

Assuming $t \approx -x/U^0$ (where U^0 is the unperturbed mean wind speed) the solution of (72) is

$$\varepsilon^{2/3} = \frac{1}{U^0 \tau} \int_{-\infty}^{0} \exp\!\left(\frac{x}{U^0 \tau} \right) \kappa^{4/3} z^{4/3} \left(\frac{\partial U^r}{\partial z} \right)^2 \mathrm{d}x. \tag{73}$$

Once LINCOM has calculated $\frac{\partial U^r}{\partial z}$, spectra, cross-spectra and simulated Gaussian wind fields can be calculated from this equation together with a suitable form of the spectral tensor (see sec. 2.2).

To illustrate the model we have calculated u-spectra (figure 17) at various downstream positions of the roughness change. The spectra shown in figure 18 first increases at high wavenumbers and more slowly at lower wavenumbers. Turbulence "overshoots" before settling at an spectrum which is in equilibrium with the higher downstream roughness. While the "overshoot" after a smooth-rough change has been observed in some wind

tunnel turbulence statistics, such as the momentum transport $\langle uw \rangle$ (Antonia and Luxton 1971, Antonia and Luxton 1972), it is only very weak or absent in other like σ_u. It seems obvious that the various components of the Reynolds stress tensor respond differently to the change of roughenss. This certainly requires a more advanced model than ours in which all components change in step. Our model clearly exaggerates the overshoot, however, it is still unclear whether it can be attributed to the linear flow model trough the calculation of $\partial U^r/\partial z$, to the model (73), or both.

2.5.3 Example: The Gedser land mast

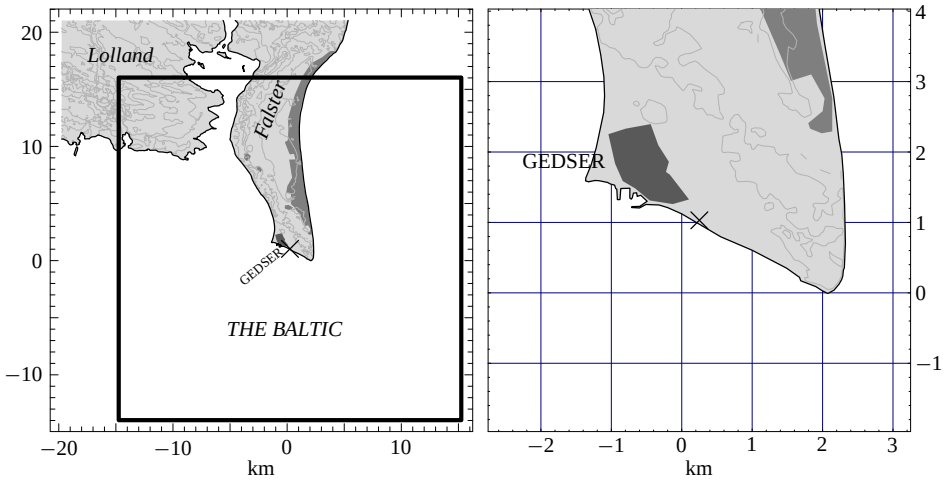

Figure 19. The Gedser land mast (cross). On the left plot the computational domain used in LINCOM is marked. The right plot shows the situation of the town Gedser, which has been assigned a roughness length of $z_0 = 1.0$ m (dark area). Other smaller towns and the forest/summer house area on the east coast have $z_0 = 0.5$ m (gray) while the country side has 0.05 m (light gray).

For offshore wind energy resource estimation one land mast and two offshore masts have been erected in the vicinity of Gedser on the southern tip of Falster, which is an island south of Zealand (Barthelmie, Courtney, Lange, Nielsen, Sempreviva, Svenson and Christensen 1998). The land mast is ideal for testing the roughness model for turbulence, because it is situated in a very flat terrain with drastically varying roughness (see figure 19). The mast is instrumented with cup anemometers at 10, 30 and 45 m, wind vanes, various temperature sensors and a sonic anemometer at 42 m, suitable for turbulence measurements.

We use an almost contiguous record of data from August 1996 to June 1998 in this analysis. All half hour average turbulence intensities measured at 42 m with an average wind speed of more than 12 m/s are plotted in figure 20. Intensities with a positive heat flux (measured with a sonic anemometer) indicating unstable stratification are shown as diamonds, while negative heat flux (stable atmospheric stratification) corresponds to crosses. As it may be seen, there is a systematic difference between the two, showing that atmospheric stability plays a significant role, even at $U > 12$ m/s.

As input for the turbulence calculation we used the LINCOM mean flow generated from the maps shown in figure 19 together with an unperturbed spectral tensor resembling Kaimal's spectra. The predicted turbulence intensities are shown as broad gray curves.

Three things immediately catch the attention:

- The large scatter of measured intensities, which, as shown, is at least partly due to atmospheric stability variations.

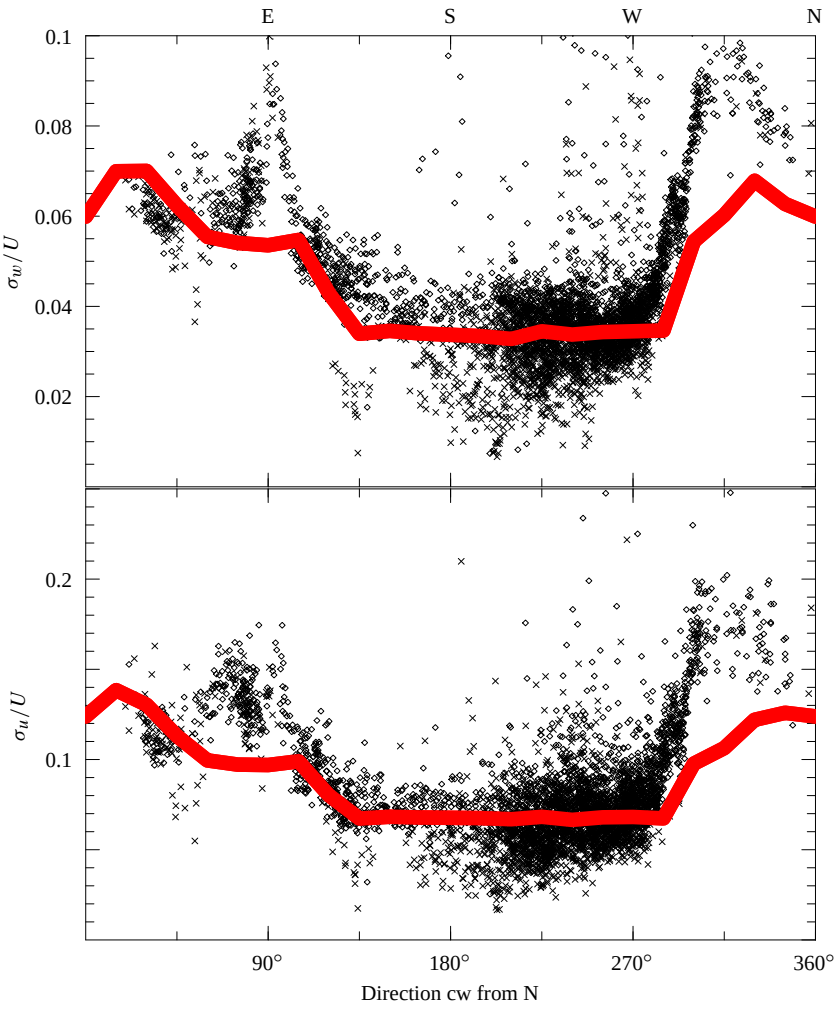

Figure 20. Turbulence intensities (10 minutes averages) from the Gedser land mast. Measurements with unstable atmospheric stratification are diamonds, stable are crosses. The broad gray curve is model results.

- The excess intensity around 90° most noticeable in w. This is due to the instruments being in the wake of the mast, which is not modeled.
- The excess intensity around 315°, which might be due to large obstacles at the harbor of Gedser, a kilometer upstream in that direction.

2.5.4 Example: An island in the Great Belt

In order to better estimate the dynamic loads on the Great Belt Bridge, which opened for traffic in 1998, an experiment was set up on the island of Sprogø in the middle of the Great Belt, see figure 21. Turbulence was measured with several sonic anemometers at high wind speeds at $z = 70$ m from the summer of 1990 until summer 1991, see Mann et al. (1991) for details on the experiment. The terrain surrounding the masts is very simple having a fetch of water for at least 10 km. However, for some directions Sprogø may disturb the flow. As a crude rule of thumb the flow is disturbed up to a height of $0.1x_r$ where x_r the upstream distance to the change of roughness, so turbulence should be enhanced in the "Island" sector and also in the "NW" sector, see the maps in figure 21.

For the calculation of spectra two-hour blocks with a mean speed larger than 15 m/s are chosen. Furthermore, to ensure stationarity only runs wind mean speeds in the previous

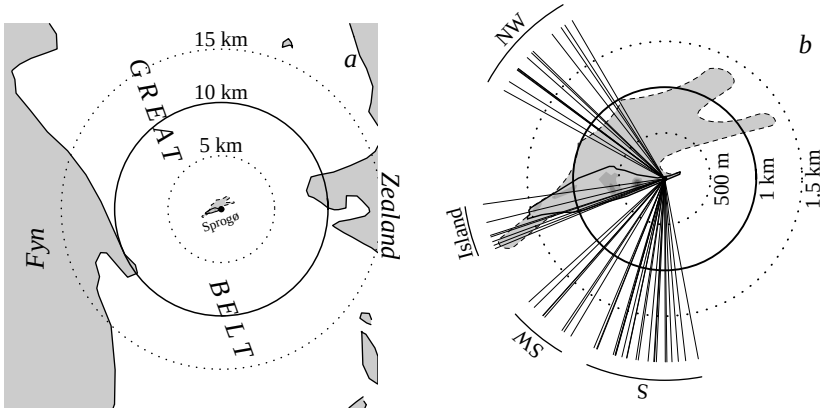

Figure 21. a: *The situation of Sprogø and the mast in The Great Belt.* b: *Close-up of Sprogø with an indication of the directions of all runs analyzed. The broad, black contour is Spogø before the extensions (dashed contours) made in connection with the train and road links. The measurements were made after the extensions were completed and during the construction of the low bridge to the West of Sprogø.*

Table 2. Number of two hour runs from Sprogø and grouping criteria.

Name	$\theta_{\min}$ [°]	$\theta_{\max}$ [°]	Mean wind speed [m/s]	# of runs	# of neutral runs
Island	245	290	16.0	7	5
South	150	210	17.4	22	16
Northwest	298	330	17.0	13	9
Southwest	210	240	15.8	8	5

and following two-hour run within ± 4 m/s and direction within $\pm 45°$ are chosen.

The bulk Richardson number, which is a measure of atmospheric stability, is calculated. It is defined as (Panofsky and Dutton 1984)

$$\mathrm{Rb} = \frac{g z_m^2}{T} \left(\frac{\Delta T / \Delta z + \gamma_d}{U_{8\mathrm{m}}^2} \right) \quad , \tag{74}$$

where g is the acceleration due to gravity, T the mean temperature, γ_d the dry adiabatic lapse rate, ΔT the temperature difference between $z = 2$ m and $z = 10.15$ m, Δz the corresponding height difference, $U_{8\mathrm{m}}^2$ the mean wind speed at 8 m, and z_m a logarithmic average height. In figure 22 spectra with differing atmospheric stabilities are plotted. "Unstable" spectra are defined to have $\mathrm{Rb} < -0.0001$, "stable" $\mathrm{Rb} > 0.0002$, and "neutral" in between. It is seen that especially the stably stratified spectra are different from the neutral spectra in the expected sense that they have less energy. It is also seen that there is a large variability, especially at low wavenumbers. We exclude non-neutral spectra from the average spectra that we are going to compare to the model.

Model calculation are performed on a 20 by 20 km grid centered on Sprogø and the calculated spectra are compared to measurements in figure 23. The modeled spectra show a slight increase in energy for the "Island" sector and an even less increase in the "NW" sector. The measurements show a larger increase in for these sectors and for the "NW" sector the increase is mostly pronounced at low wavenumbers compared to the undisturbed sectors "S" and "SW". These data appears to conflict with (Panofsky et al. 1982, Højstrup 1981) who found that high the wavenumber end of the spectra responds faster to roughness changes. However, we speculate that features in the terrain of Sprogø may trigger recirculation zones which in turn enhance the low wavenumber part

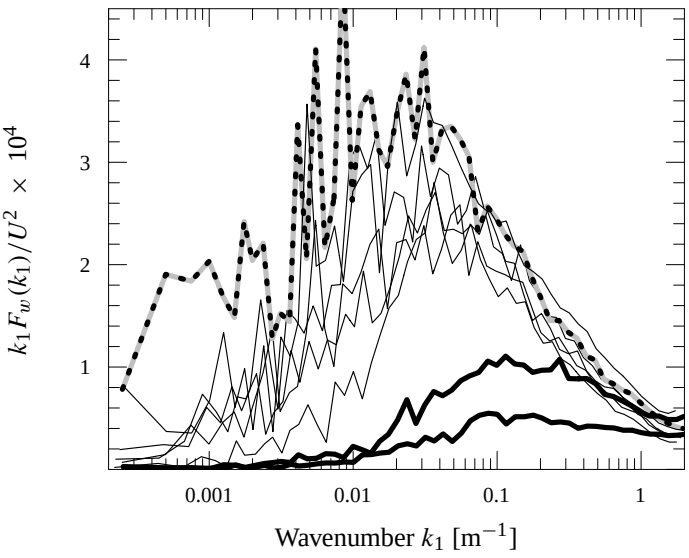

Figure 22. Spectra of the w-component from the Southwest sector. Neutral spectra are thin, solid curves, stable are broader, and unstable are dashed. See figure 7 on page 7 for the South sector data.

of the spectra.

We have also done calculations with a larger grid covering parts of Fyn and Zealand. Spectra only change slightly when this larger calculations domain is used.

2.6 Orography

Rapid distortion theory was originally developed to model turbulence in wind tunnel contractions (Batchelor and Proudman 1954, Townsend 1976), but has later been applied to a variety of atmospheric turbulent flows such as neutral flow over flat terrain (Mann 1994) or hills (Britter, Hunt and Richards 1981), the convective boundary layer close to the ground (Hunt 1984) or the inversion (Carruthers and Hunt 1986) and flow over waves (Townsend 1972). In many applications both the "rapid" condition and the condition of homogeneity have been treated rather loosely but often with good results (Savill 1987).

The rapid distortion equations describe the response of turbulence to a uniform gradient of the mean velocity $\partial U_i/\partial x_j$ over times which are small compared to the time scales of the eddies. In complex terrain the mean velocity gradients are far from constant and small eddies typically have short life times compared to the advection time over features in the terrain. Rapid distortion theory (RDT) should thus be applicable for eddies smaller than the scale of variations in the mean flow gradients but larger than the eddies with a too small life time.

In (Britter et al. 1981) the relative change in the integrated turbulence statistics (such as σ_u^2) above the top a two-dimensional hill is modeled by rapid distortion of isotropic turbulence. The authors ignore shear ($\partial U/\partial z$) entirely but get results in qualitative agreement with wind tunnel measurements for both the *relative change* of σ_u and σ_w.

Since we are not only interested in relative changes but rather the absolute value of the spectral energy in different bands our approach is somewhat different. We want to estimate the combined effect of shear and strain along the principal axes. While explicit solutions to the rapid distortion equations exists for both of these distortions separately, there is unfortunately no such for the combined case (Townsend 1980). As stated in the beginning we would like a fast computer code and would like as far as possible to avoid numerical integration of differential equations, so the way we approximate the combined action of shear and strain is to use the spectral model of section 2.2 as the upstream model,

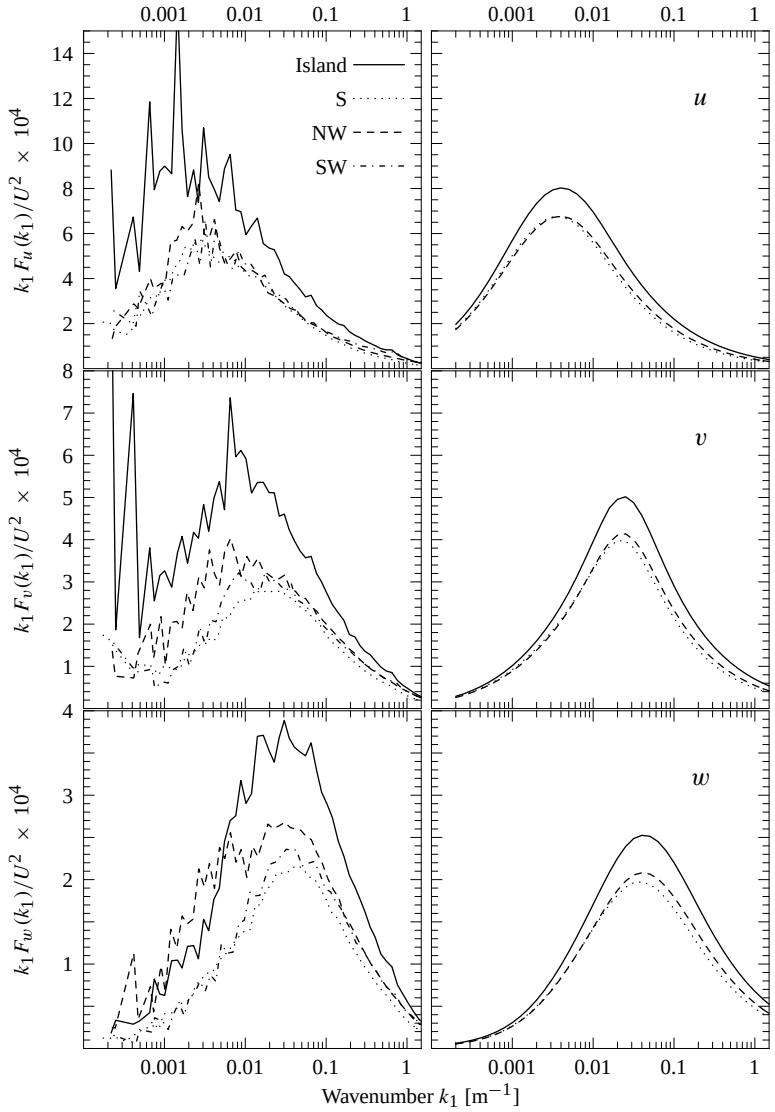

Figure 23. Comparison of measured (left column) and modeled spectra (right) from Sprogø.

which already has the effects of shear included, and then apply the irrotational distortions calculated from the linear mean flow model. We ignore the variations in the off diagonal elements in the tensor $\partial U_i/\partial x_j$. This implies for example that effect of transversal shear and curvature of the stream-lines will be neglected.

Britter et al. (1981) applies rapid distortion to all wavenumbers in the spectrum. Here the ambition is to model each part of the spectrum, not only the integrated second order statistics. Therefore, we must take special care of the areas of the spectrum where the assumptions of RDT are broken. At high frequencies (or wavenumbers) the lifetime of eddies is very short and the eddies are *not* affected by the entire upstream history of distortions. At low wavenumbers the distortion will typically not be homogeneous over the entire extent of the eddy, which is one of the basic assumptions in RDT (see figure 26). There has been attempts to generalize RDT to inhomogeneous mean flows, but they did not result in closed-form solutions and would require excessive computing time (Hunt 1973).

We have implemented some simplified solutions to take into account these deficiencies of RDT. However, the calculated spectra do not compare better to the few measurements in complex orography we have analyzed, so, until more experimental evidence is present, we assume no lower wavenumber limit of the validity of RDT.

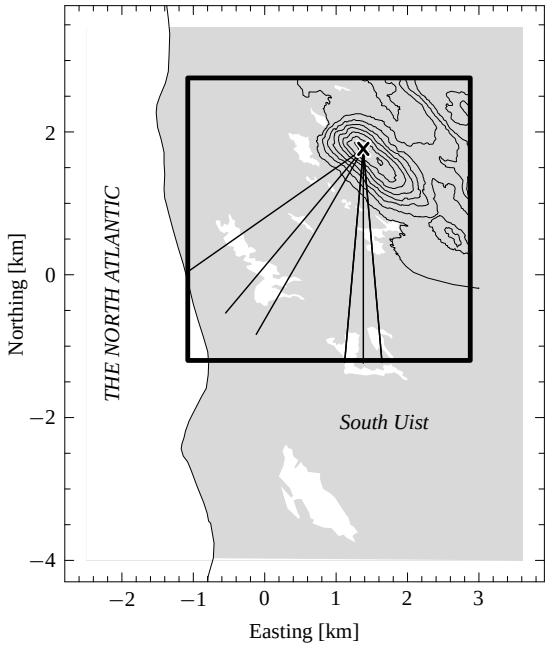

Figure 24. The Askervein hill. The position of the 46 m mast is indicated by a cross and the straight lines indicate the estimated mean directions for the analysed runs. The box is the computational domain used by LINCOM. Gray corresponds to $z_0 = 0.03$ *m and white to* 5×10^{-4} *m.*

Usually, the effect of irrotational distortion along the coordinate axes is estimated by RDT through the *total strain ratios* e_i (Townsend 1976)

$$\ln(e_i) = \int_{-\infty}^{0} \frac{\alpha_i(x)}{U(\boldsymbol{x})} \mathrm{d}x, \tag{75}$$

where the integration is done over the entire upstream track (negative x) and where $\alpha_i \equiv \partial U_i / \partial x_i$ (no summation).

We modify this to take into account finite lifetime:

$$\ln(e_i) = \int_{-\infty}^{0} \exp\left(\frac{x}{U(\boldsymbol{x})\tau(k)} \right) \frac{\alpha_i(x)}{U(x)} \mathrm{d}x, \tag{76}$$

where $\tau(k)$ is the eddy time scale (31), i.e. small, short-lived eddies hardly experience any distortion at all. This guarantees the $\frac{4}{3}$-ratio between transversal (v and w) and longitudinal spectra (u) at high frequencies. These modified strain ratios are subsequently used in the RDT calculations.

2.6.1 Example: The Askervein Hill

The Askervein Hill Field Experiment took place in September/October 1982 and September/October 1983. The purpose was to study boundary-layer flow over a low hill (Taylor and Teunissen 1983, Taylor and Teunissen 1985, Walmsley and Taylor 1996).

Askervein is a 116 m high hill (126 m above sea level) on the west coast of South Uist of the Outer Hebrides, Scotland. As seen from figure 24 it has an essentially elliptical base.

Spectra from the sonic anemometer at $z = 47$ m on the mast at the hill top are calculated and runs with mean wind directions around 180° and 225° are shown in figure 25. Most runs are longer than one hour and they have all wind speeds larger than 13 m/s. Superimposed in the same figure are calculated model spectra for the two directions. The hill top spectra have considerably different distribution of turbulent energy among the

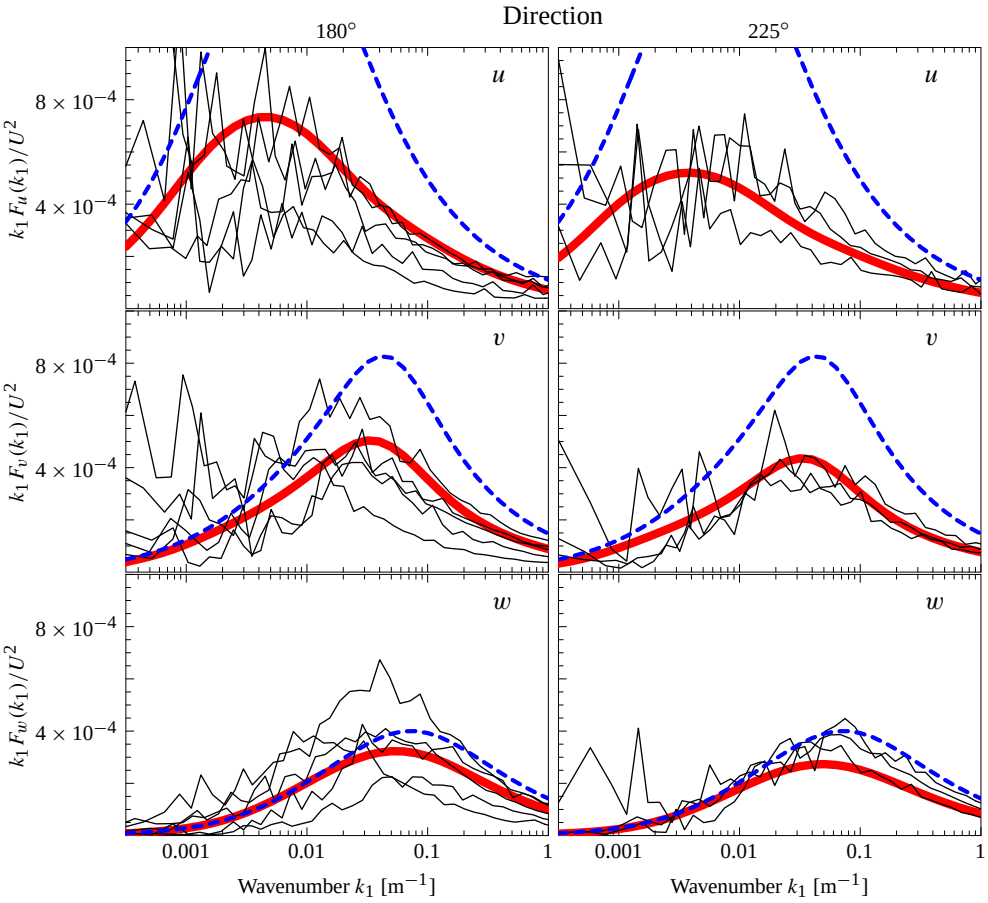

Figure 25. Measured and modeled spectra at $z = 47$ m at the top of the Askervein Hill. The broad, gray curves are the model calculations and the thin, black curves are measurements. The dashed curves are flat terrain spectra. All spectra have been normalized with the squared mean speed at the hill top, except for the dashed which are normalized with the square of the flat terrain wind speed.

Table 3. Comparison of model calculations of Askervein hill top variances to flat terrain values at $z = 47$ m. From both directions σ_u^2 decreases, σ_w^2 increases, while σ_v^2 is almost unchanged. The suppression of all hill top spectra compared to flat terrain spectra in figure 25 are mainly due to the normalization with U^2, which makes the turbulence intensity (the square root of the area under these curves) much lower at the hill top compared to flat terrain.

		$\sigma^2_{\mathrm{HT}}/\sigma^2$		
Direction	U_{HT}/U	u	v	w
180°	1.26	0.87	1.03	1.33
225°	1.37	0.75	1.03	1.34

three component spectra compared to what is found over flat terrain. The u-spectrum is considerably attenuated while the w-spectrum is enhanced. The modeled spectra agrees reasonably well with the measured, however, the experimental spectra have considerable scatter, probably caused by variation in the atmospheric stability.

2.6.2 Is RDT valid at low frequencies?

Although the rejection of RDT at low wavenumbers is not obvious from the Askervein data, there are several reasons to question RDT anyway.

Many studies indicate that in a boundary layer gusts with larger wavelengths are advected faster than indicated by Taylor's hypothesis (Mizuno and Panofsky 1975, Kim and Hussain 1993). This is because large eddies are somehow attached to flow further away from the surface where the mean wind speed is larger. The terrain induced strains decrease rapidly with height, so one may expect the effects of RDT to be attenuated for large eddies, i.e. low frequencies. One way of doing this would be to use

$$\ln(e_i) = \int_{-\infty}^{0} \exp\left(\frac{x}{U(x,y,z')\tau(k)}\right) \frac{\alpha_i(x,y,z')}{U(x,y,z')} \mathrm{d}x \tag{77}$$

instead of (76), where

$$z'^2 = z^2 + \frac{1}{k_3^2} \quad \text{or} \quad z'^2 = z^2 + \frac{1}{k^2} \tag{78}$$

where we have used the later expression for computational convenience. In other words we use the strains calculated at z' which is wavenumber dependent and larger than z.

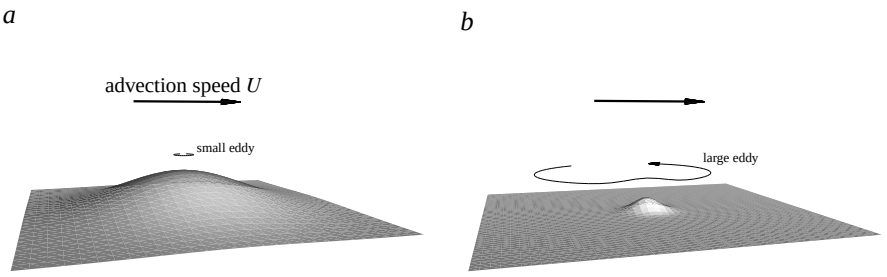

Figure 26. The difference between RDT and quasi-stationary amplification illustrated by flow over a simple hill. In a the eddy experiences roughly the same distortion over its extent implying (if the distortion is also rapid) that RDT applies. In b the eddy is larger than the hill and the wind variations are amplified as if they were changes in the mean speed U^0.

Preliminary calculations with (77) indicate that this does *not* improve the model performance.

Another effect which should counteract RDT in some situations is quasi-steady amplification of the low frequency fluctuations as illustrated in figure 26. Again, comparison with the Askervein data shows that the inclusion of this effect does not improve the model, somewhat in contrast to the findings of Frank (1996).

2.7 Turbulent wind field simulation

Having discussed the spectral tensor in flat terrain (section 2.2), in relation to literature spectra (section 2.3), and in complex terrain (section 2.4), we now describe how to simulate a velocity field $\boldsymbol{u}(\boldsymbol{x})$.

We approximate the integral (3) by a discrete Fourier series:

$$u_i(\boldsymbol{x}) = \sum_{\boldsymbol{k}} \mathrm{e}^{\mathrm{i}\boldsymbol{k}\cdot\boldsymbol{x}} C_{ij}(\boldsymbol{k}) n_j(\boldsymbol{k}), \tag{79}$$

where the l'th component of $\boldsymbol{x}$ is $x_l = n\Delta L_l$ with $n = 1, ..., N_l$. The symbol $\sum_{\boldsymbol{k}}$ denotes the sum over all wave vectors $\boldsymbol{k}$ with components $k_i = m2\pi/L_i$, with the integer $m = -N_i/2, ..., N_i/2$, $n_j(\boldsymbol{k})$ are independent Gaussian stochastic complex variables with unit variance and $C_{ij}(\boldsymbol{k})$ are coefficients to be determined. See figure 27. The great advantage

of (79) is that, once the coefficients are known, it can be evaluated very fast by the fast Fourier transform (FFT) (Shinozuka and Deodatis 1991).

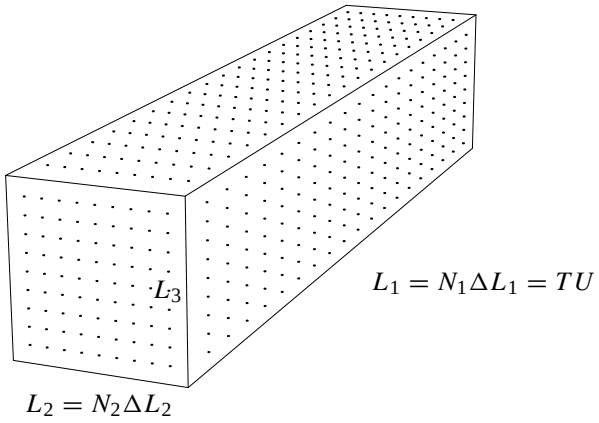

Figure 27. The box B consists of $N_1 \times N_2 \times N_3$ points and has side lengths L_i, $i = 1, 2, 3$, so the separation between the points in the i-direction is $\Delta L_i = L_i/N_i$. U is the mean wind speed and T is the simulation time.

Solving (79) we get (approximately, see the appendix of Mann (1998)).

$$C_{ij}(\boldsymbol{k}) n_j(\boldsymbol{k}) = \frac{1}{V(B)} \int_B u_i(\boldsymbol{x}) \mathrm{e}^{-\mathrm{i}\boldsymbol{k}\cdot\boldsymbol{x}} \mathrm{d}\boldsymbol{x}, \tag{80}$$

where $V(B) = L_1 L_2 L_3$ is the volume of B and $\int_B \mathrm{d}\boldsymbol{x}$ means integration over the box B. From (80) it is easy to see that $n_j(\boldsymbol{k})$ *have* to be Gaussian when $u_i(\boldsymbol{x})$ is a Gaussian field. Many authors relax this constraint and let $n_j(\boldsymbol{k})$ have random phase but a fixed absolute value (Shinozuka and Jan 1972, Shinozuka and Deodatis 1991, Shinozuka and Deodatis 1996). Using this approach every sample will get exactly the same variance and, given a wavenumber (or vector), the estimated power spectral density at this wavenumber will be the same for all realizations of the same process. This might be advantageous in some situations, but it is in contrast to power spectral density estimates of stationary time series which have 100% rms (Press, Flannery, Teukolsky and Vetterling 1992, Bendat and Piersol 1971). The difference between the two approaches is discussed in detail in (Grigoriu 1993). In practice there is little difference and both models could be used. However, the Gaussian approach is usually easier to analyse theoretically and we shall stick to that here.

To find the coefficients $C_{ij}(\boldsymbol{k})$ we calculate the covariance tensor of (80) obtaining

$$\begin{aligned} & C^*_{ik}(\boldsymbol{k}) C_{jk}(\boldsymbol{k}) \\ &= \frac{1}{V^2(B)} \int_B \int_B \left\langle u_i(\boldsymbol{x}) u_j(\boldsymbol{x}') \right\rangle \mathrm{e}^{\mathrm{i}\boldsymbol{k}\cdot\boldsymbol{x}} \mathrm{e}^{-\mathrm{i}\boldsymbol{k}\cdot\boldsymbol{x}'} \mathrm{d}\boldsymbol{x}\mathrm{d}\boldsymbol{x}' \\ &= \frac{1}{V^2(B)} \int \int R_{ij}(\boldsymbol{x} - \boldsymbol{x}') 1_B(\boldsymbol{x}) 1_B(\boldsymbol{x}') \mathrm{e}^{\mathrm{i}\boldsymbol{k}\cdot(\boldsymbol{x}-\boldsymbol{x}')} \mathrm{d}\boldsymbol{x}\mathrm{d}\boldsymbol{x}', \end{aligned} \tag{81}$$

where $1_B(\boldsymbol{x}) = 1$ if $\boldsymbol{x} \in B$ and 0 otherwise. Using the change of variables $\boldsymbol{r} = \boldsymbol{x} - \boldsymbol{x}'$ and $\boldsymbol{s} = \boldsymbol{x} + \boldsymbol{x}'$ having the Jacobian $|\partial(\boldsymbol{r}, \boldsymbol{s})/\partial(\boldsymbol{x}, \boldsymbol{x}')| = 8$ we get

$$C_{ik}(\boldsymbol{k}) C_{kj}(\boldsymbol{k}) = \frac{1}{8V^2(B)} \int R_{ij}(\boldsymbol{r}) \mathrm{e}^{-i\boldsymbol{k}\cdot\boldsymbol{r}} \int 1_B\left(\frac{\boldsymbol{s}+\boldsymbol{r}}{2}\right) 1_B\left(\frac{\boldsymbol{s}-\boldsymbol{r}}{2}\right) \mathrm{d}\boldsymbol{s}\mathrm{d}\boldsymbol{r} \tag{82}$$

The inner integration can be carried out according to

$$\int 1_B\left(\frac{\boldsymbol{s}+\boldsymbol{r}}{2}\right)1_B\left(\frac{\boldsymbol{s}-\boldsymbol{r}}{2}\right)\mathrm{d}\boldsymbol{s} = \begin{cases} \prod_{l=1}^{3} 2(L_l - |r_l|) & \text{for } |r_l| < L_l \text{ for all } l \\ 0 & \text{otherwise} \end{cases} \tag{83}$$

so, using the convolution theorem and noting that the Fourier transform of $L - |r|$ (for

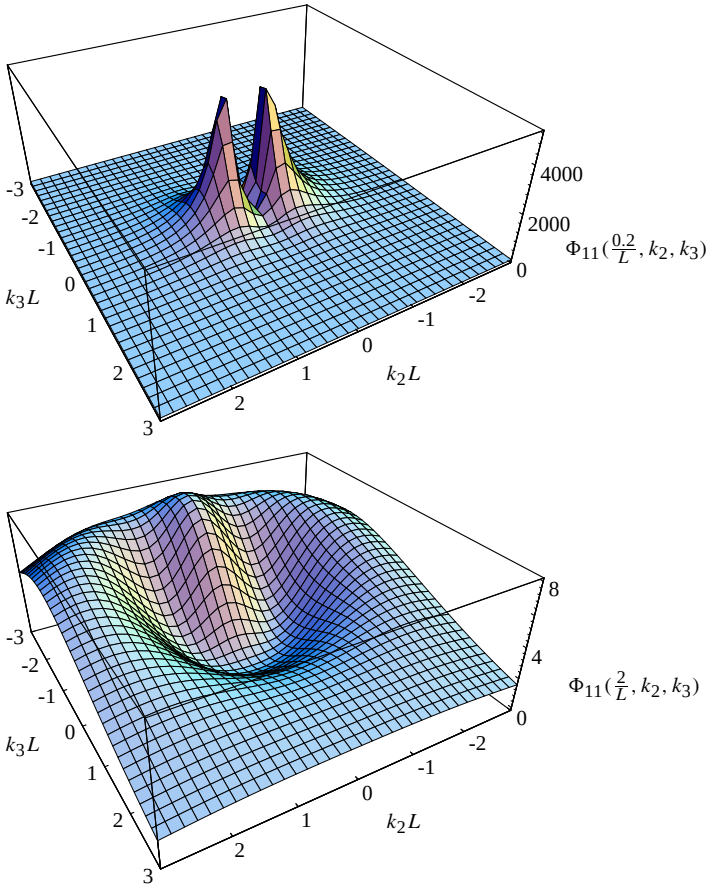

Figure 28. $\Phi_{11}(\boldsymbol{k})$ *(in arbitrary units) at* $k_1 = 0.2/L$ *and* $2/L$ *with* $\Gamma = 3$.

$|r| < L$ and else 0) is $L^2\,\mathrm{sinc}^2(kL/2)$, we get

$$C^*_{ik}(\boldsymbol{k})C_{jk}(\boldsymbol{k}) = \int \Phi_{ij}(\boldsymbol{k}')\prod_{l=1}^{3}\mathrm{sinc}^2\left(\frac{(k_l - k'_l)L_l}{2}\right)\mathrm{d}\boldsymbol{k}', \tag{84}$$

where $\mathrm{sinc}\,x \equiv (\sin x)/x$. For $L_l \gg L$, the sinc^2-function is 'delta-function-like', in the sense that it vanishes away from k_l much faster than any change in Φ_{ij}, and the area beneath the sinc^2-curve is $2\pi/L_l$. Therefore, we get

$$C^*_{ik}(\boldsymbol{k})C_{jk}(\boldsymbol{k}) = \frac{(2\pi)^3}{V(B)}\Phi_{ij}(\boldsymbol{k}). \tag{85}$$

The solution to (85) is

$$C_{ij}(\boldsymbol{k}) = \frac{(2\pi)^{3/2}}{V(B)^{1/2}}A_{ij}(\boldsymbol{k}) = (\Delta k_1\Delta k_2\Delta k_3)^{1/2}\,A_{ij}(\boldsymbol{k}) \tag{86}$$

with $A^*_{ik}A_{jk} = \Phi_{ij}$ and $\Delta k_l = 2\pi/L_l$. This result should be expected when comparing (3) to (79).

An example of a simulated non-isotropic velocity field with $\Gamma = 3$ is shown in Figure 29. It is seen on the upper plot that the shear tilts the elongated fluctuations. Similar plots of the w-components show much less elongation and a shorter length scale.

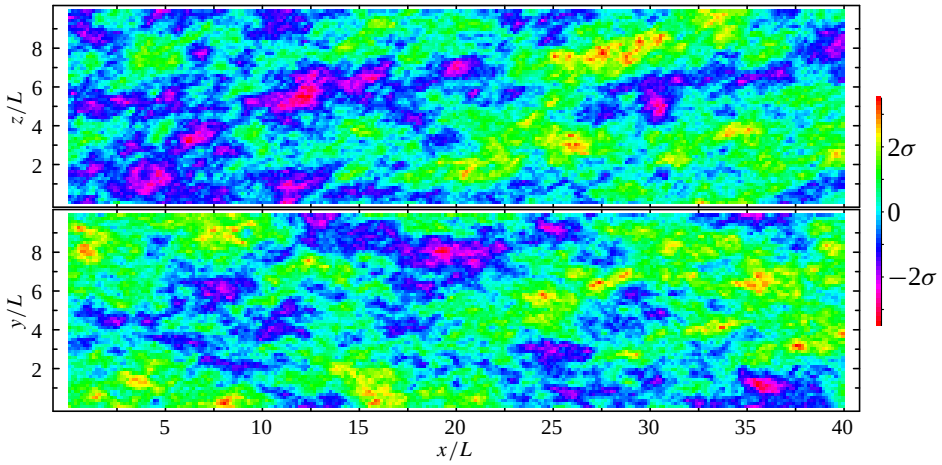

Figure 29. Vertical and horizontal cross sections of the u-fluctuations of simulated non-isotropic turbulence with $\Gamma = 3$.

2.7.1 Problems with discretization and periodicity

Two problems occur by simulating a field by the Fourier series (79) with the coefficients (86). The first is that for many applications the dimensions of the simulated box of turbulence need *not* to be much larger than the length scale of the turbulence model L. Therefore (85) may not be a good approximation to (84). However, almost always for practical applications $L_1 \gg L$, so we can at least reduce (84) to

$$C_{ik}^*(\boldsymbol{k})C_{jk}(\boldsymbol{k}) = \frac{2\pi}{L_1}\int \Phi_{ij}(k_1,k_2',k_3')\prod_{l=2}^{3}\mathrm{sinc}^2\left(\frac{(k_l-k_l')L_l}{2}\right)\mathrm{d}\boldsymbol{k}_\perp', \tag{87}$$

where $\int \mathrm{d}\boldsymbol{k}_\perp \equiv \int_{-\infty}^{\infty}\int_{-\infty}^{\infty}\mathrm{d}k_2\mathrm{d}k_3$. This integration, which has to be done numerically[2] is here limited to wave vectors, $\boldsymbol{k}$, obeying $k = |\boldsymbol{k}| < 3/L$. Outside this volume we consider (85) a good approximation to (84), regardless of the dimensions of the box. This discretization problem is illustrated by figure 28 and 30. Figure 28 shows that close to $\boldsymbol{k} = 0$, $\Phi_{ij}(\boldsymbol{k})$ varies rapidly implying that (85) may be a poor approximation to (84). Figure 30 indicate that (87) must be used if L_l ($l = 2$ or 3) is less than $\propto 8L$.

The second problem is that the simulated velocity field (79) is periodic in all three directions. Originally, Shinozuka and Jan (1972) suggested to perturb the wave vectors in (79) to avoid this problem. However, this would corrupt the efficiency of the FFT. Our solution to the problem is to use a larger spatial window. In figure 31 the coherence of vertical velocity fluctuations for a vertical separation

$$\mathrm{coh}_{ww}(k_1,z) \equiv \frac{|\chi_{33}(k_1,z)|^2}{\chi_{33}(k_1,0)^2}, \tag{88}$$

calculated from the sheared velocity tensor with $\Gamma = 4$, is shown together with coherences calculated from simulations with $2048 \times 32 \times 32$ points and dimensions $256L \times 3L \times 3L$. Since the simulated field is periodic the coherence goes to 1 as $z \to L_3 = 3L$. In a structural response analysis the space domain (L_2 and L_3) should be chosen large enough to contain roughly *twice* the structure of interest in each dimension. However, if

[2] In practice the integration is only done over $|k_l' - k_l| < 2\pi/L_l \;\; l = 2,3$ i.e. out to the first zero in the sinc-function. The loss in variance is accounted for by multiplying by c^2 with $c = \int_{-\infty}^{\infty}\mathrm{sinc}^2(x)\mathrm{d}x \Big/ \int_{-\pi}^{\pi}\mathrm{sinc}^2(x)\mathrm{d}x = \frac{\pi}{2\mathrm{Si}(2\pi)} = 1.1076$, where Si is the sine integral function. An even better representation of the target spectrum is possible if the integration interval of the convolution is extended. However, out to the first zeros seems to be sufficient.

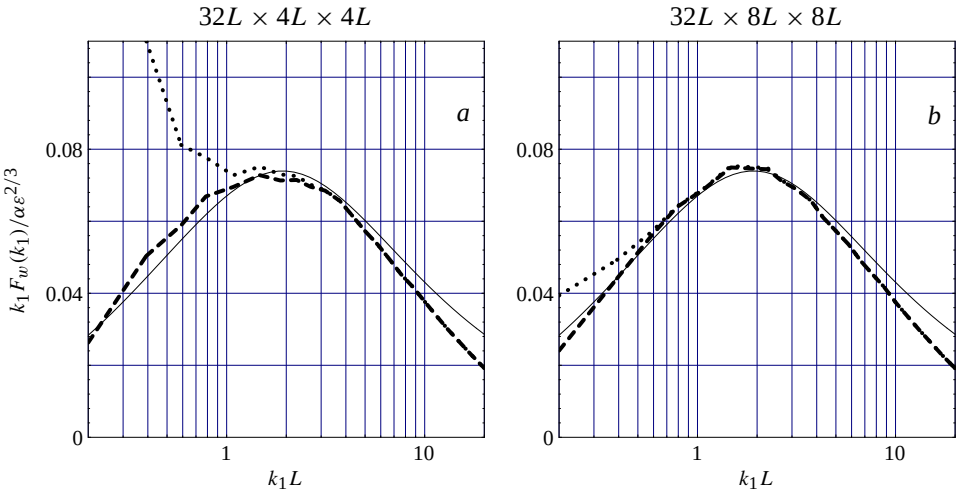

Figure 30. The discretization problem illustrated by a w-spectrum with $\Gamma = 3.0$. The thin line is the target spectrum, the dotted line is the average spectrum obtained by using (86) and the dashed line is an average spectrum using (87). a) *Average spectra of 100 simulations with box dimensions* $32L \times 4L \times 4L$ *(*$512 \times 32 \times 32$ *points).* b) *Average spectra of 20 simulations with* $32L \times 8L \times 8L$ *(*$512 \times 64 \times 64$ *points).*

$L_l \gg L$ or if the structure is insensitive to low frequency fluctuations the structure might cover more than half the simulated field in each direction.

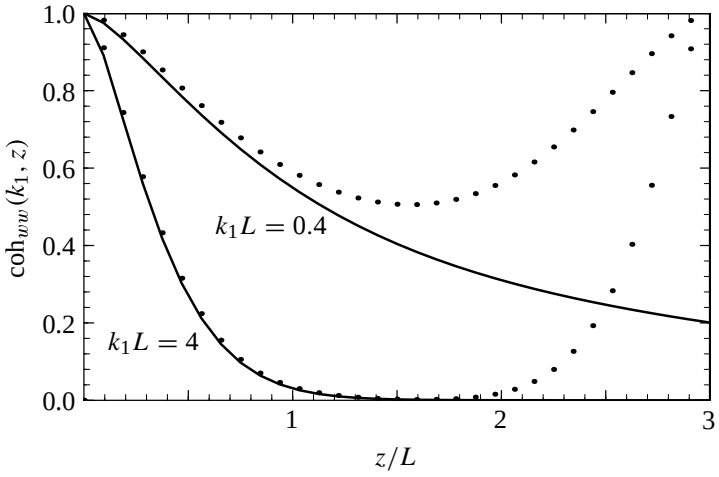

Figure 31. Illustration of periodicity. Simulated (dots) and model w-coherences (curves) as functions of vertical coordinate z. The vertical dimension of the box is $L_3 = 3L$.

A final point is that the simulated spectra are typically attenuated at high wave numbers (or frequencies) as seen from figure 30. The reason is that the wind speed is spatially averaged over a small volume roughly of the size $\Delta L_1 \times \Delta L_2 \times \Delta L_3$. In most engineering applications it is exactly this averaged field which is needed, but if the un-averaged 'point velocities' are required they can still be simulated with our technique. Details of this aliasing problem are scrutinized in Mann (1998).

2.7.2 Implementation and speed

The implementation of the model includes three steps:

1. Evaluate the coefficients $C_{ij}(\boldsymbol{k})$, either by (86) or, if necessary, by (87) using the factorizations discussed in the previous section.
2. Simulate the Gaussian variable $n_j(\boldsymbol{k})$ and multiply.
3. Calculate $u_i(\boldsymbol{x})$ from (79) by FFT.

The time consumption in the first step is proportional to the total number of points $N = N_1 N_2 N_3$ in the simulation. The required time to perform the FFT is $O(N \log_2 N)$ (Press et al. 1992).

In practice, simulating a three-dimensional field, used for load calculations on wind turbines, with millions of velocity vectors takes of the order of a few minutes on a modern pc.

3 Revision of the LINCOM model

3.1 Motivation

LINCOM has a big problem. The calculated streamlines are vertical at the boundary, where they should run parallel with it. The intentions with the model is that, sufficiently close to the surface, the flow should resemble and ordinary log-profile as over flat terrain. The 'inner' solution should take care of this, but apparently this is not what happens in the model. Below a simple way out of the the problem is proposed which constitutes only a minor revision. In addition the interpretation of geometry is made straight forward.

In Section 3.2 the necessary steps are taken to formulate a concise perturbation problem. The results are used in Section 3.3 to revise the LINCOM model equations. Sections 3.4, 3.5 and 3.6 are devoted to a discussion of the equations that come out of the perturbation problem, omitting the approximations made in LINCOM. The approach is applied to flow over a sinusoidal row of hills, assuming that the unperturbed profile is of the form $V(z) = \alpha z$. Model results are compared to data from wind tunnel experiments.

3.2 The first order strategy

We consider incompressible turbulent flow over terrain defined by a orography function $h(x, y)$. In flat terrain ($h = 0$) we have of course the well known logarithmic profile and we expect this to be only slightly modified if h is suitably small. It is therefore natural to attempt a perturbation approach. In order to avoid certain mathematical inconsistencies (to be discussed below) we propose the following strategy:

1. A coordinate transformation is applied which simplifies the domain to $z > 0$.
2. A divergence free velocity $\boldsymbol{v}''$ is defined in the transformed system.
3. The governing equation for $\boldsymbol{v}''$ is written down in transformed coordinates.
4. Extra non-Navier-Stokes terms are identified.
5. The transformation which (in some suitable sense) minimizes or simplifies the extra terms may be chosen.
6. The momentum equation is ensemble averaged.
7. An appropriate closure is postulated.
8. An expansion parameter ϵ is introduced in the extra terms. The extra terms should be unchanged for $\epsilon = 1$ and vanish for $\epsilon = 0$.
9. The equation is simplified by keeping only first order terms in the ϵ.
10. ϵ is set equal to 1.
11. The closed equation is solved based on knowledge of the zero-th order solution.
12. The solution is transformed back to original coordinates.

A 'first order' perturbation with respect to a certain quantity has a concise meaning. The concept can be applied in situations where we have a set of differential equations containing a perturbation term, say Q. Q may enter the equations and/or the boundary condition. The procedure is to substitute Q with $\epsilon\, Q$ and expand solutions in powers of the expansion parameter ϵ. In our case we may want h to play the role of Q, but there is a complication due the fact that h defines the boundary as such and therefore enters the problem in a more fundamental way than just through terms in governing equations and boundary conditions. The problem is how to compare solutions for different boundaries. A point close to the ground in the unperturbed case may become located below the surface

when the perturbation is turned on and the perturbed velocity is not defined. Therefore it makes no sense to compare solutions for different boundaries unless we specify a one-to-one connection between points in the two domains. The coordinate transformation takes care of this, because the boundary is flat in transformed system and does not change with h. The simple, flat boundary has other convenient features. For example, it allows us we to define the Fourier transform in the x and y coordinates, e.g.

$$\boldsymbol{v}(k_1, k_2, z) \equiv \frac{1}{2\pi} \int\int \boldsymbol{v}(x, y, z)\, \mathrm{e}^{-ik_1 x - ik_2 y}\, \mathrm{d}x\mathrm{d}y \tag{89}$$

This is not possible with a curved boundary because $\boldsymbol{v}$ is not defined *inside* the hills.

It is customary to use the following transformation

$$\begin{aligned} x_1'' &= x_1 \\ x_2'' &= x_2 \\ x_3'' &= x_3 - h(x_1, x_2) \end{aligned} \tag{90}$$

Simplicity is the main virtue of this transformation, but there are of course many other transformation that flatten the boundary, even among transformations that depend linearly on h. In generally we may write the transformation as

$$x_i'' = x_i - \lambda_i(x, y, z) \tag{91}$$

with the condition

$$\lambda_3(x, y, h(x, y)) = h(x, y) \tag{92}$$

so that $x_3'' = 0$ at the surface. The the extra terms in reformulated equations will depend on h through λ_i. Therefore it is convenient to use λ_i as the seed of the perturbation. In other words, we replace λ_i with $\epsilon\lambda_i$, expand in powers of ϵ, discard terms of order ϵ^2 or higher, set $\epsilon = 1$ and solve the equations.

The next step is to define a transformed velocity field v_i''. We cannot just let $\boldsymbol{v}''(\boldsymbol{x}'') = \boldsymbol{v}(\boldsymbol{x})$ because this may violate mass conservation (this is one of the problems with LINCOM). The new field should be divergence free, i.e.

$$\frac{\partial v_i''}{\partial x_i''} = 0 \tag{93}$$

where the partial derivatives are with respect to transformed coordinates. The following transformation produces a divergence free field whenever $\nabla \cdot \boldsymbol{v} = 0$

$$v_i'' \equiv D\, \frac{\partial x_i''}{\partial x_j}\, v_j \tag{94}$$

where D is the Jacobian of the transformation (i.e. the determinant of the matrix $\frac{\partial x_i}{\partial x_j''}$). In the appendix we show this by proving that

$$\frac{\partial v_i''}{\partial x_i''} = D \frac{\partial v_j}{\partial x_j} \tag{95}$$

The term $\frac{\partial x_i''}{\partial x_j}\, v_j$ represents the velocity of the image of the fluid element located at $\boldsymbol{x}$ in the original system. This may seem to be a natural definition of a transformed velocity, because it maps streamlines onto streamlines, but care should be taken not to sacrifice the mass balance. It is not necessary to identify fluid elements in the two systems, an we may in fact define the new velocity entirely as we wish, as long as we can transform back and forth. It therefore seems even more natural to define a divergence free vector field so

that mass is conserved for perturbations of any order. The inclusion of the factor D in the definition of the transformed velocity insures this.

The inverse transformation is

$$v_i \equiv \frac{1}{D}\,\frac{\partial x_i}{\partial x_j''}\,v_j'' \tag{96}$$

Inserting this into the N-S equations we obtain the new, transformed N-S equation. After some manipulations it can be written as

$$\frac{\partial v_i''}{\partial t} + \frac{1}{D}\,v_q''\frac{\partial v_i''}{\partial x_q''} + v_p''\,v_q''\,\frac{\partial x_i''}{\partial x_j}\,\frac{\partial}{\partial x_p''}\left[\frac{1}{D}\,\frac{\partial x_j}{\partial x_q''}\right] = -D\,\frac{\partial x_i''}{\partial x_j}\,\frac{\partial x_q''}{\partial x_j}\,\frac{\partial P}{\partial x_q''} + \text{ viscous term} \tag{97}$$

This equation is exact since no approximations have been made so far. The viscous term is quite complicated, but it plays a minor role and will soon be discarded, so we have not written it explicitly. Compared to the normal Navier-Stokes equation several new terms appear. The factor D is responsible for some of them and it clearly would be convenient if $D = 1$. This is a strong argument for choosing (90). It would also simplify matters if $\frac{\partial x_i''}{\partial x_j}\,\frac{\partial x_q''}{\partial x_j}$ was proportional to δ_{iq} so that we have an ordinary pressure gradient on the right hand side of the equation. This requires that the planes $x_i''(\boldsymbol{x}) =$ constant makes right angle intersections with planes $x_q''(\boldsymbol{x}) =$ constant for $i \neq q$. It should be realized that not all simplifications we may want can be imposed at the same time, and of course we cannot get rid of all the extra terms.

According to the strategy we only retain terms to first order in the expansion parameter ϵ. We may expand λ_i in terms of h also, but the way λ_i depends on h is a separate problem altogether, and we can treat λ_i exactly or to first order in h as we wish. When $\lambda_i = A_i h$, where A_i are linear operators, as in (90), it does not matter if we place the ϵ on h or λ_i.

Jackson and Hunt (1975) introduced the concepts of 'inner' and 'outer' solutions. The idea is that the flow looks like an ordinary surface layer flow close to the surface, but higher above the terrain the the mean flow is essentially determined by the pressure perturbations and resembles a potential flow. We may recover the essence of these results by choosing the coordinate transformation (the link between h and λ_i) in such a way that the transformed coordinates follow the outer solution streamlines, while the perturbations of the transformed NS equation takes care of the modifications close to the ground (the inner solution). We leave this to future speculations.

To first order in λ_i we have

$$\frac{\partial x_i}{\partial x_j''} \approx \delta_{ij} + \frac{\partial \lambda_i}{\partial x_j''} \approx \delta_{ij} + \frac{\partial \lambda_i}{\partial x_j} \tag{98}$$

and

$$D \approx 1 + \frac{\partial \lambda_i}{\partial x_i''} \tag{99}$$

and

$$\frac{\partial x_i''}{\partial x_j}\,\frac{\partial x_q''}{\partial x_j} \approx \delta_{iq} - \frac{\partial \lambda_i}{\partial x_q} - \frac{\partial \lambda_q}{\partial x_i} \tag{100}$$

Inserting into (97) yields the linearized equation

$$\begin{aligned} &\frac{\partial v_i''}{\partial t} + v_q''\frac{\partial v_i''}{\partial x_q''} - v_q''\frac{\partial}{\partial x_q''}\left(v_i''\frac{\partial \lambda_j}{\partial x_j''}\right) + v_p''\,v_q''\frac{\partial^2 \lambda_i}{\partial x_p'' \partial x_q''} \\ = \;& -\left[\delta_{iq} - \frac{\partial \lambda_j}{\partial x_j''}\,\delta_{iq} - \frac{\partial \lambda_q}{\partial x_i''} - \frac{\partial \lambda_i}{\partial x_q''}\right]\frac{\partial P}{\partial x_q''} + \text{ viscous term} \end{aligned} \tag{101}$$

Now we take the ensemble average on both sides and assume stationarity so that $\langle \partial \boldsymbol{v}''/\partial t \rangle = 0$. We know the solution to this equation when $\lambda_i = 0$, where the peculiar thing is that all terms vanish. This means that there are no zero order terms in $\frac{\partial \left\langle v_q'' v_i'' \right\rangle}{\partial x_q''}$ and $\frac{\partial \langle P \rangle}{\partial x_q''}$, and since we only intend to keep terms up to first order the averaged equation reduces to

$$\frac{\partial \left\langle v_q'' v_i'' \right\rangle}{\partial x_q''} - \frac{\partial}{\partial x_q''} \left\langle v_i^0 \, v_q^0 \right\rangle \frac{\partial \lambda_j}{\partial x_j''} + \left\langle v_p^0 \, v_q^0 \right\rangle \frac{\partial^2 \lambda_i}{\partial x_p'' \partial x_q''} = -\frac{\partial \langle P \rangle}{\partial x_i''} + \langle \text{ viscous term} \rangle \quad (102)$$

where v_p^0 is the *un-perturbed* wind field. We notice that a lot of terms have now disappeared, and we should probably be careful with the interpretation of what is left. A random stirring force added to the Navier-Stokes equation also vanishes on averaging, but that does not mean that a random stirring force has no effect.

3.3 Revised LINCOM

We now proceed in the spirit of the derivation of the LINCOM equations. We therefore set $\lambda_1 = \lambda_2 = 0$ and $\lambda_3 = h$. Then $\frac{\partial \lambda_j}{\partial x_j''} = 0$ automatically so that we can drop the second term on the left hand side of (102). In the third term on the lhs we make the approximation

$$\left\langle v_p^0 \, v_q^0 \right\rangle \approx V_p \, V_q \quad (103)$$

where V_p is a short hand notation for the un-perturbed mean velocity $\left\langle v_p^0 \right\rangle$. We also drop the viscous terms.
Then we make a Fourier transform with respect to the variables x and y, which are replaced by wave number variables k_1 and k_2. This yields the following equations

$$\begin{aligned} ik_q \left\langle v_q'' v_1'' \right\rangle + \frac{\partial}{\partial z} \left\langle v_3'' v_1'' \right\rangle &= -ik_1 P \\ ik_q \left\langle v_q'' v_2'' \right\rangle + \frac{\partial}{\partial z} \left\langle v_3'' v_2'' \right\rangle &= -ik_2 P \\ ik_q \left\langle v_q'' v_3'' \right\rangle + \frac{\partial}{\partial z} \left\langle v_3'' v_3'' \right\rangle - k_q V_p k_p V_q \, h &= -\frac{\partial P}{\partial z} \end{aligned} \quad (104)$$

Next, we write $\boldsymbol{v}''$ as

$$\boldsymbol{v}'' = \boldsymbol{v}^0 + \tilde{\boldsymbol{v}} \quad (105)$$

A crucial point is the following first order closure assumption for the advection term

$$ik_q \left\langle v_q'' v_i'' \right\rangle + \frac{\partial}{\partial z} \left\langle v_3'' v_i'' \right\rangle \approx ik_q \left\langle \tilde{v}_q \right\rangle V_i + ik_q \, V_q \, \langle \tilde{v}_i \rangle - \frac{\partial}{\partial z} K \frac{\partial \langle \tilde{v}_i \rangle}{\partial z} \quad (106)$$

where index q runs from 1 to 2 (there is no k_3). It is understood here that we are dealing with the (partially) Fourier transformed fields so that the 'eddy diffusivity' K is a function of $\boldsymbol{k}$ and z. When we transform back to real space the term will become a convolution of K and $\langle \tilde{\boldsymbol{v}} \rangle$ in the x and y coordinates, which may not be a bad way to model the term. In LINCOM K is independent of z. As a further approximation the logarithmic variation of $\boldsymbol{V}$ with z is neglected. This means that terms involving $\partial \boldsymbol{V}/\partial z$ are discarded and that a z-independent value of $\boldsymbol{V}^r = \boldsymbol{V}(z_r)$, for a suitably chosen reference height z_r, is used. With all these approximations, of which the use of a constant $\boldsymbol{V}^r$ might be the most problematic, we finally arrive at the following set of equations

$$
\begin{aligned}
ik_q\, V_q^r\ \langle\tilde{v}_1\rangle - \frac{\partial}{\partial z} K \frac{\partial\,\langle\tilde{v}_1\rangle}{\partial z} &= -ik_1 P \\
ik_q\, V_q^r\ \langle\tilde{v}_2\rangle - \frac{\partial}{\partial z} K \frac{\partial\,\langle\tilde{v}_2\rangle}{\partial z} &= -ik_2 P \\
ik_q\, V_q^r\ \langle\tilde{v}_3\rangle - \frac{\partial}{\partial z} K \frac{\partial\,\langle\tilde{v}_3\rangle}{\partial z} - k_p V_p^r k_q V_q^r\, h(\boldsymbol{k}) &= -\frac{\partial P}{\partial z} \\
ik_j \left\langle\tilde{v}_q\right\rangle + \frac{\partial\,\langle\tilde{v}_3\rangle}{\partial z} &= 0 \qquad (107)
\end{aligned}
$$

This system of linear equations is identical to that in LINCOM except that the inhomogeneous term, involving h, is lacking in LINCOM. Solutions are obtained as the sum of a solution to the homogeneous system (as in LINCOM) and a particular solution to the inhomogeneous system. Thus the general solution may be written as

$$
\begin{pmatrix} \langle\tilde{v}_1\rangle \\ \langle\tilde{v}_2\rangle \\ \langle\tilde{v}_3\rangle \\ P \end{pmatrix} = A_1 \mathrm{e}^{\alpha z} \begin{pmatrix} k_2 \\ -k_1 \\ 0 \\ 0 \end{pmatrix} + A_2 \mathrm{e}^{\alpha z} \begin{pmatrix} ik_1 \\ ik_2 \\ \boldsymbol{k}^2/\alpha \\ 0 \end{pmatrix} + B \mathrm{e}^{-|\boldsymbol{k}|z} \begin{pmatrix} ik_1 \\ ik_2 \\ -|\boldsymbol{k}| \\ -C \end{pmatrix} + \begin{pmatrix} 0 \\ 0 \\ -i\boldsymbol{k}\cdot\boldsymbol{V}^r\, h(\boldsymbol{k}) \\ 0 \end{pmatrix} \qquad (108)
$$

where A_1, A_2 and B are arbitrary constants, $C = i\boldsymbol{k}\cdot\boldsymbol{V}^r - \boldsymbol{k}^2 K$ and $\alpha = \sqrt{\frac{i\boldsymbol{k}\cdot\boldsymbol{V}^r}{K}}$. The square root for which $\mathrm{Re}\,\alpha < 0$ should be chosen in order to get a bounded solution. The solution involving $\mathrm{e}^{+|k|z}$ must be discarded for the same reason. The two first terms are the inner solutions, the third term is the outer solution and the last term is the particular solution. The arbitrary constants are fixed by the boundary condition $\left\langle\tilde{\boldsymbol{v}}\right\rangle = 0$ at the ground, which leads to

$$
\begin{aligned}
A_1(\boldsymbol{k}) &= 0 \\
A_2(\boldsymbol{k}) &= -B(\boldsymbol{k}) \\
B(\boldsymbol{k}) &= -\frac{i\boldsymbol{k}\cdot\boldsymbol{V}^r\, h(\boldsymbol{k})}{\boldsymbol{k}^2/\alpha + |\boldsymbol{k}|} \qquad (109)
\end{aligned}
$$

Taking the Fourier transform we obtain the perturbation $\tilde{\boldsymbol{v}}(\boldsymbol{x})$. This should be added to the zero order profile. Following LINCOM we choose this to be a logarithmic profile $\boldsymbol{V}$, even if different constant profiles have been used for different Fourier components. This does not spoil mass conservation. Changing back to the original coordinates we finally get

$$
\begin{aligned}
\langle v_1\rangle &= V_1(z-h) + \sum_{\boldsymbol{k}} \langle\tilde{v}_1(\boldsymbol{k}, z-h)\rangle\ \mathrm{e}^{i\boldsymbol{k}\cdot\boldsymbol{x}} \\
\langle v_2\rangle &= V_2(z-h) + \sum_{\boldsymbol{k}} \langle\tilde{v}_2(\boldsymbol{k}, z)\rangle\ \mathrm{e}^{i\boldsymbol{k}\cdot\boldsymbol{x}} \\
\langle v_3\rangle &= \sum_{\boldsymbol{k}} \langle\tilde{v}_3(\boldsymbol{k}, z-h)\rangle\ \mathrm{e}^{i\boldsymbol{k}\cdot\boldsymbol{x}} + \langle\boldsymbol{v}\rangle\cdot\nabla h \qquad (110)
\end{aligned}
$$

The results for $\langle v_1\rangle$ and $\langle v_2\rangle$ are very similar to those in LINCOM. The difference is that LINCOM uses two different constant velocities $\boldsymbol{V}(L)$ and $\boldsymbol{V}(l)$. One is used to specify boundary conditions and the other is used for the governing equations. On top of this both depend on $\boldsymbol{k}$. This is very confusing, and it has almost no impact on the numerical results if l and L are both set equal to $1/|k|$. With $z_r = l = L$ the horizontal components of the two models are identical. The revised vertical component $\langle v_3\rangle$ is, on

the other hand, radically different from LINCOM. Note that we may write this component as

$$\langle v_3 \rangle = \sum_{\boldsymbol{k}} B(\boldsymbol{k}) \left[-\boldsymbol{k}^2/\alpha \mathrm{e}^{\alpha(z-h)} - |\boldsymbol{k}| \mathrm{e}^{-|\boldsymbol{k}|(z-h)} \right] \mathrm{e}^{i\boldsymbol{k}\cdot\boldsymbol{x}} + \sum_{\boldsymbol{k}} i\boldsymbol{k}\cdot[\boldsymbol{V}(z-h) - \boldsymbol{V}(z_r - h)]\, h(\boldsymbol{k}) \tag{111}$$

The first sum term on the right hand side vanishes for $z \to \infty$, but the second sum does not. This is an artifact caused by the inconsistent adoption of a flat velocity profiles in the calculations.

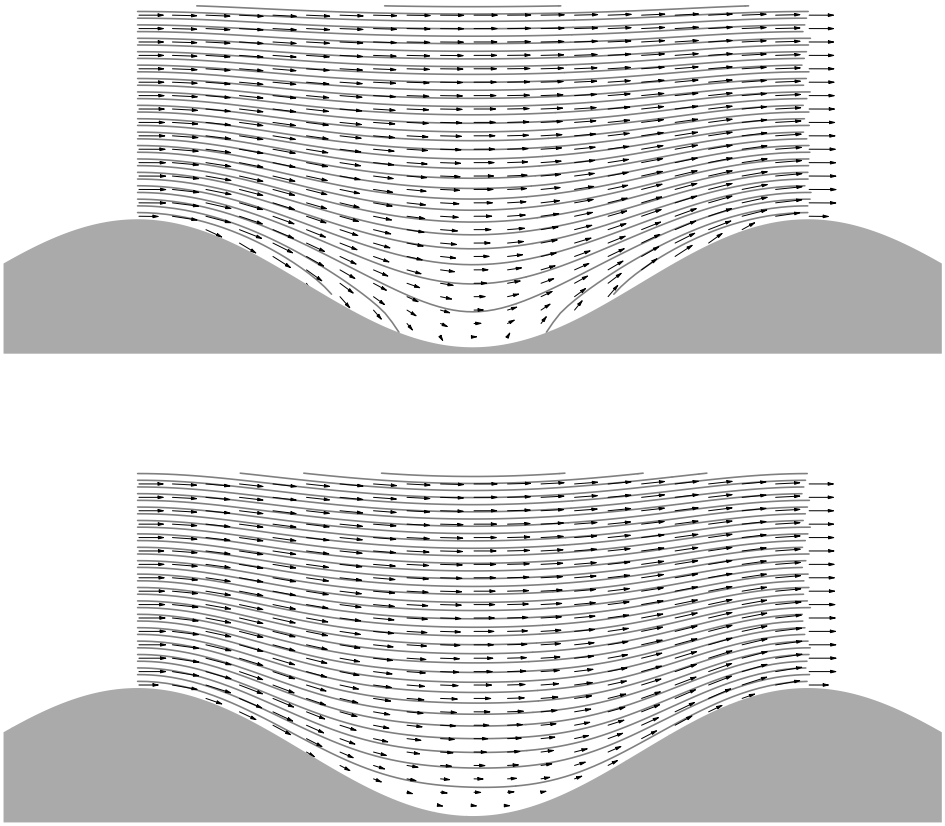

Figure 32. Flow field over sinusoidal orography with maximum slope 0.6. Upper: LINCOM model. Lower: revised LINCOM model.

A series of sinusoidal hills, $h(x, y) = A \sin kx$, with the wind direction perpendicular to the ridges, can be used as a test example. Figure 32 shows results for LINCOM and the revised LINCOM. The LINCOM streamlines clearly have strange features: they are vertical at the surface so that air is emerging from the ground at the uphill slope and is sucked into the hill at the downhill slope. At the same time the steamlines are pushed away from the hill, probably because of violation of the mass balance which introduces spurious bulk sources. The corrected equations do not violate mass conservation, and behave much nicer. The flow runs parallel with the ground and with a compression of streamlines at the summit as expected. The maximum slope is 0.6 in this case and a recirculation zone at the trough could have been expected, and a recirculation zone does appear for slopes steeper than about 0.7. Real flows separate at much lower slopes. Separation of the model flow is illustrated in figure 33 (upper) where the maximum slope is 1. The fact that the revised equations can produce recirculation zones is reassuring, but the accuracy of the prediction should be questioned. The perturbation must be larger than the unperturbed velocity for this to happen, so a first order approximation is probably

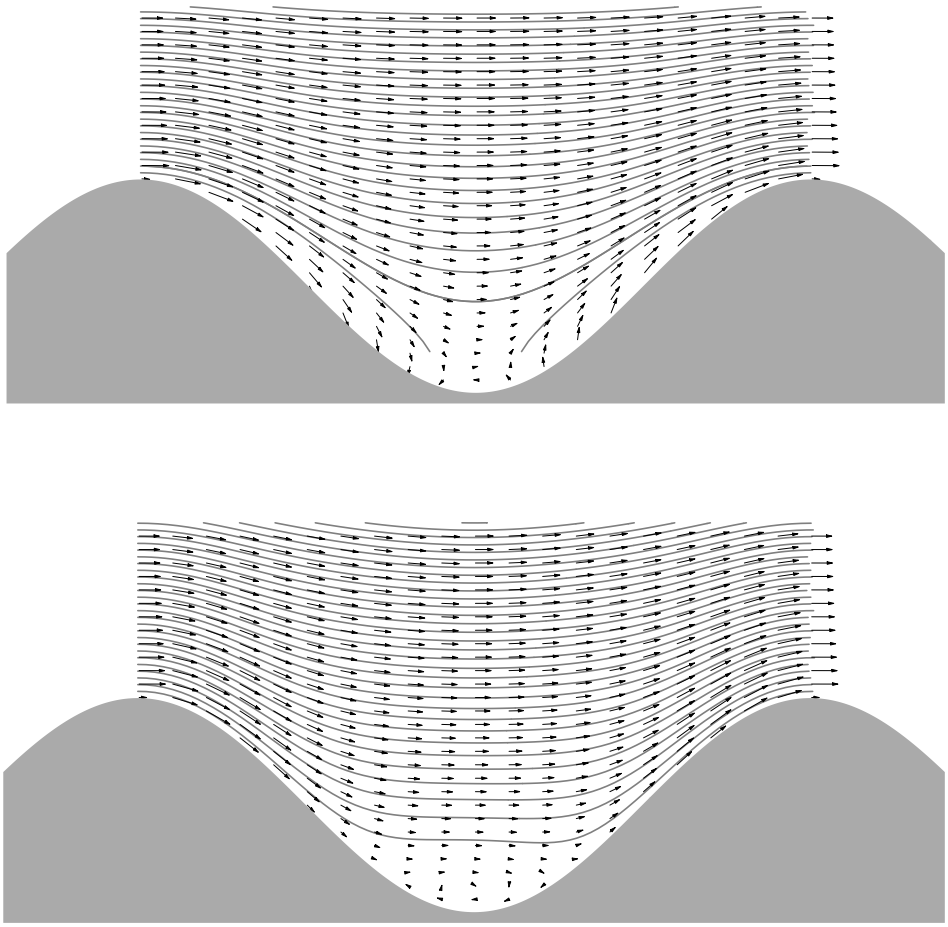

Figure 33. Flow field over sinusoidal orography with maximum slope 1.0. Upper: LINCOM model. Lower: revised LINCOM model.

inadequate. In this model streamlines have the same reflection symmetries as the terrain, therefore the recirculation zone is symmetric around the trough, which is an unwanted feature. Real hills exert a drag force caused by higher pressures on the sides facing the wind, but the symmetry means that the net drag force is zero. It should be noted that the symmetry is broken by terms like $\tilde{v_3}\partial V_i/\partial z''$, which appears in the equations for a non-constant V_i.

As we have seen the application of a stricter derivation procedure leads to corrections of LINCOM, which removes unphysical features at no extra computational cost. Therefore there is every reason to implement these corrections. It is a minimal repair copying LINCOM as far as possible. It is likely that we could do even better if a logarithmic velocity profile was used.

3.4 First order equations

It seems natural to investigate the first order equations as they come out of the derivation described above without further approximations. This means letting $\boldsymbol{V}$ and K vary with height. The extra computational work could be a good investment, and it would ensure a well defined set of governing equations. The plan is to start with a closed set of equations, apply a transformation that straightens the boundary, make a first order approximation and solve the equations. We choose the following closure

$$\langle \boldsymbol{v} \rangle \cdot \nabla \langle \boldsymbol{v} \rangle = -\nabla \langle P \rangle + \frac{\partial}{\partial z} K \frac{\partial}{\partial z} \langle \boldsymbol{v} \rangle \tag{112}$$

where

$$K = \kappa\, u_*\,(z - h(x,\,y)) = \kappa\, u_*\, z'' \tag{113}$$

A more fancy closure such as $\nabla_j K(\nabla_j v_i + \nabla_i v_j)$ could be tried here, the extra terms are in fact quite harmless. However, we wish to keep things as simple as possible, and the proposed closure might still catch much of the right behaviour.

Next we apply the coordinate transformation $x_i'' = x_i - \delta_{i3}\, h$ and define the transformed velocity $v_i'' = v_i + \delta_{3i}\, \boldsymbol{v} \cdot \nabla h$, as was done above. The transformed equation becomes (we drop the brackets from now on)

$$\boldsymbol{v}'' \cdot \nabla \left(v_i'' + \delta_{3i}\, \boldsymbol{v}'' \cdot \nabla h\right) = -\nabla_i P + \frac{\partial P}{\partial z''} \nabla_i h + \frac{\partial}{\partial z''} K \frac{\partial}{\partial z''} \left(v_i'' + \delta_{3i}\, \boldsymbol{v}'' \cdot \nabla h\right) \tag{114}$$

Then we insert $\boldsymbol{v}'' = \boldsymbol{V} + \tilde{\boldsymbol{v}}$, where $\tilde{\boldsymbol{v}}$ is the perturbation and expand to first order in h. This yields the following equation:

$$\tilde{\boldsymbol{v}} \cdot \nabla V_i + \boldsymbol{V} \cdot \nabla \tilde{v}_i + \delta_{3i} (\boldsymbol{V} \cdot \nabla)^2\, h = -\nabla_i P + \frac{\partial}{\partial z''} K \frac{\partial}{\partial z''} \tilde{v}_i \tag{115}$$

This is an inhomogeneous system of linear equation in $\boldsymbol{v}$ with the important property that all coefficients depend only on z''. This means that the partial Fourier transform decouples the problem into *independent* ordinary differential equations. This is a major simplification because the equations can be solved separately for each $\boldsymbol{k}$ without having to solve implicit equations. The reason for this is the lack of a self advection term $\boldsymbol{v} \cdot \nabla \boldsymbol{v}$ which would convolute the Fourier components. The term is of second order and should probably only be admitted together with all other second order terms. After a partial Fourier transform we end up with (please recall that $\boldsymbol{k} = (k_1,\, k_2,\, 0)$)

$$\begin{aligned}
i\boldsymbol{k} \cdot \boldsymbol{V} \tilde{\boldsymbol{v}}_i + \tilde{v}_3 \frac{\partial}{\partial z''} V_i &= -i k_i P + \frac{\partial}{\partial z''} K \frac{\partial}{\partial z''} \tilde{v}_i \qquad \text{for } i = 1, 2 && (116)\\
i\boldsymbol{k} \cdot \boldsymbol{V} \tilde{\boldsymbol{v}}_3 + (i\boldsymbol{k} \cdot \boldsymbol{V})^2\, h &= -\frac{\partial P}{\partial z''} + \frac{\partial}{\partial z''} K \frac{\partial}{\partial z''} \tilde{v}_3 && (117)\\
i\boldsymbol{k} \cdot \tilde{\boldsymbol{v}} + \frac{\partial \tilde{v}_3}{\partial z''} &= 0 && (118)
\end{aligned}$$

We could have obtained the same equations if we had let $\boldsymbol{V}$ be a function of z'' in (107). In other words, the simple closure can be applied before or after the coordinate transformation with the same result. This is not so for the 'more fancy' closure mentioned above, where extra terms are generated if the closure is applied first. These terms ensure the right asymptotic behaviour, therefore the correct procedure is to apply the closure first.

Contracting both sides of (116) with k_i and inserting $i\boldsymbol{k} \cdot \tilde{\boldsymbol{v}} = -\partial \tilde{v}_3 / \partial z''$ we get two equations for $\tilde{v}_3$ and P

$$\begin{aligned}
-i\boldsymbol{k} \cdot \boldsymbol{V} \frac{\partial \tilde{v}_3}{\partial z''} + \tilde{v}_3 \frac{\partial i\boldsymbol{k} \cdot \boldsymbol{V}}{\partial z''} &= \boldsymbol{k}^2 P - \frac{\partial}{\partial z''} K \frac{\partial^2 \tilde{v}_3}{\partial z''^2}\\
i\boldsymbol{k} \cdot \boldsymbol{V} \tilde{\boldsymbol{v}}_3 + (i\boldsymbol{k} \cdot \boldsymbol{V})^2\, h &= -\frac{\partial P}{\partial z''} + \frac{\partial}{\partial z''} K \frac{\partial}{\partial z''} \tilde{v}_3 && (119)
\end{aligned}$$

Differentiating the second of these equations with respect to z'' and adding the result to the first equation yields two coupled second order differential equations:

$$\begin{aligned}
2\,(\tilde{v}_3 + i\boldsymbol{k} \cdot \boldsymbol{V} h)\, \frac{\partial i\boldsymbol{k} \cdot \boldsymbol{V}}{\partial z''} &= \boldsymbol{k}^2 P - \frac{\partial^2 P}{\partial z''^2} + \frac{\partial}{\partial z''} K' \frac{\partial \tilde{v}_3}{\partial z''} && (120)\\
(i\boldsymbol{k} \cdot \boldsymbol{V})(\tilde{v}_3 + i\boldsymbol{k} \cdot \boldsymbol{V}\, h) &= -\frac{\partial P}{\partial z''} + \frac{\partial}{\partial z''} K \frac{\partial}{\partial z''} \tilde{v}_3 && (121)
\end{aligned}$$

Solving these equations we obtain $\tilde{v}_3$, P and $i\boldsymbol{k}\cdot\tilde{\boldsymbol{v}} = -\partial\tilde{v}_3/\partial z''$. Contracting both (116) with $\hat{\boldsymbol{k}} \equiv (-k_2, k_1, 0)$ yields an equation for the second horizontal component $\hat{\boldsymbol{k}}\cdot\tilde{\boldsymbol{v}}$

$$i\boldsymbol{k}\cdot\boldsymbol{V}\,\hat{\boldsymbol{k}}\cdot\tilde{\boldsymbol{v}} + \tilde{v}_3\frac{\partial\hat{\boldsymbol{k}}\cdot\boldsymbol{V}}{\partial z''} = \frac{\partial}{\partial z''}K\frac{\partial\hat{\boldsymbol{k}}\cdot\tilde{\boldsymbol{v}}}{\partial z''} \tag{122}$$

3.5 Higher orders

The higher order equations are derived replacing h with ϵh in (114), inserting

$$v'' = \sum_{n=0}^{\infty}\tilde{\boldsymbol{v}}^{(n)}\,\epsilon^n \tag{123}$$

and

$$P = \sum_{n=0}^{\infty}P^{(n)}\,\epsilon^n \tag{124}$$

and equate terms of order ϵ^n. Due to the product in the advection term, the nth equation will only contain perturbations of orders lower than or equal to n. The equations should therefore be solved sequentially starting with $n = 0$, then $n = 1$, $n = 2$ etc. In this way $\tilde{\boldsymbol{v}}^{(n)}$ and $P^{(n)}$ are the only unknowns in the nth equation. Collecting known terms into a 'source term' $S_i^{(n)}$ we may write the resulting equations as

$$\tilde{\boldsymbol{v}}^{(n)}\cdot\nabla V_i + \boldsymbol{V}\cdot\nabla\tilde{\boldsymbol{v}}_i^{(n)} = -\nabla_i P^{(n)} + \frac{\partial}{\partial z''}K\frac{\partial}{\partial z''}\tilde{v}_i^{(n)} + S_i^{(n)} \tag{125}$$

We see that all the equations have the same structure and therefore could be solved by the same algorithm. We also not that a partial Fourier transform decouples the equations into one separate set of equations for each Fourier component. The source term $S_i^{(n)}$ contains products so its Fourier transform is a mixture of Fourier components. The easiest way to obtain $S_i^{(n)}(\boldsymbol{k})$ is probably to transform $\tilde{\boldsymbol{v}}_i^{(p)}$ and $P^{(p)}$ $(p < n)$ to real space, make the products and transform back again. This may require lots of RAM.

3.6 Boundary conditions

The boundary conditions are tricky. The logarithmic profile is divergent for $z \to 0$ and therefore does not seem to comply with a no-slip condition. In reality there is no divergence and the meaning of the logarithmic profile is that $z\exp -V(z)/(zV'(z))$ takes on the constant value z_0 when z is within the surface layer and outside the viscous layer next to the ground. According to surface layer similarity the surface layer is controlled by the momentum flux $(-u_*^2)$ and the surface is characterized by z_0. In other words, the surface layer above the viscous layer does not care how the momentum flux is produced as long as u_* and z_0 are the same. If we want to, we can control the local forcing by putting conveyer belts on every square meter of surface. The conveyer belts should be equipped with controllers able to adjust the speed so as to maintain predetermined values of u_* and z_0. If the conveyer belts are smooth (but still giving no slip) and the viscosity is very small, the velocity at the ground becomes very large and negative. The logarithmic divergence therefore appears in the limit $\nu \to 0$. We should therefore not worry about non–zero tangential wind component at the ground. But even if the divergence is physically sound, it is annoying that the perturbation $(\boldsymbol{V}\cdot\nabla)^2 h$ is divergent at the ground. In order to make things more regular we add a finite viscosity term to K, i.e. $K = \kappa u_*(z + z_1)$. The corresponding mean profile is $V(z) = u_*/\kappa\,\log((z + z_1)/z_0)$, Where we put z_0 in the denominator in order to get the right *asymptotic* value of z_0. The boundary conditions are then that the tangential wind components vanish for $z = z_1 - z_0$ and the normal component vanished for $z = 0$. Evidently $z_1 = z_0$ is a natural choice because it is just no–slip conditions at $z = 0$.

In Section 3.2 we found three second order differential equations for P, $\tilde{v_3}$ and $\hat{\boldsymbol{k}} \cdot \tilde{\boldsymbol{v}}$ and the algebraic relation $i\boldsymbol{k}\tilde{\boldsymbol{v}} + \frac{\partial \tilde{v}_3}{\partial z''} = 0$. We therefore need six boundary conditions of which we found three in the preceding paragraph. The remaining three must be fixed by the requirement that the perturbations remain bounded for $z \to \infty$ and by specified the momentum forcing. Alternatively, if the Coriolis force is included, we must specify the geostrophic wind.

When z_0 is non-uniform the boundary condition at the ground is that

$$\int \tilde{v}_3(z_0(\boldsymbol{x}, \boldsymbol{k}))\mathrm{e}^{i\boldsymbol{k}\cdot\boldsymbol{x}}\,\mathrm{d}^2x = 0 \tag{126}$$

There is a problem if z_0 varies, because we wish to keep K only as a function of z (or actually z'') so that the equations separate in the $\boldsymbol{k}$ domain. Surface roughness variations are important so we have to be able to deal with them. In LINCOM this is done by introducing a separate perturbation problem for variations of $\log(z_0/\overline{z}_0)$, where $\overline{z}_0$ is a suitable average value of z_0. This restores the separation of equations for Fourier components, but with two perturbation expansions on top of each other the number of terms very soon becomes enormous.

When the Coriolis force is neglected, a logarithmic profile should exist high above the terrain. The friction velocity u_*, corresponding to the asymptotic logarithmic profile, is determined by the square root of the momentum flux, which is assumed to be given. Close to the ground we also expect a local logarithmic profile, but with a different (local) friction velocity. This is due to form drag of the orography. Likewise the friction velocity corresponding to the upper profile is not the same as the local z_0 on the ground, even when z_0 is the same everywhere. This is because the upper profile sees the orography as roughness. In WAsP end WAsP Engineering the geostrophic wind is used as upper boundary condition. It might be a good idea to include the Coriolis force together with this boundary condition.

3.7 An alternative

To first order each Fourier component is treated separately, which, to some extend, justifies the use of a different K for each mode. Since K is large, the model flow is laminar, as for any other eddy viscosity model. It therefore seems natural to use a solution to a real laminar flow in order to maintain some degree of realism. In LINCOM the unperturbed flow is laminar with full–slip at the boundary. On the other hand we used a no–slip boundary condition for the perturbation. This lack of consequence makes it impossible to relate the solution to a physical problem. If the full–slip condition is applied also to the perturbation the equations get under–determined. The probable explanation for this is that the lack of friction makes more than one solution possible. If we try no–slip conditions for the unperturbed field then the only constant profile is $V_1 = 0$ and nothing will work. A viable alternative is to keep the no slip condition and let the momentum flux be constant. In that case the unperturbed profile is linear, $V_1(z) = \alpha z$, which may not be any worse than a constant profile. For the constant momentum flux we have $u_*^2 = K\alpha$, where u_* should be a parameter of the problem. As the second parameter we can use the observed wind speed at the reference height z_r so that $\alpha = U(z_r)/z_r = u_*/\kappa l$ and $K = \kappa u_* l$, where $l \equiv z_r/\log(z_r/z_0)$. The results will of course depend on the choice of z_r (or l), but you can't have everything (unless you use a logarithmic profile).

For a sinusoidal orography, $h(x) = 2h_k \cos kx$, with $\boldsymbol{V}$ along the x–axis, the resulting equations can be written in non-dimensional form. To this end we define

$$s \equiv kz'' \tag{127}$$

$$\psi \equiv (v_3 + i\alpha s h_k)/u_* \tag{128}$$

$$p \equiv \frac{kP}{u_* \alpha} \tag{129}$$

Inserting this into (119) leads to the following equations

$$-is\,\frac{\partial \psi}{\partial s} + i\,\psi = p - (\kappa kl)^2 \frac{\partial^3 \psi}{\partial s^3} \tag{130}$$

$$is\,\psi = -\frac{\partial p}{\partial s} + (\kappa kl)^2\,\frac{\partial^2 \psi}{\partial^2 s} \tag{131}$$

Elimination of p leads to the equation

$$\left(\frac{\partial^2}{\partial s^2} - \frac{is}{(\kappa kl)^2}\right)\left(\frac{\partial^2}{\partial s^2} - 1\right)\psi = 0 \tag{132}$$

The factorization of the operator on the lhs is the simplification we get from assuming a simple profile. It may not seem much, but it does simplify the solution procedure. I have not been able to obtain the same for a logarithmic profile. The solution to (132) for which $\psi(0) = 0$, $\psi'(0) = i\alpha h_k/u_*$ and $\psi(s)$ is bounded for $s \to \infty$ can be written as

$$\psi(s) = i\frac{h_k}{\kappa l}\left[\sinh s - \frac{\int_0^s A(s')\,\sinh(s-s')\,\mathrm{d}s'}{\int_0^\infty A(s')\,\mathrm{e}^{-s'}\,\mathrm{d}s'}\right] \tag{133}$$

where

$$A(s) = Ai(\mathrm{e}^{-i\pi/6}(\kappa kl)^{-2/3}s) \tag{134}$$

and Ai is an Airy function. The other Airy function, Bi, produces unbounded solutions for $s \to \infty$, hence we drop it. (A linear combination of the two Airy functions should be used in case of an upper boundary at finite height).

The horizontal flow field component v_1 is determined from the continuity equation, i.e.

$$v_1(z,k) = -iu_*\psi'(kz) + \alpha h(k) \tag{135}$$

The last term is a constant ensuring that $v_1 = 0$ at the boundary. Note that $v_1 \to \alpha h$ for $z \to \infty$, where $v_1 \to 0$ might have been expected. The perturbation therefore does not vanish (although the ratio v_1/V does). This probably has to do with the fact that the $\partial V/\partial z$ remains finite for $z \to \infty$.

The flow field is shown in figure 34. The input are: maximal slope is 0.6, $z_r = 10\mathrm{m}, 2\pi/k = 500\mathrm{m}$ and $z_0 = 0.03\mathrm{m}$. This model produces flow separates much more willingly than the modified LINCOM model. A large recirculation zone is seen at the trough and separation persists down to maximum slopes of about 0.04. Figure 35 shows results for maximum slope 0.05. Flow separation is not expected at this low slope. On the other hand, wind tunnel experiments indicate that separation zones are shifted away from the trough towards the downhill slope, and the model actually does that.

Flow over sinusoidal hills has been investigated in a wind tunnel experiment by Athanassiadou and Castro (2001). Three orographies were used: a reference case on a flat, a sinusoidal 'small hill' case with maximum slope 0.2, and a 'large hill' case with maximum slope 0.4. The same roughness cover was used in all three cases and the period λ was the same for the two hill cases. The small hill was designed to be just below the onset of separation, which was confirmed by the experiment. A separation zone was observed on the large hill stretching from about halfway down the down–hill slope to right after the trough. This behaviour is nicely reproduced by the model as can be seen in figures 36 37. In the figures the reference height is set equal to the boundary layer height (obtained from the flat case), but further calculations show that the choice of reference height markedly influences the results. Choosing a somewhat lower reference heights the model

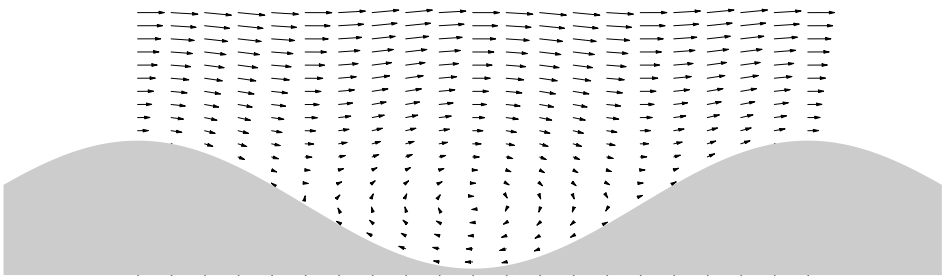

Figure 34. Flow field over sinusoidal orography with maximum slope 0.6.

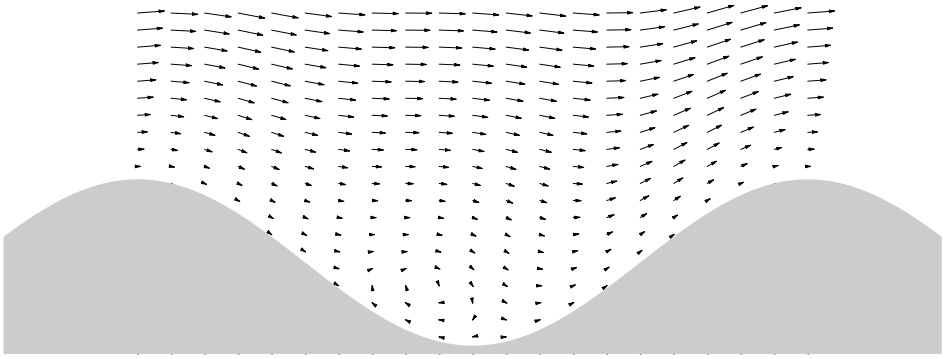

Figure 35. Flow field over sinusoidal orography with maximum slope 0.05. Note that vertical dimensions have been scaled up.

flow separates on the small hill. The measurements include surface pressure data, which are valuable for model testing. The surface pressure varies something like a sine with the same period as the hill, minimum at the crest and maximum slightly after the trough on the up–hill slope. A larger content of higher harmonics is evident from the large hill compared to the small hill. First order theory can only provide the first harmonic, hence the experimental data indicate a need for higher order calculations. The model also predicts a linear dependence of the pressure on the slope, which is not observed. The best fit to the amplitude of the pressure variation now occurs for small reference heights, so it seems that a proper choice cannot be made. It is possible to compute the form drag of the hills directly from the pressure measurements. The measured form drag is consistent with the observed u_* taken from the logarithmic profile above the hills. For the small hill the form drag is about equal in magnitude to the friction drag, while it is about six times larger for the large hill. The values predicted by the model are generally of the right order of magnitude, but depend quite a lot on the chosen reference height.

Even if there are problems with fixing the reference height in the model, it does catch much of the qualitative behaviour.

3.7.1 Proof of (95)

A proof that $\boldsymbol{v}''$ is divergence free may go as follows. Consider a regular matrix M_{ij}. We recall that the determinant Det$M$ may be expanded in terms of the jth row , i.e.

$$\text{Det } M = \sum_i C_{ij}\, M_{ij} \tag{136}$$

where C_{ij} is equal to $(-1)^{i+j}$ times the determinant of the matrix that results from delet-

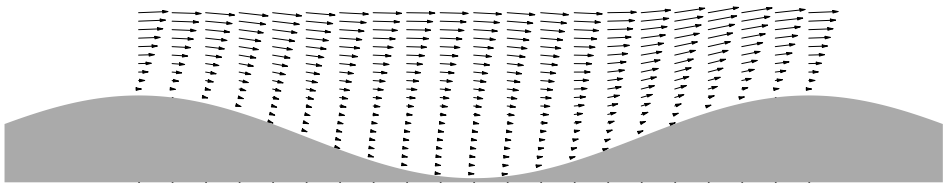

Figure 36. Flow field over the 'small hill'. Note that vertical dimensions have been scaled up.

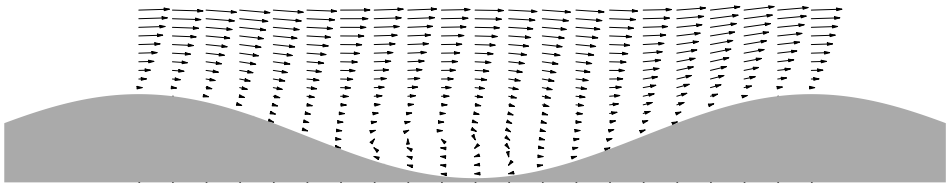

Figure 37. Flow field over the 'large hill'. Note that vertical dimensions have been scaled up.

ing the ith row and the jth column of M. In other words, $1/D\, C_{ij}$ is the inverse of M_{ij}. Since C_{ij} is independent of the element M_{ij}, we can express the differential of the matrix as

$$\mathrm{dDet}\ M = \mathrm{Det}\ M\ (M^{-1})_{ij}\, \mathrm{d}M_{ji} \tag{137}$$

Specializing this to $M_{ij} = \frac{\partial x_i}{\partial x_j''}$, we note that

$$\frac{\partial x_i}{\partial x_k''}\,\frac{\partial x_k''}{\partial x_j} = \delta_{ij} \tag{138}$$

so that $(M^{-1})_{ij} = \frac{\partial x_j''}{\partial x_i}$, and from (137)

$$\frac{\partial D}{\partial x_j} = D\,\frac{\partial x_p''}{\partial x_q}\,\frac{\partial}{\partial x_j}\,\frac{\partial x_q}{\partial x_p''} = -D\,\frac{\partial^2 x_p''}{\partial x_q \partial x_j}\,\frac{\partial x_q}{\partial x_p''} = -D\,\frac{\partial}{\partial x_p''}\,\frac{\partial x_p''}{\partial x_j} \tag{139}$$

where (138) was used in the second equality. Taking the divergence on both sides of (94) and using (139) we finally get

$$\begin{aligned}\frac{\partial v_i''}{\partial x_i''} &= D\frac{\partial x_i''}{\partial x_j}\frac{\partial v_j}{\partial x_i''} + v_j\,\frac{\partial x_i''}{\partial x_j}\frac{\partial D}{\partial x_i''} + v_j\,D\,\frac{\partial}{\partial x_i''}\frac{\partial x_i''}{\partial x_j} \\ &= D\frac{\partial v_j}{\partial x_j} + v_j\,\frac{\partial D}{\partial x_j} + v_j\,D\,\frac{\partial}{\partial x_i''}\frac{\partial x_i''}{\partial x_j} = D\,\frac{\partial v_j}{\partial x_j}\end{aligned} \tag{140}$$

4 KAMM2 simulations for Tauste

Due to large loads on wind turbines at the site Tauste in Northern Spain Gamesa Eólica and Vestas decided to investigate the flow in more detail. Two mast were instrumented by the company MetSupport and Risø National Laboratory as described in table 4. The heights are above ground level and for the sonic anemometers the brand is given in parentheses. The level 42.3 m corresponds to hub height and 18.7 m to the lowest position of the tip. This instrumentation is sufficient to give reliable information on shear, gusts, turbulence and possible influence of stability on the flow at the positions of the masts. In this investigation we are only trying to model the most simple aspect of the measurements, namely the mean wind as a function of height. Gusts and turbulence is *not* analyzed here.

Height [m]	Mast 1		Mast 2	
48	cup	vane	cup	
42.3	cup	sonic (Gill) term	cup	vane term
30.6	cup	sonic (Metek)	cup	sonic (Gill)
18.7	cup	sonic (Metek)	cup	vane
10	cup	vane term	cup	vane term

Table 4. Instrumentation of the two masts

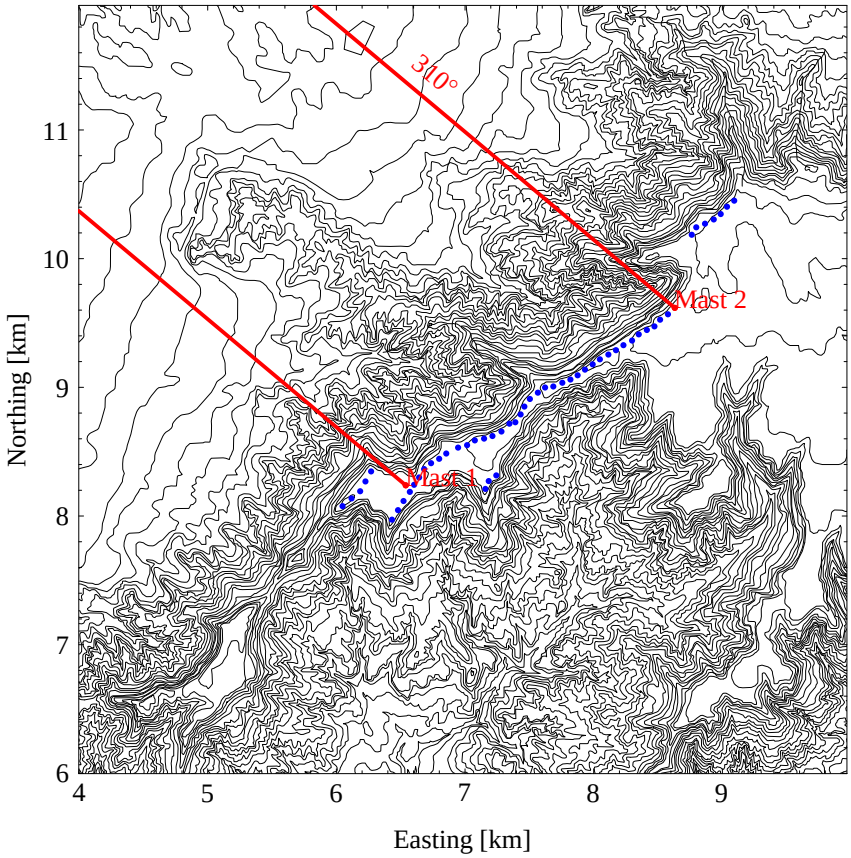

Figure 38. The two masts at Tauste together with positions of wind turbines. The lines indicate typical wind directions.

The positions of the masts are shown in figure 38.

4.1 Model issues

4.1.1 The KAMM2 mesoscale model

The Karlsruhe Atmospheric Mesoscale Model 2 (KAMM2) is a three-dimensional, non-hydrostatic and compressible mesoscale model (Adrian 1998) related to KAMM (Adrian and Fiedler 1991, Adrian 1994). Spatial derivatives are calculated in the model by central differences on a terrain following grid. The turbulent fluxes are parametrized using a mixing-length model with a non-local closure for the convective mixed layer. Lateral (i.e. the sides of the domain) boundary conditions assume zero velocity gradients normal to the inflow sides. On out-flow boundaries, the horizontal equations of motion are replaced by a simple wave equation allowing signals to pass out of the domain without reflection. Gravity waves are absorbed in the upper part of the computational domain which acts as damping layer. At initialization, the orography, roughness and large scale forcing are loaded into the model.

4.1.2 Independence of grid resolution

As when operating any finite difference model, it is necessary to run the model for different spatial grid resolutions in order to confirm that the model results are not sensitive to grid resolution. Normally, three different resolutions are employed. If the computational results of the two finest resolutions are close to each other it is an indication of that the model results approach a distinct solution for increasing grid resolution. In this way, an appropriate grid resolution can be chosen. When choosing very fine grid resolutions, the computational resource requirements may increase significantly. It may then be appropriate to allow some difference between model results for different resolutions.

4.1.3 Simulation time

A simulation time of several hours (physical model time - not computer CPU time) is necessary in order to approach a final state of the computational wind map. There is no specific correct way of deciding how much simulation time is necessary to complete a mesoscale model run. Rather, this depends on the judgment of the model operator. However, for the present work, it has been found appropriate to focus on the horizontal velocities, u and v, as they are the main variables of the computational results.

4.1.4 Sensitivity to non-smoothness of the grid

Like some finite difference models, KAMM2 is sensitive to non-smoothness of the computational grid. This is because change of elevation in the lower part of the grid is implemented via source terms containing Christoffel symbols in the equations of motion. The Christoffel symbols depend on the second derivatives of the elevation and become significant for non-smooth grids, thus making the source terms important in the model solution. The consequence is that, for complex terrain, the orography must be smoothed by filtering before the computational grid is generated. Otherwise, if the grid is not smooth, it may be very difficult to run the model although the model equations are formally correct. In practice, this is in particular a problem for high grid resolutions. Furthermore, it can become difficult to obtain grid independent solutions unless the orography is filtered appropriately.

4.1.5 Stand-alone operation of the model

KAMM2 is able to run as a “stand-alone” model, i.e. the mesoscale model can be run by using only the large scale forcing (see sketch in Figure 39) instead of being nested within a larger model supplying the boundary conditions.

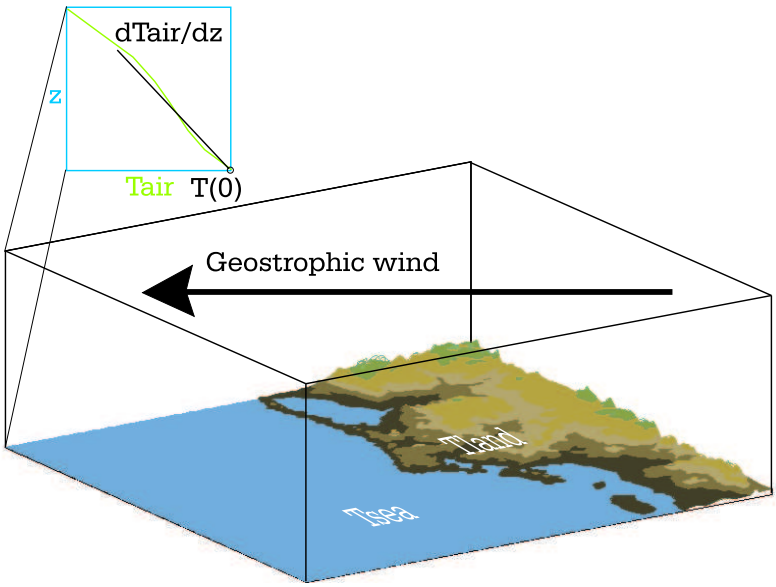

Figure 39. Sketch of the large scale forcing used for KAMM2.

4.2 Model setup for Tauste

4.2.1 Topography and filtering

The orography data with 50 m horizontal resolution was generated from the WAsP map file *Tauste.map* by using the WAsP utility *map2grd*. Prior to this, a few spurious elevation lines were removed from the WAsP map. The chosen map section is Easting 653km to 661km and Northing 4634km to 4642km (UTM32, ED50).

The orography data was filtered in real space via a binomial polynomial kernel using $n = 9$ points for each horizontal direction with the actual point in the center, i.e. by using the kernel centered at the index $i = j = 0$,

$$k(i,\ j) = \binom{n-1}{i+\frac{n-1}{2}}\binom{n-1}{j+\frac{n-1}{2}}, \quad -\frac{n-1}{2} \le i, j \le \frac{n-1}{2}, \tag{141}$$

normalized to give a unit sum. An additional horizontal zone, 600 m wide, was added around the boundary of the map prior to filtering by simple copying of the boundary points (resulting in flat squares by the corners of the map). This is because KAMM2 expects the elevation near the boundary to be constant in the horizontal direction normal to the boundary. The resulting map shown in Figure 40 has 185×185 grid points at 50 m resolution. Also shown in the figure are three transects used for comparing results.

Two additional maps with horizontal resolutions of 100 m and 200 m were generated from the filtered map by selecting every second and fourth point, respectively. These maps have 93×93 and 47×47 grid points.

The aerodynamic roughness length has been set uniformly to 0.03 m.

4.2.2 Vertical resolution

Based on experience, the vertical extension of the computational domain is chosen to be at least 5 km above terrain level and the lowest cells must lie within the inner layer of which the height is estimated by the relation by (Jensen et al. 1984),

$$\frac{l_i}{L}\ln^2\left(\frac{l_i}{z_0}\right) = 2\kappa^2, \tag{142}$$

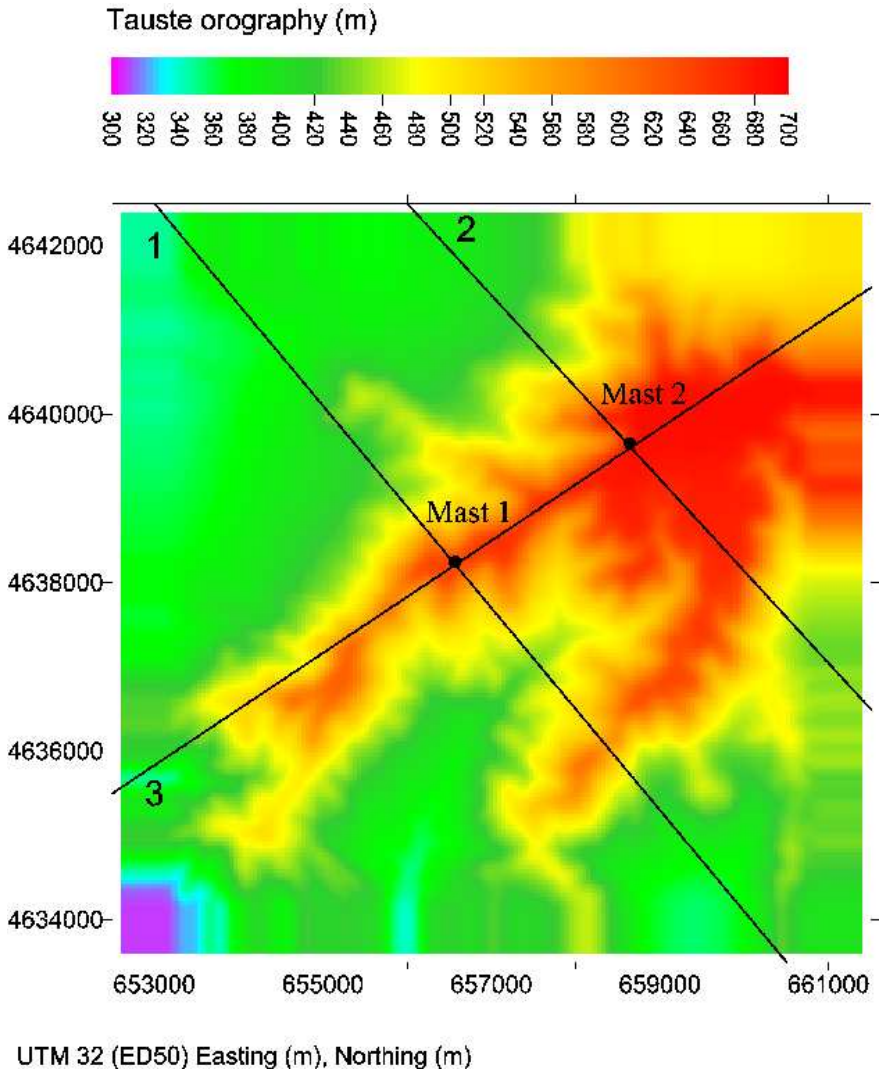

Figure 40. Orography of Tauste used for the mesoscale model. The three transects shown are used for comparing results. Each transect start at the end labeled by a number.

where L is the horizontal length scale of a hill, z_0 is the roughness length and κ is the von Kármán constant. Resolving features from topography elements of scales down to L for $z_0 = 0.03\ m$ yields

$$l_i = 5.78\ m, L = 500\ m, \tag{143}$$

$$l_i = 3.52\ m, L = 250\ m. \tag{144}$$

where the alternative values of L are based on the judgment of the model operator by regarding the orography shown in Figure 40. Using vertical parabolic stretching with 4 grid points below the height of 50 m (agl.) and 80 vertical grid points the lowest grid point is placed at a height of $h_1 = 5.9\ m$ over the lowest part of the terrain. This corresponds to the value of $L = 500\ m$. Using 100 vertical grid points with 6 grid points below the height of 50 m (agl.) the lowest grid point is placed at $h_1 = 3.4\ m$ over the lowest part of the terrain. This corresponds to the value of $L = 250\ m$. It is of course desirable to resolve the lowest part of the atmospheric boundary layer with as many grid points as possible within the scope of the study in order to investigate the negative shear at heights of order of the assumed hub height 50 m. However, it is not known how well the simple mixing length model for the turbulence responds to very fine vertical resolutions. It would

be desirable to investigate this matter further.

4.2.3 Model test cases

A strategy has been applied to the computer simulations in which the KAMM2 model was first tested with different filtering schemes for the orography and different horizontal and vertical grid resolutions for verifying grid independence of the model solutions for Tauste. Second, different large scale forcing, in particular different temperature conditions, was tested in order to investigate the local atmospheric conditions that may lead to negative shear at the positions of the two measuring masts. Most of the effort was put into generating reliable model solutions. More effort in the direction of testing different large scale forcing and perhaps different turbulence model schemes is somewhat lacking in the present study. However, it was found necessary to investigate the validity of the results generated by the mesoscale model. In Table 5 an overview is given for the cases simulated with KAMM2.

Table 5. Overview of cases simulated with KAMM2.

case	$\Delta x, \Delta y\ (m)$	NZ	$u_g\ \left(\frac{m}{s}\right)$	$v_g\ \left(\frac{m}{s}\right)$	$\frac{\Delta T}{\Delta z}\ \left(\frac{K}{m}\right)$	$\Delta T_{land}\ (K)$	comments
1	50	80	7.5	-6.5	-0.0065	0.0	
	100	80	7.5	-6.5	-0.0065	0.0	
	200	80	7.5	-6.5	-0.0065	0.0	
2	100	80	8.0	-6.0	-0.0098	-3.0	day
3	50	100	7.5	-6.5	-0.0065	0.0	
	100	100	7.5	-6.5	-0.0065	0.0	
	200	100	7.5	-6.5	-0.0065	0.0	
4	50	100	7.5	-6.5	-0.0065	0.0	filter at 25 m
	100	100	7.5	-6.5	-0.0065	0.0	filter at 25 m
	200	100	7.5	-6.5	-0.0065	0.0	filter at 25 m
5	100	100	14.1	-5.1	-0.0098	-3.0	day
6	100	100	9.4	-3.4	-0.0050	3.0	night
7	100	100	9.4	-3.4	-0.0050	0.0	

Each case is numbered and has been run for one or three horizontal resolutions indicated by $\Delta x, \Delta y$. The number of vertical grid points is listed as NZ. The geostrophic wind is given as u_g and v_g (along Easting and Northing respectively). The vertical temperature gradient in the lower part of the atmosphere is listed as $\frac{\Delta T}{\Delta z}$. ΔT_{land} is defined as the difference between the air temperature at 2 m height and the surface skin temperature over land, i.e.

$$\Delta T_{land} = T_{air,2m} - T_{land} \tag{145}$$

For all the shown cases the orography filtered at 50 m horizontal resolution was utilized except for case 4 for which the orography was filtered at 25 m resolution using a binomial filter kernel with 17 points, i.e. $n = 17$ in Equation (141).

4.3 Results

4.3.1 Initial results

While testing grid independence in for case 1, it was attempted to investigate the effects of the temperature conditions of day in case 2. No grid independence was found for case 1, rendering both case 1 and case 2 invalid. However, it was noticed from the data of case 1 that the surface wind should be turned clockwise by 15° in order to match the 310° at

50 *m* (agl.) predominant at Mast 1. From the data of case 2 it was seen that the surface wind should be 50% larger for day conditions. This can be explained by the increased influence of the surface in the lower part of the boundary layer for the day situation which has more convection.

It was then decided to increase the vertical resolution of the model by using 100 vertical grid points in case 3. In order to be able to compare to case 1, the other parameters in Table 5 were set as in case 1. The resulting wind speed at 50 *m* (agl.) after four hours of simulation time is shown in Figure 41. The horizontal wind speed at 50 *m* (agl.) along

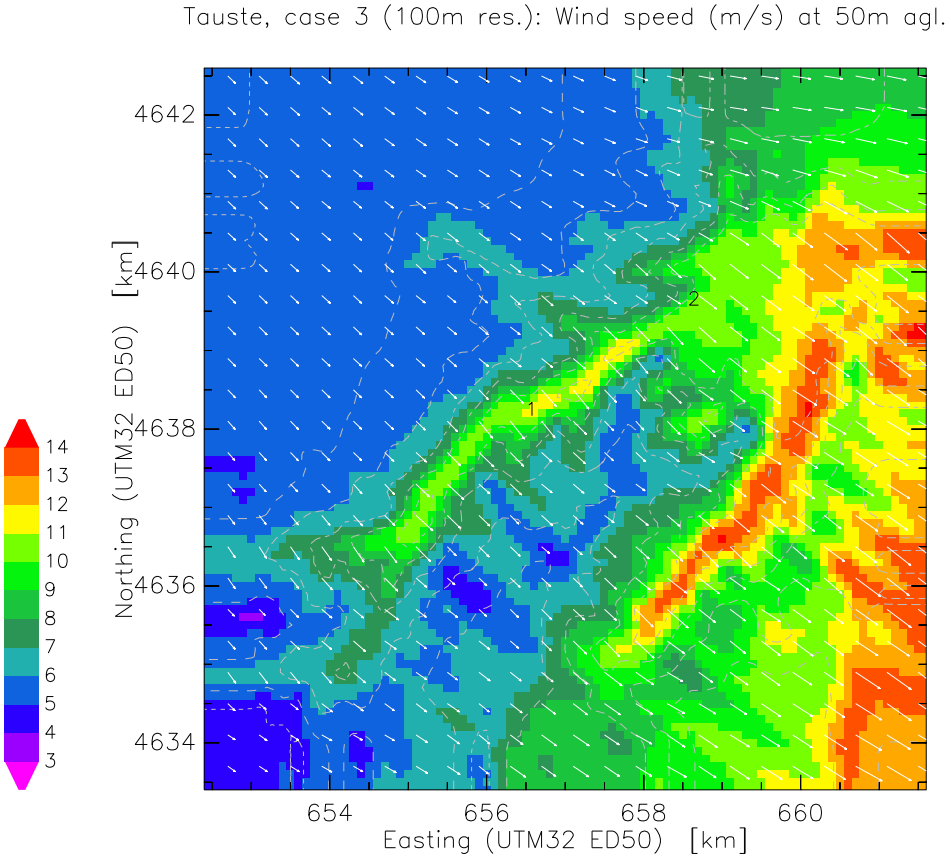

Figure 41. The horizontal wind speed for case 3 at 50 *m (agl.) for Tauste.*

the transects 1 and 2 indicated in Figure 40 is shown in Figure 42 for KAMM2 at three different horizontal resolutions and for WAsP Engineering. The results for transect 3 are shown in Figure 43. It is seen from Figure 41 that the first peak at the position of 5.7 *km* in transect 1 in Figure 42 is the most important part, as it is near the position of the meteorological mast 1. For transect 2 in Figure 42 the most important part is the peak at the position of 4 *km* which is near the mast 2. In Figure 43 it is hard to see the positions of the masts in the plot. Mast 1 is located at 4.9 *km* and Mast 2 is located at 7.6 *km*. Grid independence is not clear at the positions near the masts. However, the results for the three different horizontal resolutions are generally close in large parts of the domain investigated via the transects. It is readily seen in the figure that the level of the wind speed near mast 1 is very similar for KAMM2 and WAsP Engineering, whereas the wind speed for WAsP Engineering is generally greater than for KAMM2 along the part of each transect before the masts and generally smaller than for KAMM2 along the part after.

The wind direction at 50 *m* (agl.) along the transects 1 and 2 is shown in Figure 44 for

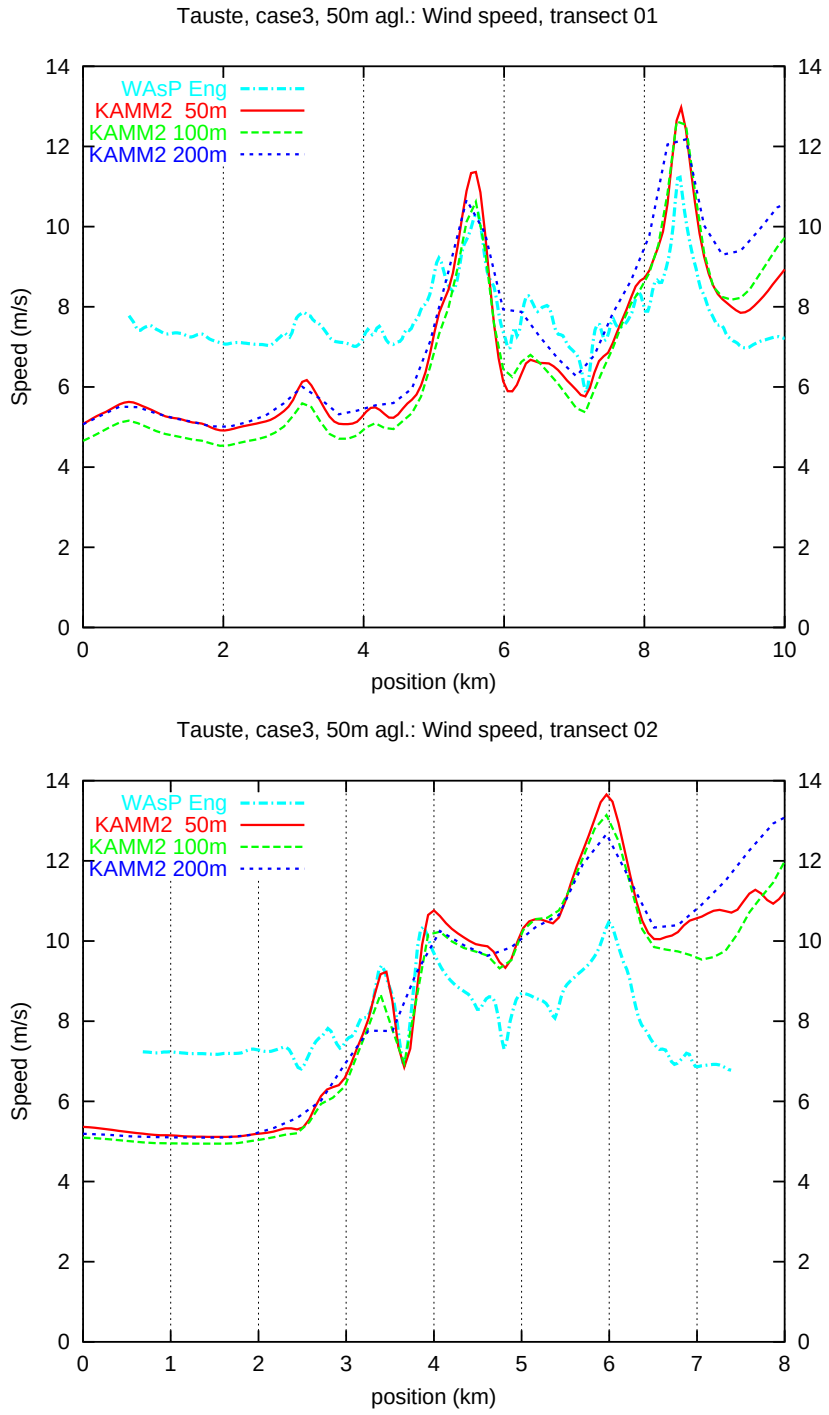

Figure 42. The horizontal wind speed for case 3 at 50 *m (agl.) along the transects 1 (top) and 2 (bottom).*

KAMM2 at three different resolutions and for WAsP Engineering. The results for transect 3 are shown in Figure 45. Grid independence is obtained along all three transects for the wind direction. It is also seen that the results from WAsP Engineering are close to the wind directions from KAMM2. The vertical profiles of velocity are shown in Figures 46 and 47 for Mast 1 and 2, respectively. No indication of negative shear is visible for Mast 1. For Mast 2, a tendency of negative shear is observed in the lowest part of the plot of

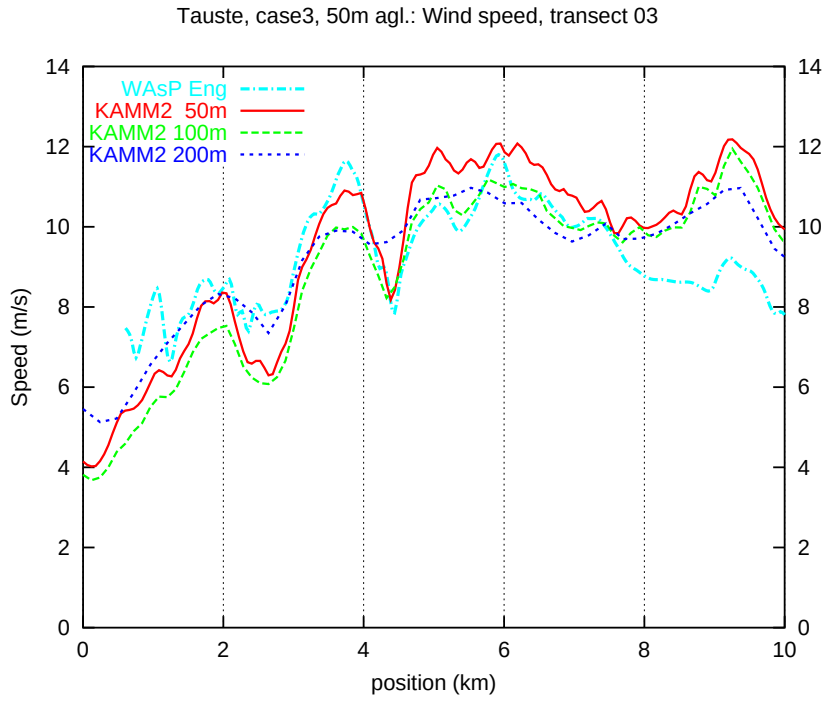

Figure 43. The horizontal wind speed for case 3 at 50 *m (agl.) along transect 3.*

v_h. However, it corresponds only to two grid cells and should be verified by simulations with higher vertical resolution near the ground.

The data for the comparison has been treated in the following way. First, all 10 minutes averages with a mean wind speed of more than 9 m/s at 42 m and a direction (at 42 m at mast 1 and at 50 m at mast 2) within $\pm 6°$ of the direction of the KAMM2 run at computational level number 6 ($z = 44.91$ m) are selected. Then, the wind speed at $z = 42$ m is scaled, so it matches the KAMM2 wind speed. The scale factor is used to scale wind speeds in all others heights and the wind direction is not changed. The resulting data set is averaged to get a profile which is guaranteed to match at $z = 44.91 \approx 42$ m, and we can make a crude test of the performance of the calculation by comparing calculations and the averaged wind speed and direction at the other heights. The vertical velocity generally compares very poorly with data. One explanation could be that the filtering changes the local slope of the terrain, which to a large degree determines w. The slightly negative wind shear observed at mast 2 (see figure 47 where the largest average speed is at $z \approx 18$ m) is not reproduced by the model. The large positive shear at mast 1 (figure 46) is also poorly reproduced.

In order to obtain a clear demonstration of grid independence, case 4 was run using a map filtered at 25 *m* instead of 50 *m* horizontal resolution. The underlying hypothesis is that grid independence is lost when the orography is filtered at a horizontal resolution similar or equal to the resolution utilized in the model runs. Thus, it was believed that doubling the resolution before the filtering of the orography should improve grid independence. However, this turned out not to be the case. In fact it made the situation worse! Rather, it is thought that the vertical resolution is more important, because an improvement in grid independence is actually achieved when going from case 1 to case 3.

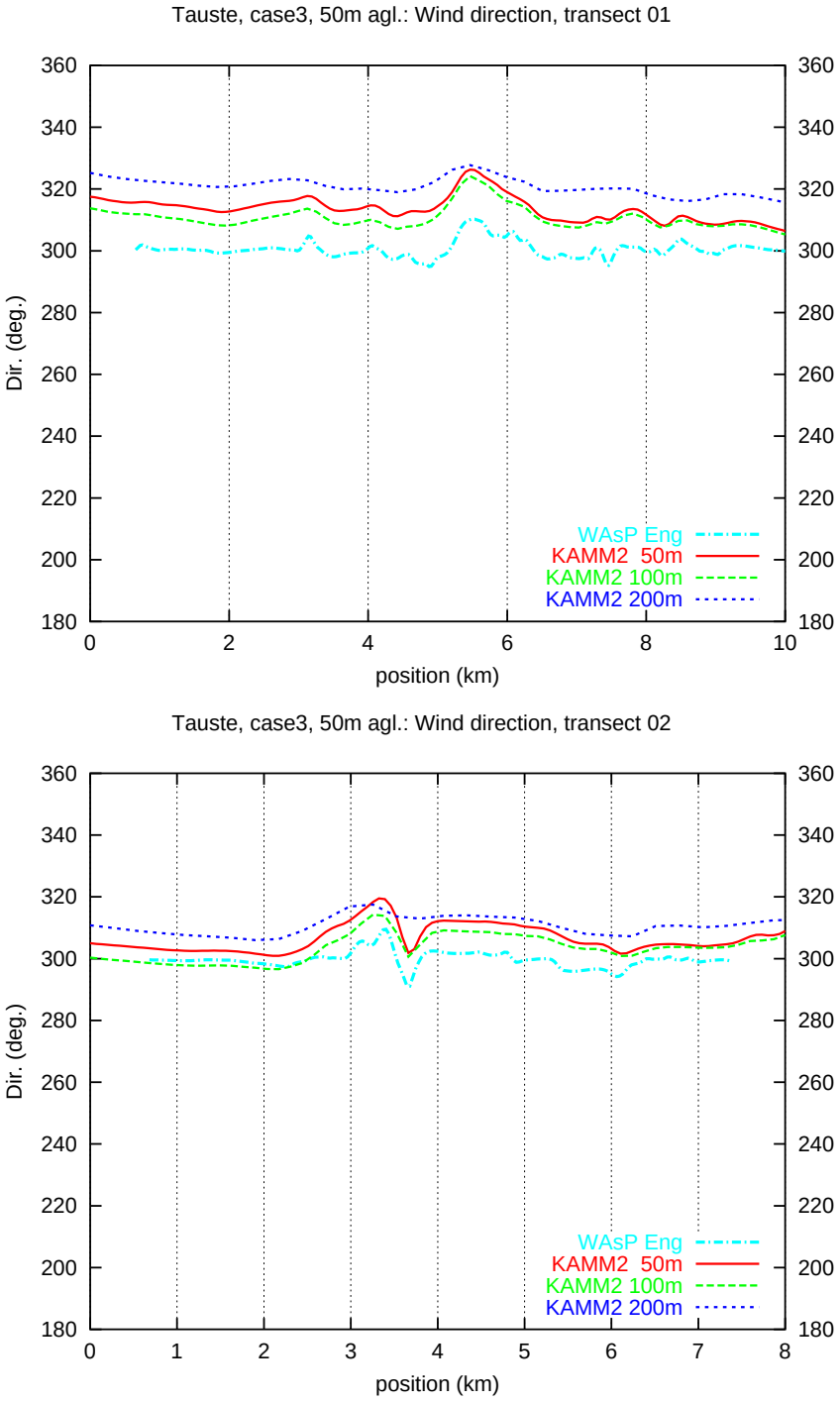

Figure 44. The wind direction for case 3 at 50 *m (agl.) along the transects 1 (top) and 2 (bottom).*

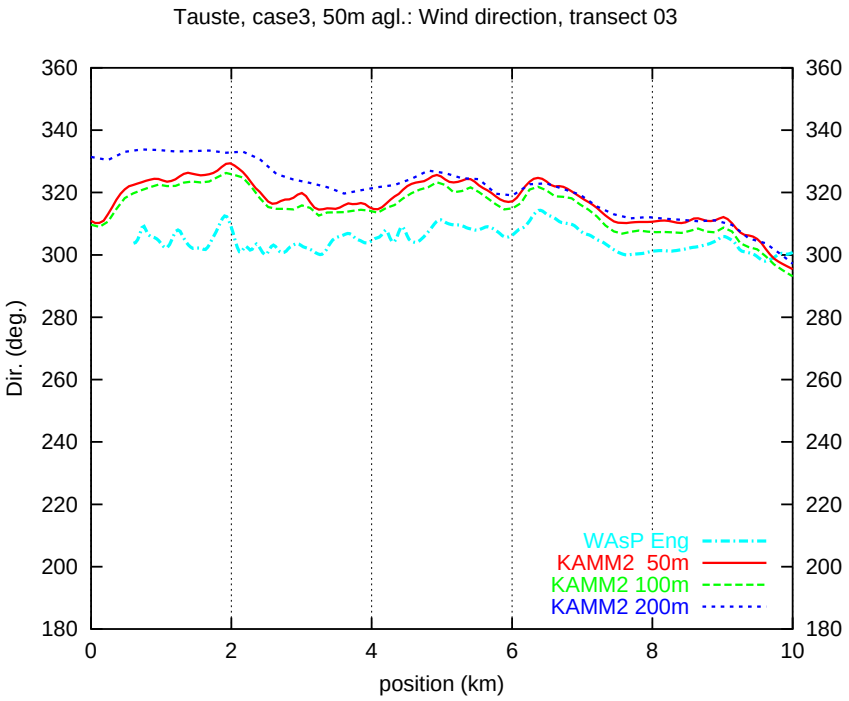

Figure 45. The wind direction for case 3 at 50 *m (agl.) along transect 3.*

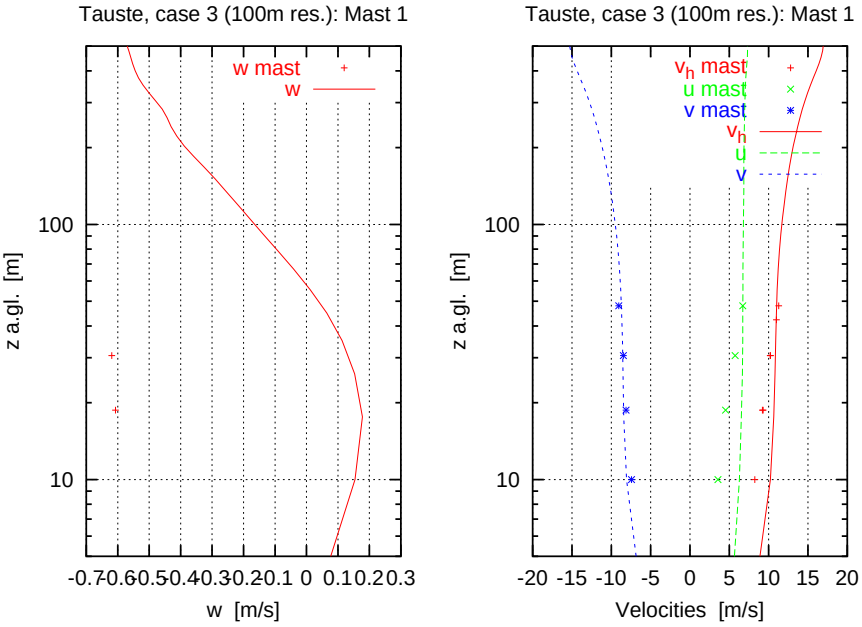

Figure 46. Vertical velocity profiles near Mast 1 for case 3. Left, vertical velocity. Right, horizontal wind speed (v_h) and its components u, v. Symbols are measurements.

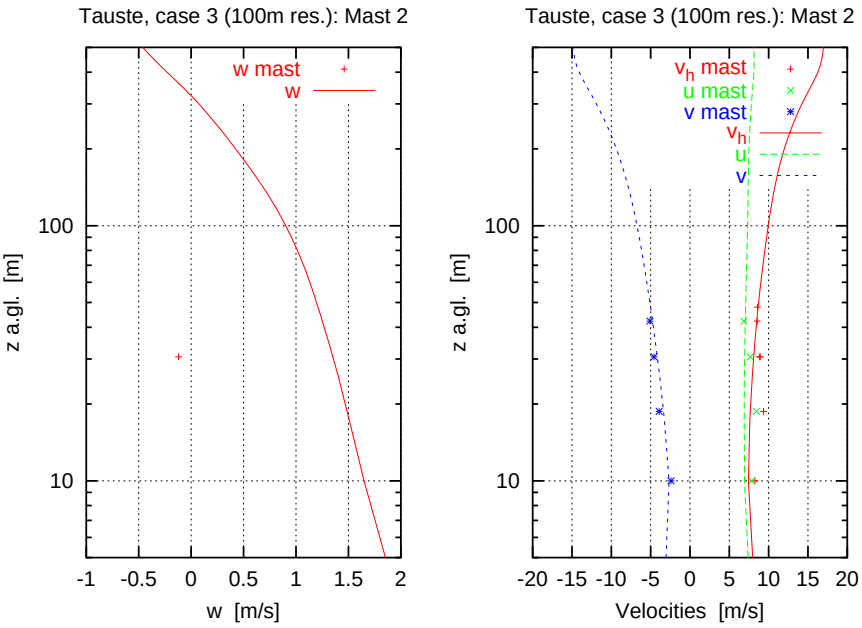

Figure 47. Vertical velocity profiles near Mast 2 for case 3. Left, vertical velocity. Right, horizontal wind speed (v_h) and its components u, v. Symbols are measurements.

4.3.2 Results of physical parameter changes

Based on the results from the cases 1,2,3 and 4 it was decided to continue an investigation of physical parameter changes with the same model setup as in case 3, assuming grid independence. Hence, a horizontal resolution of 100 m and a vertical resolution determined by $NZ = 100$ was applied to the cases 5, 6 and 7.

The geostrophic wind direction of case 5, 6 and 7 was set to 290° corresponding to a clockwise rotation of 20° relative to the cases 1 and 3. The purpose of this is to obtain a surface wind direction close to 310°. However, this was not achieved in the model results. The modelled wind speed and direction for Mast 1 at 50 m height (agl.) is summarized together with the geostrophic wind speed and direction in Table 6. The horizontal grid resolution referred to is 100 m. For convenience, the vertical temperature gradient and the difference between air temperature at height 2 m and the surface skin temperature are also shown.

Table 6. Summary of speed and direction for the geostrophic wind and the modelled wind near Mast 1 at 50 *m (agl.) height. The horizontal resolution, the vertical temperature gradient and the temperature difference between air and surface are also shown.*

case	$\Delta x, \Delta y\ (m)$	$FF_g\ \left(\frac{m}{s}\right)$	$DD_g\ (°)$	$FF\ \left(\frac{m}{s}\right)$	$DD\ (°)$	$\frac{\Delta T}{\Delta z}\ \left(\frac{K}{m}\right)$	$\Delta T_{land}\ (K)$
1	100	10.0	311	9.1	325	-0.0065	0.0
2	100	10.0	307	6.4	299	-0.0098	-3.0
3	100	10.0	311	9.4	321	-0.0065	0.0
4	100	10.0				-0.0065	0.0
5	100	15.0	290	9.5	231	-0.0098	-3.0
6	100	10.0	290	13.6	344	-0.0050	3.0
7	100	10.0	290	13.6	340	-0.0050	0.0

In case 5 the geostrophic wind was increased by 50% relative to case 2. Case 5 was allowed six hours of simulation time whereas the cases 1, 2, 3, 4, 6 and 7 were only allowed four hours of simulation time. The purpose of case 5 was to simulate day time temperature conditions similar to case 2. But the geostrophic wind in case 5 was adjusted to yield a sufficiently high surface wind (the wind speed at 50 m height (agl.) should be $10 - 14\ m/s$). However, the direction of the geostrophic wind was chosen wrong by a mistake. It should have been increased by 10° instead of decreased by 20°. The resulting wind speed at 50 m (agl.) is shown in Figure 48. The horizontal wind speed at 50 m (agl.) along the transects 1 and 2 is shown in Figure 49 for KAMM2 and for WAsP Engineering. For transect 1 the wind speed of KAMM2 is close to the wind speed of WAsP Engineering at the position 5.7 km corresponding to Mast 1. For the rest of the plot the wind speed of KAMM2 is significantly higher than that of WAsP Engineering. A similiar behavior is observed for transect 2. Here, Mast 2 is located at the position 4 km. The wind direction at 50 m (agl.) along the transect 1 is shown in Figure 50 for KAMM2 and for WAsP Engineering. Unfortunately, the wind direction of KAMM2 is offset by 80° clockwise relative to the predominant wind direction of Mast 1 as indicated in Table 6. This is of course visible in the large difference between KAMM2 and WAsP Engineering. The vertical profiles of velocity are shown in Figures 51 and 47 for Mast 1 and 2, respectively. No indication of negative shear is visible for any of the masts. On the contrary, the observations at mast 1 show strong positive shear. The model also have quite strong shear, although the detailed shape of the profile is not reproduced.

The purpose of case 6 is to investigate the effect of night time temperature conditions. Thus, the air temperature gradient in this case corresponds to stable conditions and $\Delta T_{land} = T_{air} - T_{land}$ was set to 3.0 K simulating a cold surface. The resulting wind speed at 50 m (agl.) is shown in Figure 53. The horizontal wind speed at 50 m (agl.) along

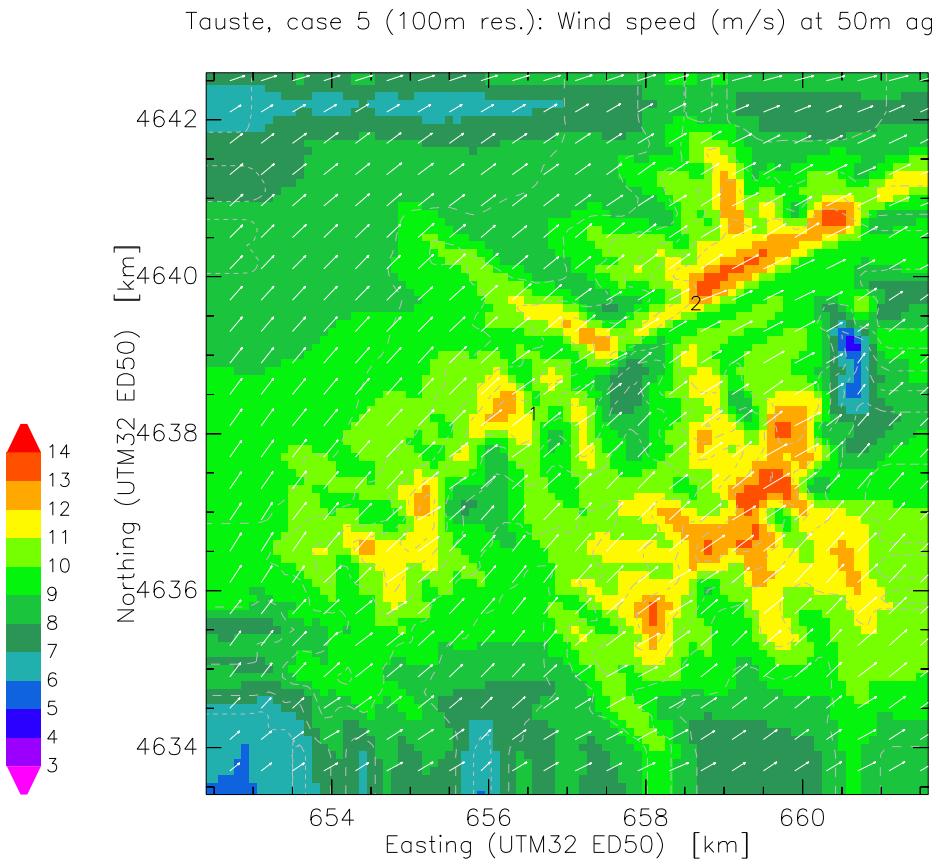

Figure 48. The horizontal wind speed for case 5 at 50 *m (agl.) for Tauste.*

the transects 1 and 2 is shown in Figure 54 for KAMM2 and for WAsP Engineering. The wind speed of KAMM2 along transect 1 is close to the wind speed of WAsP Engineering for positions lower than 5 km. Near Mast 1 at the position 5.7 km the difference in wind speed is large. For positions greater than 5 km the wind speed of KAMM2 is significantly larger than the wind speeds of WAsP Engineering. In contrast, the wind speed of KAMM2 along transect 2 is lower than the wind speed of WAsP Engineering for positions less than 3 km and larger for positions greater than 4 km. For positions from 3 km and up to the location of Mast 2 at 4 km the velocities of the two models are close. The wind direction at 50 m (agl.) along the transect 1 is shown in Figure 55 for KAMM2 and for WAsP Engineering. The wind direction og KAMM2 is offset by 30° counter-clockwise relative to the predominant wind direction of Mast 1 as indicated in Table 6. This is observed in the difference between KAMM2 and WAsP Engineering. The vertical profiles of velocity are shown in Figures 56 and 57 for Mast 1 and 2, respectively. No indication of negative shear is visible for Mast 1, but the quite flat profile compares well with data. For Mast 2, a tendency of negative shear is observed is observed in the lowest part of the plot of v_h. However, like for case 3, it corresponds only to two grid cells and should be verified by simulations with higher vertical resolution near the ground. Also, the observed slightly negative shear at higher elevations seems not to be reproduced by the model. Whether this discrepancy is due to the model or wrong input to the model remains to be seen.

There is not much difference between case 6 and case 7, which have identical temperature gradients. Case 7 has $\Delta T_{land} = 0$. Apparently the change from the positive ΔT_{land} in case 6 to zero in case 7 does not have much effect for the temperature gradient of $-0.005\ K/m$.

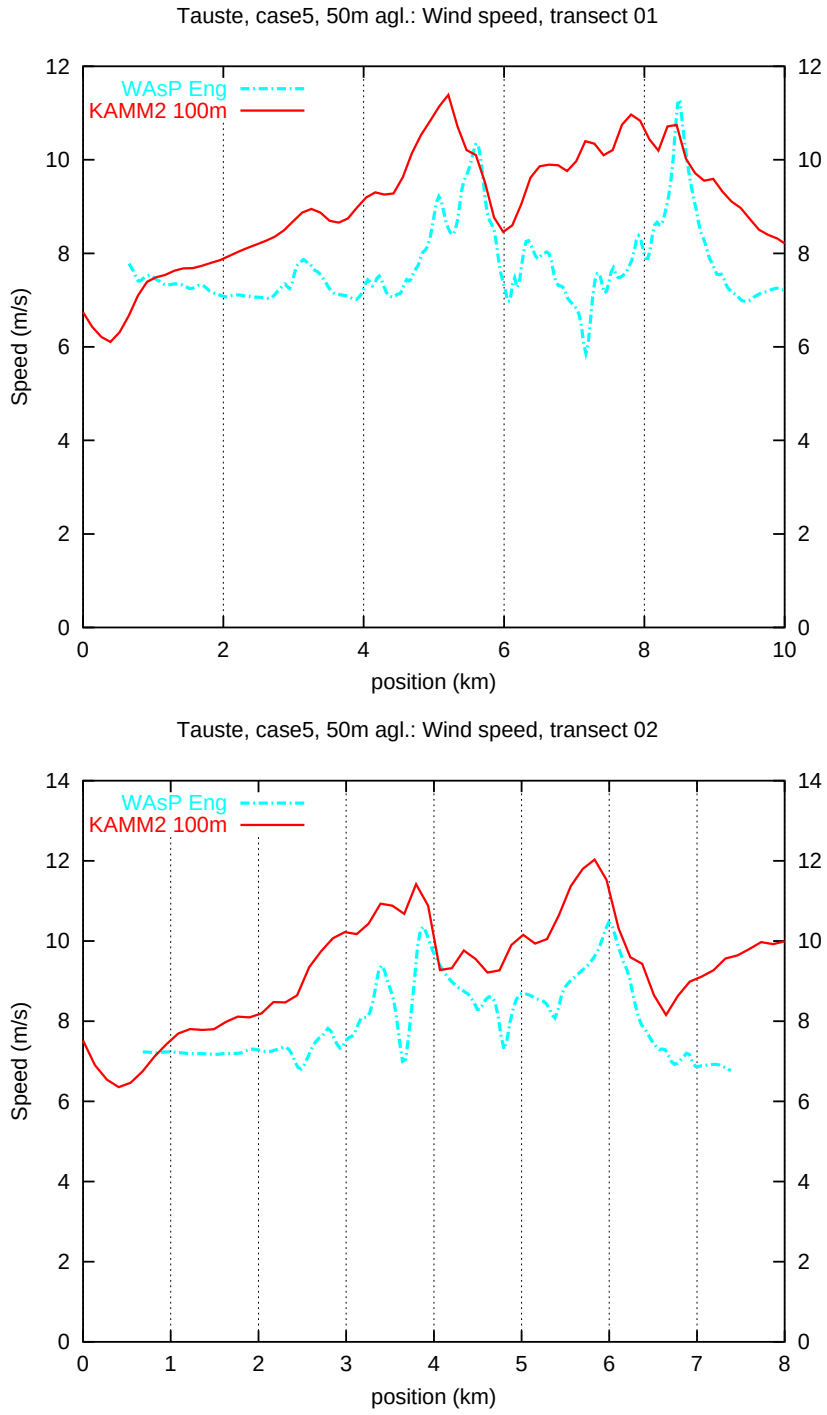

Figure 49. The horizontal wind speed for case 5 at 50 *m (agl.) along the transects 1 (top) and 2 (bottom).*

4.4 Conclusion

A number of different cases have been simulated with the Karlsruhe Atmospheric Mesoscale Model 2 (KAMM2) for a local area in Tauste, Spain. The motivation of the simulations is the presence of negative wind shear measured at heights under 50 *m* above ground level at two meteorological masts. It has been attempted to reproduce similar situations of negative shear by performing changes of the conditions of large scale forcing used as input to

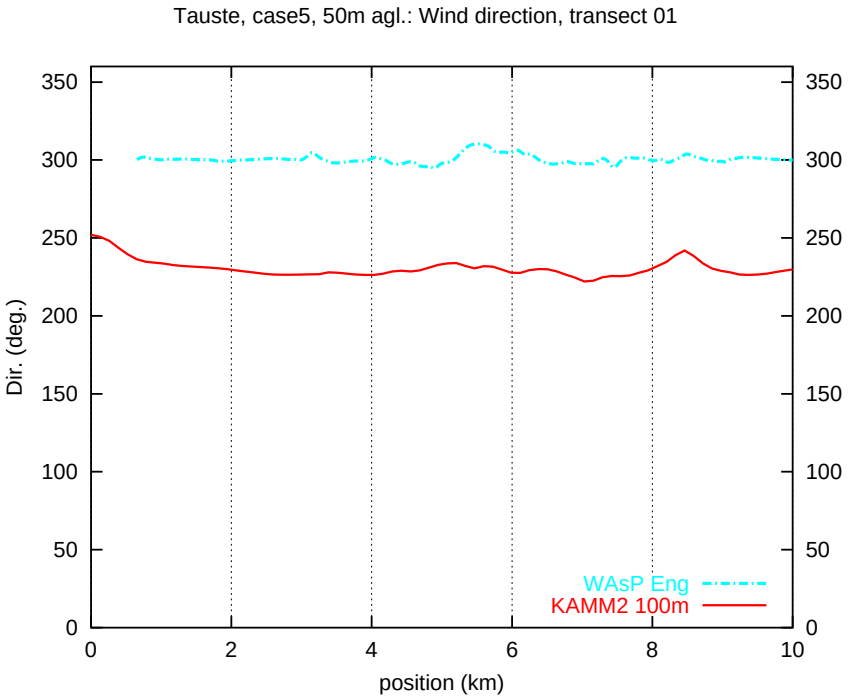

Figure 50. The wind direction for case 5 at 50 *m (agl.) along transect 1.*

the mesoscale model. In conclusion, no clear indication has been found of the ability of KAMM2 to produce negative wind shear similar to the measurements for the investigated conditions of large scale forcing. Two obstacles for the successful use of KAMM2 have been identified. First, the model seems not to handle non-smooth orography very well and extensive filtering of the terrain was necessary. Second, for the type of calculations considered here, the demand for computational resources is very large, making detailed parameter studies impractical.

The following conditions have been tried. First, a stable but near neutral case. Second, a day case with neutral atmosphere and a warm surface. Third, a night case with stable atmosphere and cold surface. Fourth, a case with stable atmosphere and a surface with temperature similar to the air.

It is also concluded that more effort in the direction of testing different conditions of large scale forcing and perhaps different turbulence model schemes is somewhat lacking in the present study. However, it was found necessary to spend a large part of the work in establishing the validity of the results generated by the mesoscale model.

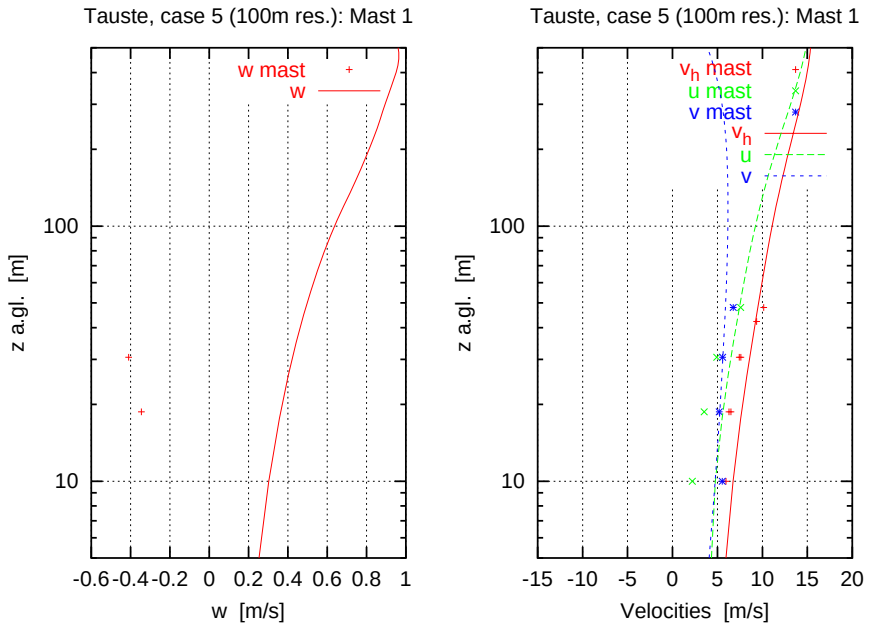

Figure 51. Vertical velocity profiles near Mast 1 for case 5. Left, vertical velocity. Right, horizontal wind speed (v_h) and its components u, v. Symbols are measurements.

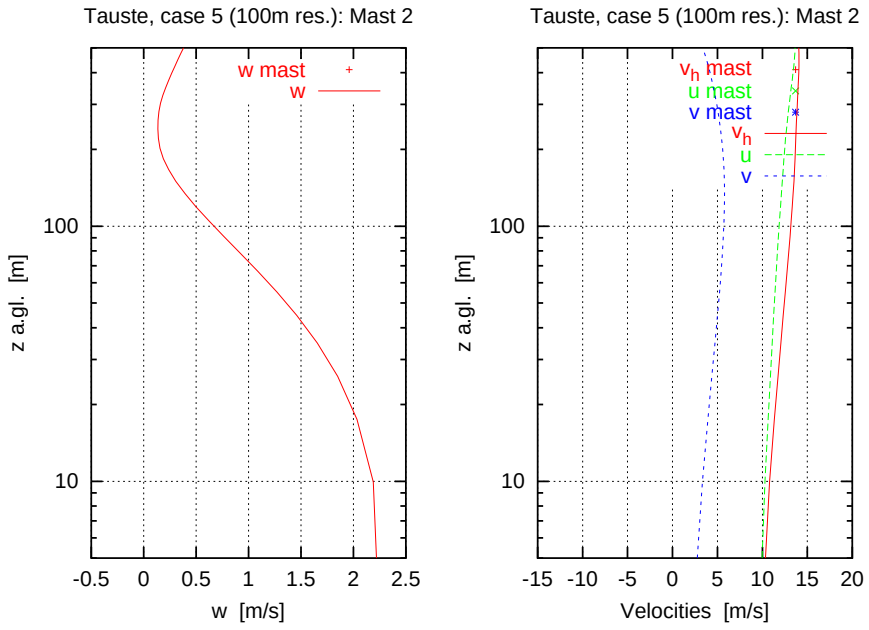

Figure 52. Vertical velocity profiles near Mast 2 for case 5. Left, vertical velocity. Right, horizontal wind speed (v_h) and its components u, v. No measurements were available for this particular direction.

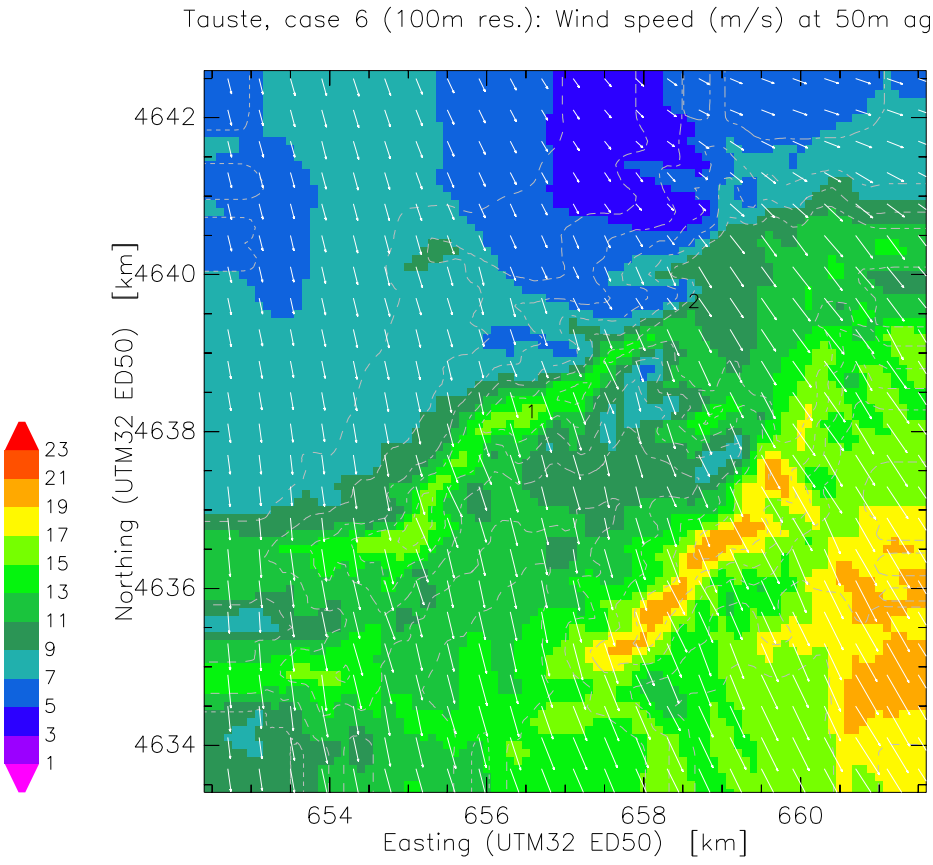

Figure 53. The horizontal wind speed for case 6 at 50 *m (agl.) for Tauste.*

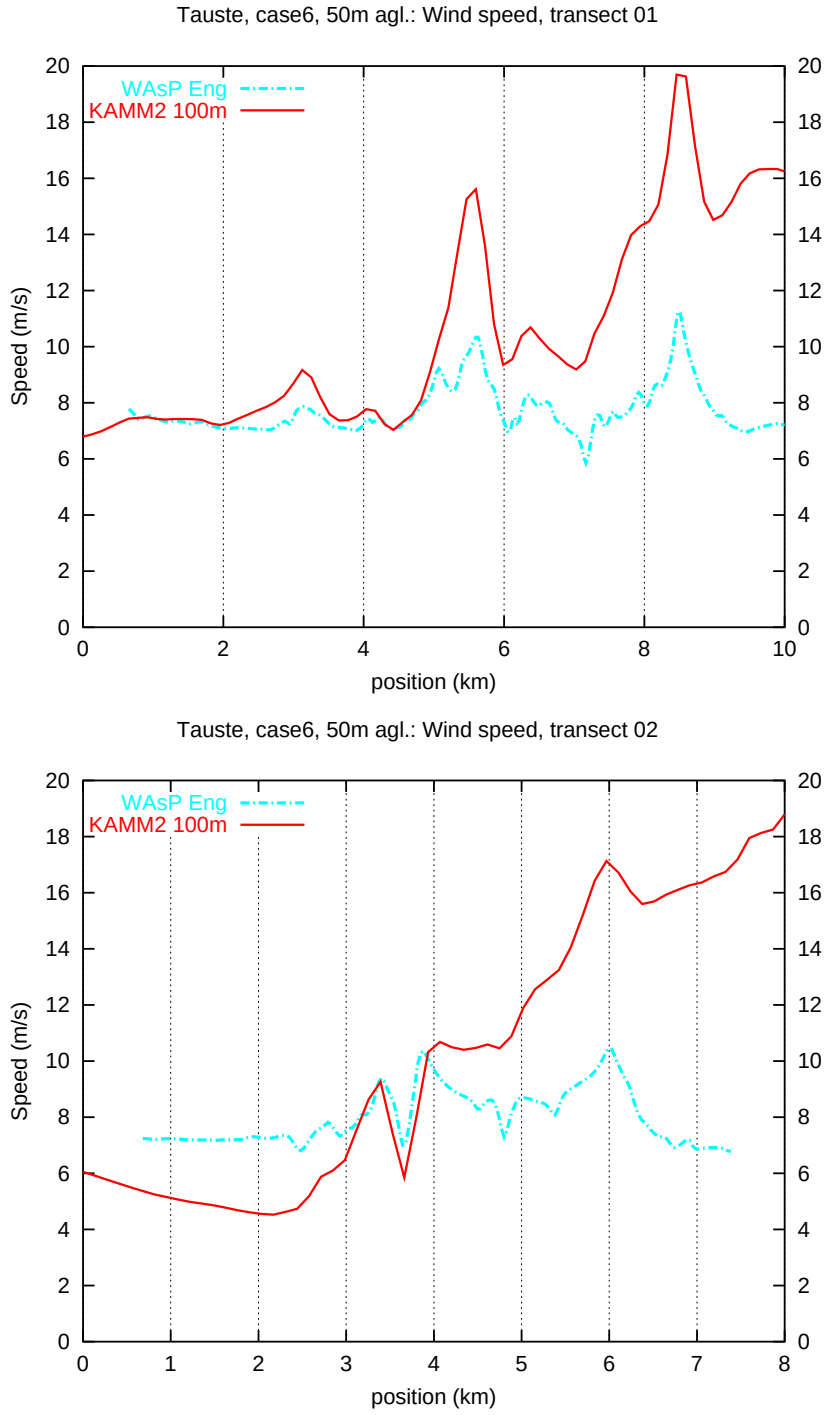

Figure 54. The horizontal wind speed for case 6 at 50 *m (agl.) along the transects 1 (top) and 2 (bottom).*

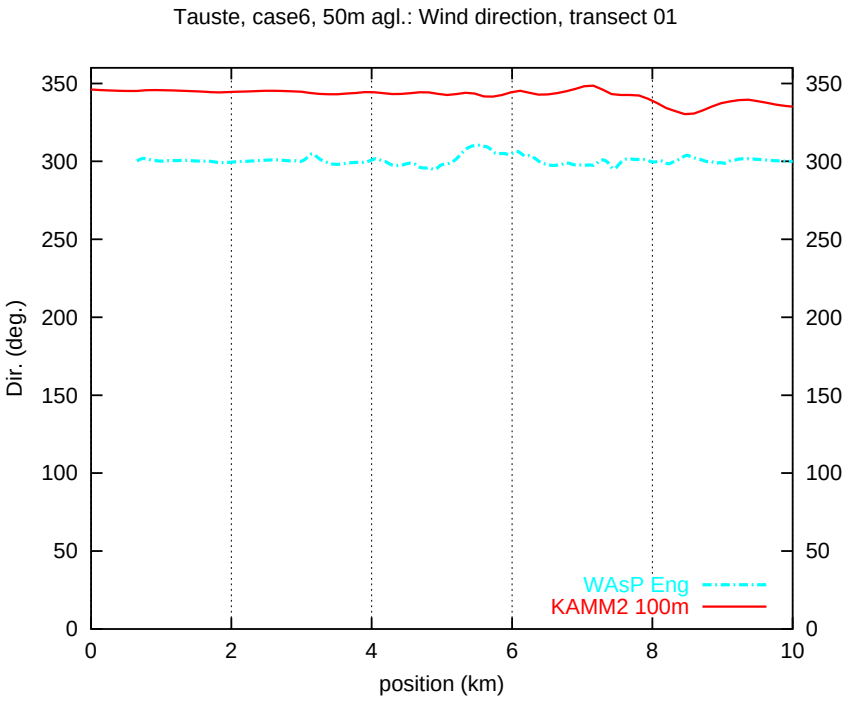

Figure 55. The wind direction for case 6 at 50 *m (agl.) along transect 1.*

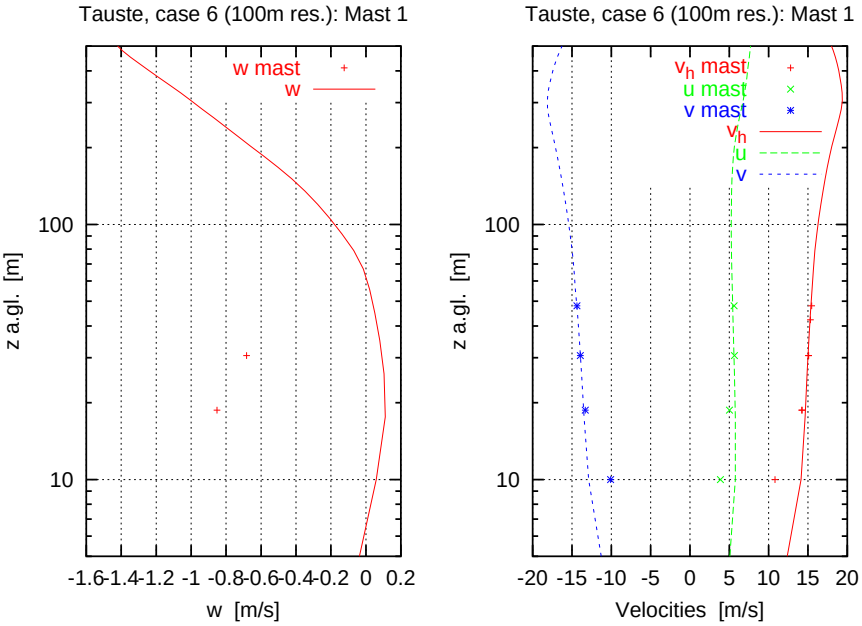

Figure 56. Vertical velocity profiles near Mast 1 for case 6. Left, vertical velocity. Right, horizontal wind speed (v_h) and its components u, v. Symbols are measurements.

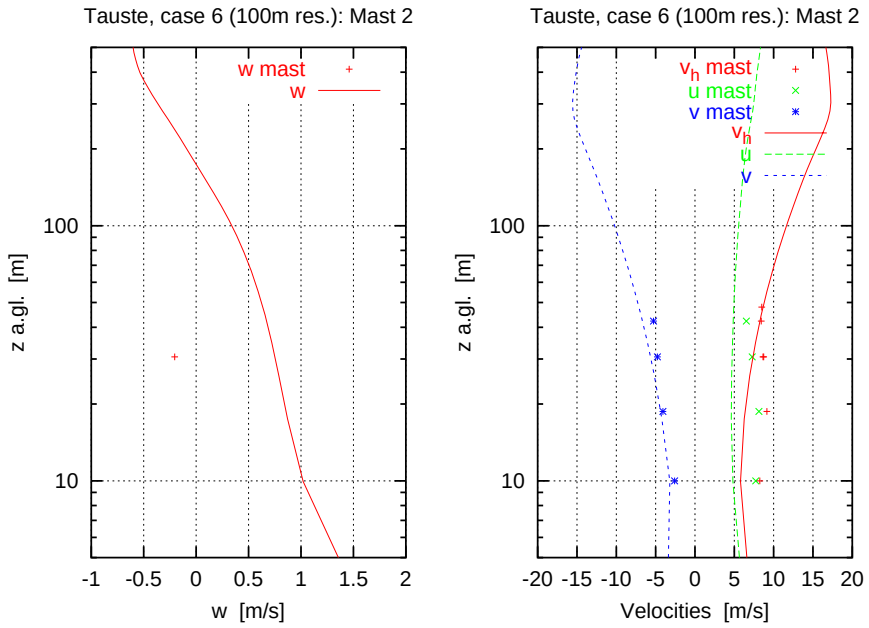

Figure 57. Vertical velocity profiles near Mast 2 for case 6. Left, vertical velocity. Right, horizontal wind speed (v_h) and its components u, v. Symbols are measurements.

5 Extreme winds

5.1 50 year winds from Reanalysis Data

For the analysis of extreme winds it is necessary to have several years of observations to be able to make a reliable estimate of the wind speed, which can be expected to occur with a return period of 50 years. For many constructions, this wind produces the extreme load for which the building must be designed. Jensen and Franck (1970), Abild (1994) and Kristensen, Rathmann and Hansen (1999) determined the 50 year return wind for Denmark from measurements at different sites. However, in many locations good measurements over a sufficient observation period are not available. Hence, it would be of great advantage if extreme surface winds could be derived from modeled data.

An analysis of global weather observations with a modern numerical weather analysis and modeling system was and is performed by the U.S. National Centers for Environmental Prediction (NCEP) and the National Center for Atmospheric Research (NCAR) (Kalnay, Kanamitsu, Kistler, Collins, Deaven, Gandin, Iredell, Saha, White, Woollen, Zhu, Leetmaa, Reynolds, Chelliah, Ebisuzaki, Higgins, Janowiak, Mo, Ropelewski, Wang, Jenne and Joseph 1996). The NCEP/NCAR reanalysis covers more than 50 years world wide. Therefore, it promises a good data base for global estimates of the extreme winds. However, the low resolution of the global reanalysis model and the temporal resolution of 6 hours will likely result in an under-estimation of the actual extreme winds. However, if this under-estimation turns out to be systematic, the extreme winds from the model could be corrected to make global predictions of the expected extreme surface wind.

Here we describe an analysis done for an area around Denmark. More details can be found in Frank (2001).

5.1.1 The reanalysis data

First, we analyzed the predicted wind at 10 m above the surface. It is calculated on a Gaussian grid with a longitudinal resolution of 1.875° and meridional resolution of approximately 1.91° (Kalnay et al. 1996). The surface wind is a quantity which strongly depends on the model physics. The data analyzed here is a 6-h forecast, not an analysis of observations. Still, as we are not interested in the prediction of the highest winds in individual storms, but only in the statistics of extreme winds, the model winds might yield good estimates of the true extreme winds.

We used wind data every 6 hours for the 52 years 1948 to 1999. The maximum modeled 10 m wind speed for the years 1948 to 1999 is shown in Figure 58. Actually, the 10 m wind of the model is calculated at the height $10\,\mathrm{m} + z_0$, which can be 11 m or more at grid points over land.

The date of the maximum wind is also written on Figure 58. At several longitudes the most severe storm occurs on the same day. However, only at two grid points does the highest wind occur at neighboring latitudes. This indicates the main storm passages from west to east. Most likely, the true maximum speed occurred between the 6 hour sampling interval. As the storm moves eastward its intensity decreases. This can be seen best at latitude 52.4° N.

It is striking that the great storm on December 3. 1999 (Mann and Hansen 2000) seems to be missed partly by the reanalysis data. Only at the two grid points in the Baltic has 50 year maxima at Dec. 3. 1999 despite the fact that the strongest wind ever measured in Denmark was on this occasion 15 km off the coast of Jutland in the North Sea. Here, at a location called Horns Rev, the 10 minute average wind speed peaked at 39.3 m/s at 15 m above the water. (It was 45.4 m/s at $z = 62$ m.) A five hour average wind speed centered around this extreme is 31.5 m/s, much higher that the North Sea maxima from the reanalysis data of approximately 25 m/s. It seems that the spatial resolution of the

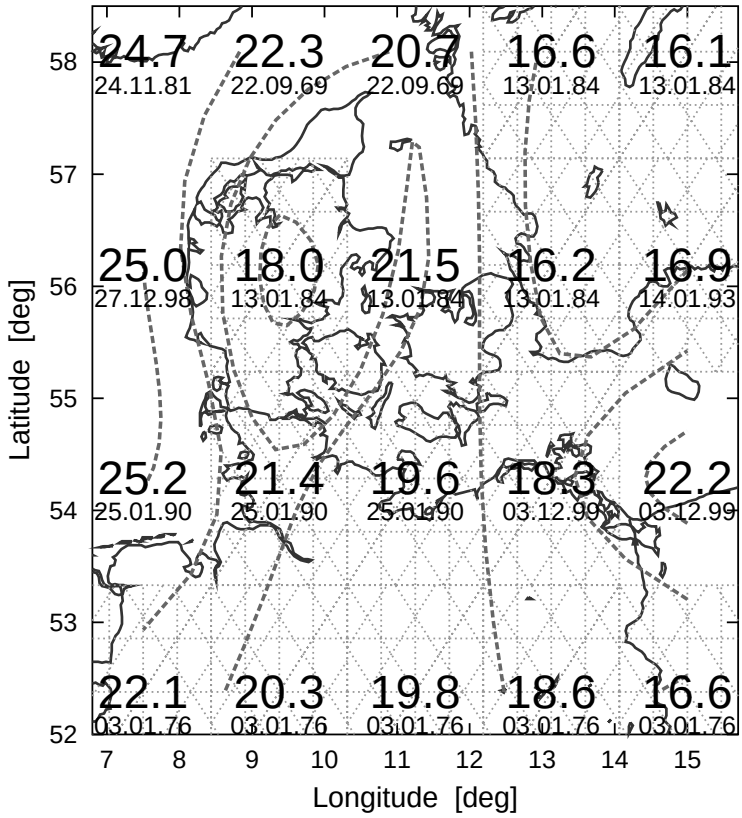

Figure 58. Maximum wind at 10 m for the years 1948 to 1999 of the NCEP/NCAR reanalysis and date of the maximum wind. Grid points over land are hatched. Grid points over water are white.

model is not sufficient to resolve this storm.

The wind at 850 hPa is available on a regular grid with a resolution of 2.5 degrees in longitudinal and meridional direction. It has been interpolated to the pressure levels and the 2.5 degrees grid from the sigma levels of the model and the spectral representation of the model. The interpolation introduces some smoothing. Upper-air winds depend more on observations than on the model physics. This is especially the case in Europe with its dense network of observations. Hence, the data represents analyzed observations, not 6 hour forecasts as the surface wind.

Another data set is the surface pressure, i.e. the pressure at the model surface. Like the 10 m wind it is a 6 hour forecast. But, it is more influenced by observations. It is available on the same grid as the 10 m wind. A geostrophic wind near the surface can be calculated from it. The disadvantage is that the pressure must be extrapolated to one height to calculate gradients. Any interpolation introduces extra uncertainties.

5.1.2 The statistical model

The frequency of extreme events is described by the double exponential, the so-called Gumbel distribution (Gumbel 1958):

$$P(U) = \exp(-\exp(-\alpha(U-\beta))) \tag{146}$$

$P(U)$ is the cumulative probability that the wind speed, U, is exceeded.

We use the periodical maximum method of Abild (1994) as described by Mann, Kristensen and Jensen (1998) to determine the parameters α and β. The method is the probability-weighted moment procedure.

A record of the maximum winds $U_1^{\max}, \ldots, U_n^{\max}$ within a certain period is constructed and sorted in ascending order. Here, the maximum wind in one calendar year has been

chosen and ordered. From this record the quantity

$$b_1 = \frac{1}{n}\sum_{i=1}^{n}\frac{i-1}{n-1}U_i^{\max} \tag{147}$$

is calculated. Then α and β can be estimated to be

$$\alpha = \frac{\ln 2}{2b_1 - \overline{U^{\max}}} \tag{148}$$

$$\beta = \overline{U^{\max}} - \frac{\gamma}{\alpha} \quad , \tag{149}$$

where $\gamma \approx 0.577216$ is Euler's constant, and $\overline{U^{\max}}$ the mean maximum value.

From the cumulative probability (146) for the recurrence interval $T = 1/(1-P(U_T))$, the T-year wind speed U_T is obtained:

$$U_T = \alpha^{-1}\ln T + \beta \tag{150}$$

The uncertainty of U_T can also be calculated (Mann et al. 1998).

5.1.3 Extreme surface winds from the NCEP/NCAR reanalysis

The one-year maximum winds were determined from the 52 years 1948-1999. The parameters α and β of the double exponential function were fitted to the record of ranked annual maximum wind for each grid point near Denmark. The records are well approximated by this function. (see e.g. Figure 59).

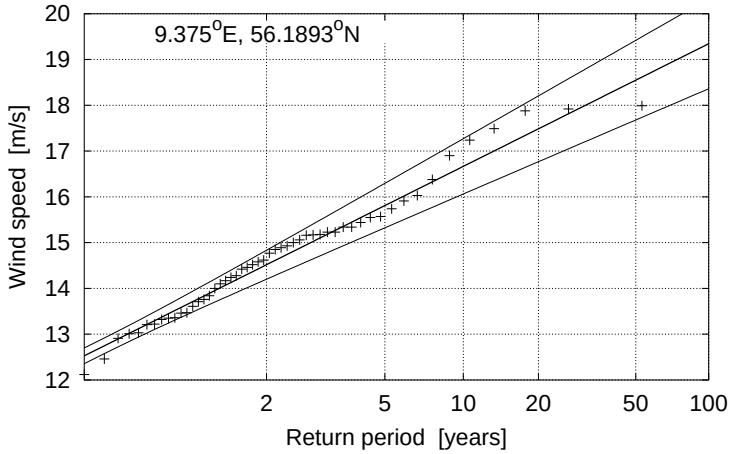

Figure 59. Ordered one-year maximum wind speed at 10 m at 9.375° *E,* 56.19° *N, and the double exponential fit. The thin lines are the fit plus/minus one standard deviation.*

A map of the expected 50 year return wind speed is shown in Figure 60. The values range from 15.4 m s^{-1} in Sweden to 26.6 m s^{-1} in the North Sea west of Denmark. The standard deviations are between 0.6 m s^{-1} and 1.3 m s^{-1}. Naturally, the winds are higher over the sea than over land. In addition, there is a decrease from west to east.

Abild (1994) obtained 28.8 m s^{-1} for the expected maximum wind at 10 m above water averaged over 10 min with a return period of 50 years. He transformed the estimate of Jensen and Franck (1970) for Thorsminde at the west coast of Jutland to 30.3 m s^{-1} for conditions over water. The grid point in the North Sea west of Denmark has a maximum of 26.6 m s^{-1}. However, this data is sampled only 4 times daily. Likely, the true maxima occurred in between the sampling times.

This effect was tested for time series of 10 min mean wind measurements at 44 m, 77 m, and 125 m height at the Risø mast. The original time series were continuous and covered 4 years. The data recovery rate is greater than 99 %. The maximum speeds within

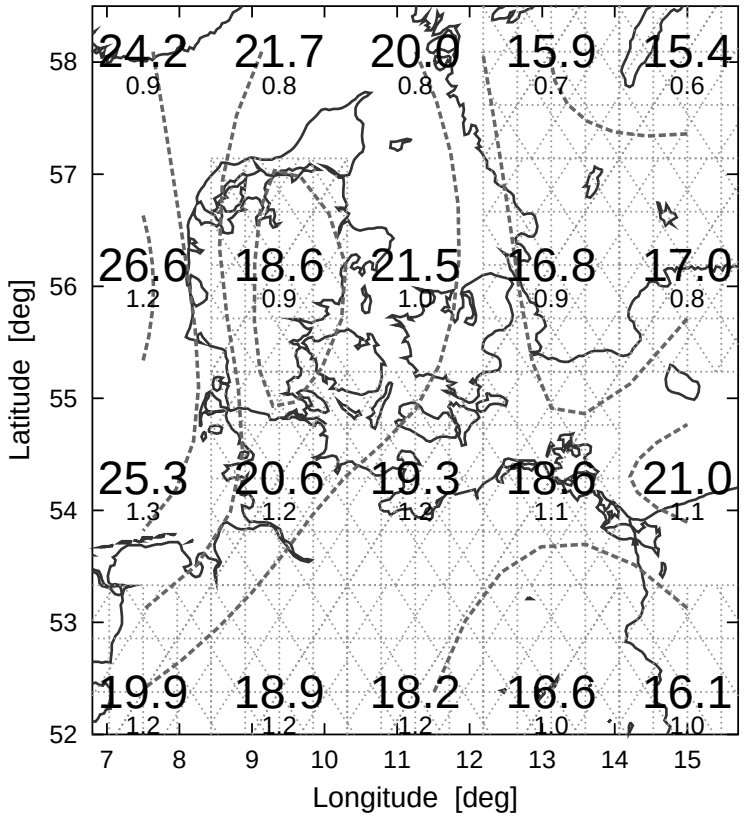

Figure 60. The expected 50 year maximum 10 m wind determined from the NCEP/NCAR reanalysis over and near Denmark. The standard deviation is written below the expected value.

3 months were found and averaged. Taking only the data at the hours 0, 6, 12, 18 the average maximum is reduced to between 87.4 % and 88.9 % of the maximum of the full time series. The reduction is slightly less at 125 m than at 44 m height.

Definitively, the variability in the model is less than in nature. The time step of the model is 20 min. However, it is not clear that this truly corresponds to an averaging time of 20 min of measured data. Also spatial averaging may reduce the modeled maxima compared to point measurements. If we correct the model wind by 11 % we obtain 29.5 $\mathrm{m\,s^{-1}}$. This lies between the estimates of Abild (1994) and the transformed estimate of Jensen and Franck (1970). The uncertainty margin of our estimates includes both.

5.1.4 Surface winds at standard conditions

The extreme winds obtained in the previous section cannot be compared directly with each other and with observations because the surface roughness varies from one grid point over land to the other. It must be expected to differ from the local roughness at an observation site, too. Therefore, the modeled winds must be transformed to a common roughness to make them comparable among each other and to observations.

The transformation to one roughness follows the wind atlas method used in the European Wind Atlas (Troen and Petersen 1989) and applied to extreme winds by Abild (1994) and Kristensen et al. (1999).

The surface roughness used in the NCEP/NCAR reanalysis model is determined from the Simple Biosphere Model (Dorman and Sellers 1989). Daily values are interpolated from a data base of monthly values. In addition an interpolation is done from the original $1° \times 1°$ resolution of the data base to the grid of the reanalysis model. Unfortunately, neither the peninsula of Jutland nor the Danish islands are present in the original data

base. Instead, it indicates water for these areas. The interpolation program *cycle* yields a land roughness for the peninsula of Jutland (Figure 61) because the land-sea mask for the NCEP/NCAR model defines these points as land areas. However, values between 0.5 m and 1 m are too high for this region, which is dominated by farming without large forest areas.

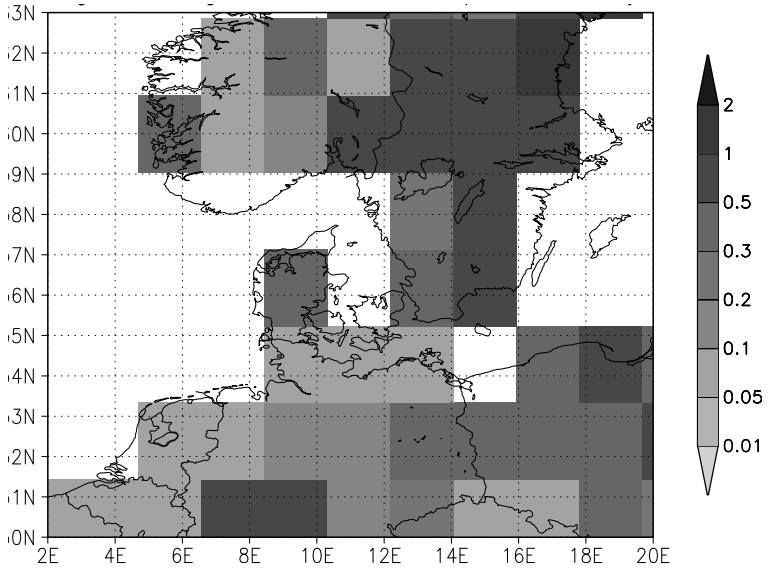

Figure 61. Surface roughness length z_0 in mid-January as used in the NCEP/NCAR reanalysis. These roughness lengths are derived from the data base for the Simple Biosphere Model (Dorman and Sellers 1989).

Over the sea the roughness length depends on the wind speed following Charnock (1955). The Charnock constant $A_c = 0.014$ is used in the model. Assuming a logarithmic wind profile the sea surface roughness can be iterated from the 10 m wind speed. Alternatively, it can be down-loaded from the Climatic Diagnostics Center, CDC. However, the down-loaded sea surface roughness values are greater than those iterated from the 10 m wind speed. Even after communication with Hua-Lu Pan from NCEP it was not possible to find out the reason for the difference.

In the end it was not clear how to transform the modeled surface wind to standard conditions with smooth transitions from sea to land and reverse. Stratification has only a very minor influence on the surface winds under conditions of extreme winds. During storms the surface layer is well mixed. This was confirmed by calculations where a Monin-Obukhov-length was determined from the wind speed at 10 m and the difference of the 2 m temperature and the skin temperature of the model. The difference on the 50 year return wind was 0.1 m s^{-1} or less.

5.1.5 Extremes of winds at 850 hPa

The results of the last section was disappointing. The problem with the correct friction velocity over water could not be resolved. Therefore, an extreme wind analysis was done for the wind at the 850 hPa level, which is above the planetary boundary layer in Denmark. Therefore, it is not directly influenced by the surface roughness. The 50 year return wind at 850 hPa is shown in Figure 62. The extreme winds decrease from southwest to northeast.

The wind at 850 hPa is close to the geostrophic wind at 850 hPa. However, it must be expected that the geostrophic wind, i.e. the pressure gradient, at the surface is greater than at the 850 hPa level. Cyclones deepen at the surface in agreement with theoretical

models of cyclogenesis (Hoskins 1982). The 850 hPa wind is used here because it is an analyzed quantity strongly influenced by observations, and no additional calculations are needed to get it.

We use the geostrophic drag law to transform the wind at 850 hPa to a surface wind. These are half as strong as upper-air wind. (Figure 62). These surface winds are approximately 2 $\mathrm{m\,s^{-1}}$ less than the values obtained by Kristensen et al. (1999) for the central and eastern part of Denmark. However, if we introduce the correction factor 1.1 (see section 5.1.3) to account for the low temporal resolution, essentially the same extreme winds are obtained.

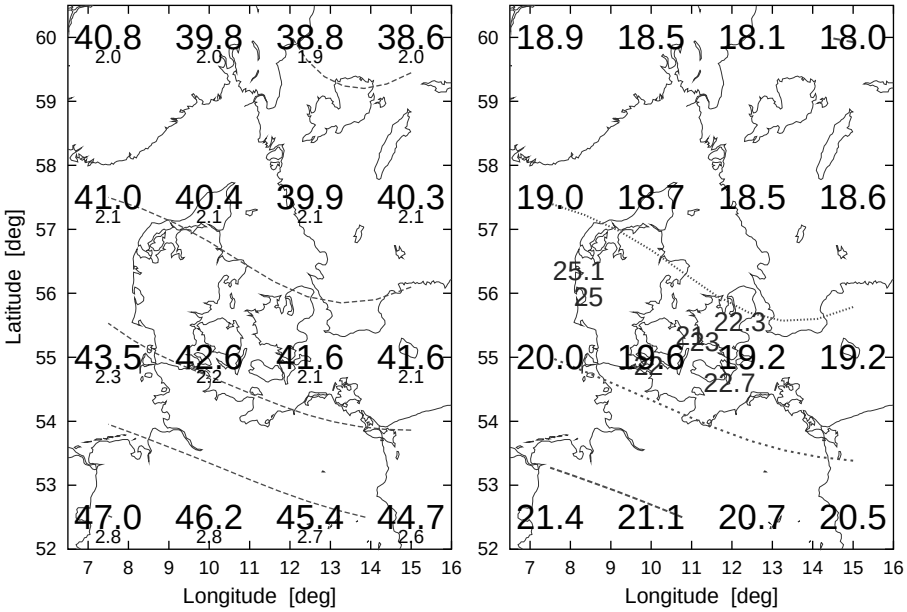

Figure 62. Left: Expected 50 year wind at 850 hPa and standard deviation. Right: Expected 50 year wind at 10 m above a flat surface with roughness length 5 cm obtained from the wind at 850 hPa using the geostrophic drag law. Estimates from observations (Kristensen et al. 1999) are written with smaller letters.

The trend from west to east agrees with the conclusion of Kristensen et al. (1999) that the west coast of Denmark experiences higher winds than the rest of the country. However, owing to the low resolution of the model, and perhaps enhanced by the smoothing to the 2.5 degree grid, the difference is very small. The difference between southern and northern Denmark is bigger in the model results. Unfortunately, Kristensen et al. (1999) did not analyze data in northern Jutland. The mean winds at the northern tip of Jutland are less than along the west and northwest coast. This might indicate that the extreme winds are also weaker.

5.1.6 Extremes of the geostrophic wind

Since the geostrophic drag law is being used to transform surface winds to the same conditions, we might as well start directly with the geostrophic wind. The extreme wind analysis is carried out for the geostrophic wind calculated from the surface pressure, p_s. Centered differences are used to calculate the pressure gradients. Only data at 00 UTC and 12 UTC for the 47 years 1953-1999 were analyzed.

The variation of the 50 year geostrophic wind calculated from the surface pressure (Figure 63) shows an expected decrease from west to east. The highest winds are predicted for the southern North Sea and the lowest winds for central Sweden and north-eastern Germany.

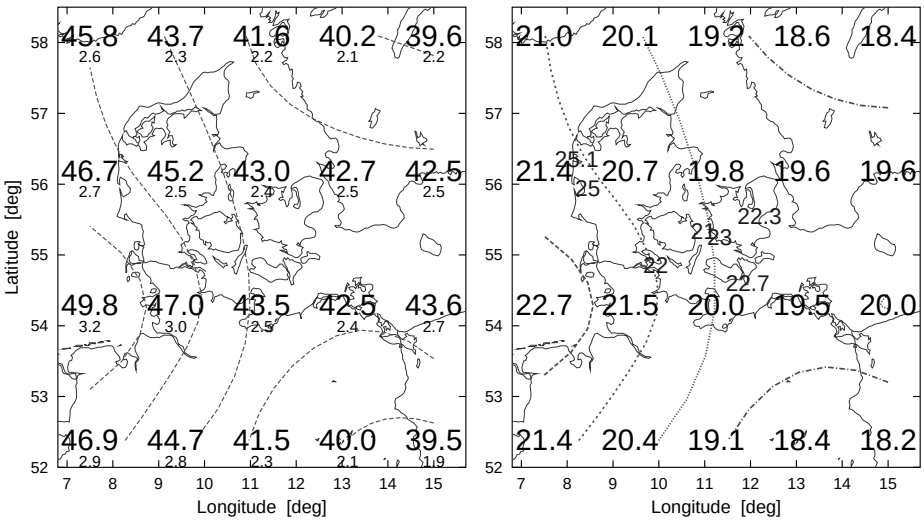

Figure 63. Expected 50 year geostrophic wind at sea level (left), and expected wind at 10 m above roughness 5 cm derived from it (right). Estimates from observations (Kristensen et al. 1999) are written with smaller letters.

The 50 year wind calculated from the surface pressure shows the expected decrease from west to east. The values are approximately 10 % less than the 22 $\mathrm{m\,s^{-1}}$ found by Kristensen et al. (1999) for most of Denmark. Unfortunately, we have no observations to verify that the highest winds are in the southern North Sea.

5.1.7 Conclusions

Unfortunately, it seems not possible to compare directly the extreme winds at 10 m of the NCEP/NCAR reanalysis with observed extreme winds over Denmark. The roughness length used in the NCEP/NCAR reanalysis at land points in Denmark is much to high. At some grid points — in the North Sea west of Denmark, perhaps in northern Germany — the expected 50 year return winds seem to compare well with other investigations based on surface measurements if the reanalysis values are increased by approximately 10–12 % owing to the low spatial and temporal resolution of the model data.

The analyses of the wind at 850 hPa and the geostrophic wind at 850 hPa and 1000 hPa (not shown here) yield very similar extreme winds of approximately 42 $\mathrm{m\,s^{-1}}$. The surface pressure data yields extreme geostrophic winds of ca. 45 $\mathrm{m\,s^{-1}}$ over Jutland. Transformed to a height of 10 m above a surface with roughness length 5 cm we obtain approximately 20 $\mathrm{m\,s^{-1}}$ for the 50 year return wind. This is approximately 10 % less than found by Kristensen et al. (1999) for most of Denmark. Considering the low temporal and spatial resolution of the model data such an underestimation could be expected.

A comparison with extreme wind analyses in other areas of the mid-latitudes would be necessary to find out if the underestimation of the “true” extreme winds by 10–12 % in the reanalysis data is generally valid. Compared to the resolution of the reanalysis model, and perhaps also compared to the size of most cyclones, Denmark is just too small to see big variations across the country.

Also further analysis is needed in order to see whether the directional distribution of extreme winds can be deduced faithfully from the reanalysis data. This would be necessary for the construction of Extreme Wind Climates used as input for WAsP Engineering.

In our opinion the analysis indicates that the best estimate for extreme winds in mid-latitudes can be obtained from geostrophic wind calculated from the surface pressure field. In areas with big variations of the surface height it is difficult to calculate correct horizontal pressure gradients. There it might be best to use an upper-air wind, e.g. at 850 hPa, with a greater correction factor than for the geostrophic wind at the surface.

5.2 Recalculation of extreme winds in Denmark

The basic design wind speed for Denmark was obtained in a previous EFP project called WAsP Engineering 1.0 DK (ENS–1363/07–0004) on basis of analysis of wind record from four masts: Skjern, Kegnæs, Sprogø and Tystofte. In that analysis WAsP was used to "clean" the data for the terrain surrounding terrain. Here WAsP Engineering is used for the same purpose in order to investigate whether the results differ significantly from the WAsP results presented in Kristensen et al. (2000).

This analysis was undertaken by Janne R. T. Banke, Brian R. Broe, Carsten Damberg and Birgitte Knudsen, four students from the University of Copenhagen, Department of Geophysics, under supervision by Jakob Mann. They used the same data as Kristensen *et al.* in order to be able to see the differences in using the flow model of WAsP Engineering instead of that of WAsP. There are many small differences between the two programs. The influence of roughness on the flow in WAsP is calculated by an adaptation of empirical knowledge of internal boundary layers after simple roughness changes. The mathematics of WAsP Engineering is quite different. Here the spatial roughness variations are decomposed into Fourier modes and for each mode the flow is calculated by an eddy diffusion model where the diffusion coefficient depends on the wave length. The resulting flow is calculated as a sum of the contribution from all the individual Fourier modes (Astrup, Jensen and Mikkelsen 1996, Astrup et al. 1997). Further, the roughness in WAsP is assumed to have constant value over water of $z_0 = 0.0002$ m. In WAsP Engineering the roughness over water depends on the wind speed just above the water and can be much larger at high wind speeds. Finally, the models of how the flow responds to orography are slightly different, but this aspect will probably be less important because the sites are relatively flat.

There are also differences in the way extrapolation to a 50 year return period is done. In the present analysis we use what is presented in section 5.1.2, while Kristensen et al. (2000) use a least squares fit in a Gumbel plot. Also the way the terrain is described is different in the two models. WAsP uses a polar, zooming grid while WAsP Engineering uses a Cartesian grid.

Banke, Broe, Damberg and Knudsen (2001) find that the calculation grid around the mast should be of the order of 10 km in each direction. Apart from the differences above they follow Kristensen (1999) in their analysis and the results are shown in table 7.

Table 7. Danish 50 year winds derived from WAsP and WAsP Engineering

		Skjern	Sprogø	Tystofte
	short period	1983–1997	1978–1997	1983–1997
	long period	1983–1998	1978–1998	1983–2000
U_{50} [m/s]	WAsP (short)	28.7 ± 2.5	20.4 ± 1.3	24.1 ± 1.9
	WAsP Engng (short)	29.2 ± 2.2	21.5 ± 1.4	25.6 ± 2.1
	WAsP Engng (long)	28.9 ± 2.1	21.4 ± 1.3	27.1 ± 2.3

The wind speeds in the table are *basic wind speeds* which is the 50-year wind speed under standard conditions, i.e. ten minute averages at the height 10 m over a uniform terrain with the roughness length 0.05 m. The data from Kegnæs have not been analyzed because the time series is only half the length of the others. The original values from Kristensen et al. (1999) are shown in the row "WAsP (short)" and should be compared with the row immediately below. The WAsP Engineering result are generally slightly larger, however, they are within the uncertainty of the original analysis. The inclusion of newer data does not change the numbers much except from the Tystofte site, which was hit by the Dec. 3. storm of 1999 (Mann and Hansen 2000). We believe that much of the (small) difference between the two analyses can be explained by variable water roughness

in WAsP Engineering. In WAsP Engineering the roughness is higher compared to WAsP for strong winds which leads to larger winds under standard conditions.

5.3 Estimation of extreme wind climates

The wind atlas used in WAsP contains a wind rose, giving the probabilities of wind in the n_s sectors, and Weibull A and k parameters for each sector. This is given for various heights z above flat, homogeneous terrain and roughness lengths z_0. An extreme wind atlas contains sectorwise information on strong winds pertaining to $z = 10$ m and $z_0 = 0.05$ m. The probabilities and Weibull parameters of the wind atlas are given at this height and roughness length, or they are easily derived through interpolation between the z's and z_0's in the wind atlas.

In Kristensen et al. (1999) the extreme wind atlas is given in terms of sectorwise Gumbel distribution for the friction velocity pressure, which is also used in WAsP Engineering.

It is desirable to be able to derive the parameters of the extreme wind atlas from the ordinary wind atlas. In Dekker and Pierik (1999) a connection has been established, but it is clear that pure mathematics will not do the job, additional assumptions have to be made.

An old engineering approach states that the 50 year wind is 5 times the average wind speed. Dekker and Pierik (1999) refines this estimate by taking into account not only the mean but also the shape of the distribution of the wind speeds. Here it is further refined to apply to the extreme winds for different direction sectors. It is important to emphasize that this is merely a refinement of the engineering formula $U_{50,\text{year}} = 5U_{\text{ave}}$.

Here the connection between a wind atlas and a WAsP Engineering wind atlas is described.

5.3.1 Mathematical preliminaries

The wind atlas The wind atlas is described by sector probabilities and Weibull parameters:

$$\sum_{i=1}^{n_s} p_i = 1\,; \quad A_i, k_i, \text{ for } i = 1, ..., n_s, \tag{151}$$

with the (10 minutes) mean winds in the ith sector distributed as

$$W(U) = P(\mathcal{U} < U) = 1 - \exp\left\{-\left(\frac{U}{A_i}\right)^{k_i}\right\}, \tag{152}$$

or, in terms of the probability density function,

$$w(U) = \frac{k_i - 1}{A_i}\left(\frac{U}{A_i}\right)^{k_i} \exp\left\{-\left(\frac{U}{A_i}\right)^{k_i}\right\}, \tag{153}$$

The nth non-central moment of the Weibull distribution is

$$m_n = \int_0^\infty U^n w(U)\mathrm{d}U = A^n \Gamma\left(1 + \frac{n}{k}\right) \tag{154}$$

The extreme wind atlas The extreme wind atlas is described in terms of the Gumbel distribution. Suppose x is the largest value of some atmospheric quantity over the *basis period* T_0, e.g. 50 years. Obviously, x varies from basis period to basis period and the distribution of x is often well approximated by the Gumbel distribution. The cumulative Gumbel distribution is

$$G(x) = \exp\left[-\exp\{-\alpha(x - \beta)\}\right], \tag{155}$$

and the corresponding probability density function is

$$g(x) = G'(x) = \alpha \mathrm{e}^{-\alpha(x-\beta)} \mathrm{e}^{-\mathrm{e}^{-\alpha(x-\beta)}}. \tag{156}$$

The parameter β is the most probable value of x and also the value of x which, on average, is exceeded once in the basis period T_0. The mean of the Gumbel distribution is slightly different from β:

$$m_G = \int_0^\infty x g(x) \mathrm{d}x \approx \int_{-\infty}^\infty x g(x) \mathrm{d}x = \beta + \gamma/\alpha, \tag{157}$$

where $\gamma \approx 0.577216$ is Euler's constant, and the variance is

$$\sigma_G^2 \approx \frac{\pi^2}{6\alpha^2} \tag{158}$$

Connection between Gumbel distribution of U and $\frac{1}{2}\rho u_*^2$ Suppose the distribution of yearly (or some other period, f.ex. 50 years) extreme 10 minute average wind speeds is given by the Gumbel distribution (155) with parameters α and β. What is the distribution of the friction pressure?

The friction pressure is given by

$$q = \frac{1}{2}\rho u_*^2 = \frac{1}{2}\rho \left(\frac{\kappa U}{\log(z/z_0)} \right)^2 \equiv C U^2, \tag{159}$$

where u_* is the friction velocity, ρ the density of air often taken to be 1.25 kg/m^3 and $\kappa \approx 0.4$ the von Karman konstant. Given that U is Gumbel distributed the cumulative distribution of the friction velocity pressure is

$$P(\mathcal{Q} < q) = G_2(q) \tag{160}$$

$$G_2(x) = \exp\left[-\exp\left\{ -A(\sqrt{x} - B) \right\} \right], \tag{161}$$

with the parameters

$$\begin{aligned} A &= \sqrt{C}\alpha = \sqrt{\frac{2}{\rho}} \frac{\log(z/z_0)}{\kappa} \\ B &= \beta/\sqrt{C} \end{aligned} \tag{162}$$

The mean of the G_2 distribution is

$$m_q \approx \frac{(AB + \gamma)^2 + \pi^2/6}{A^2} \tag{163}$$

and the variance is

$$\sigma_q^2 \approx \frac{60(AB+\gamma)^2\pi^2 + 11\pi^4 + 720(AB+\gamma)\zeta(3)}{90A^4}, \tag{164}$$

where ζ is the Riemann zeta function ($\zeta(3) \approx 1.202057$). Now the mean and the variance of the exact distribution (163) and (164) are matched with (157) and (158) and approximate Gumbel parameters α_q and β_q are derived:

$$\alpha_q = \frac{\pi}{\sqrt{6}\sigma_q} \tag{165}$$

and

$$\beta_q = m_q - \gamma/\alpha_q \tag{166}$$

To summarize, given the Gumbel parameters of the ten minutes average wind speed extreme value distribution we can calculate the corresponding parameters of the friction pressure Gumbel distribution.

5.3.2 The WAsP Engineering ewc file

The essential part of the extreme wind climate file `DK24.ewc`, which is a part of the *WAsP Engineering* distribution, looks as follows:

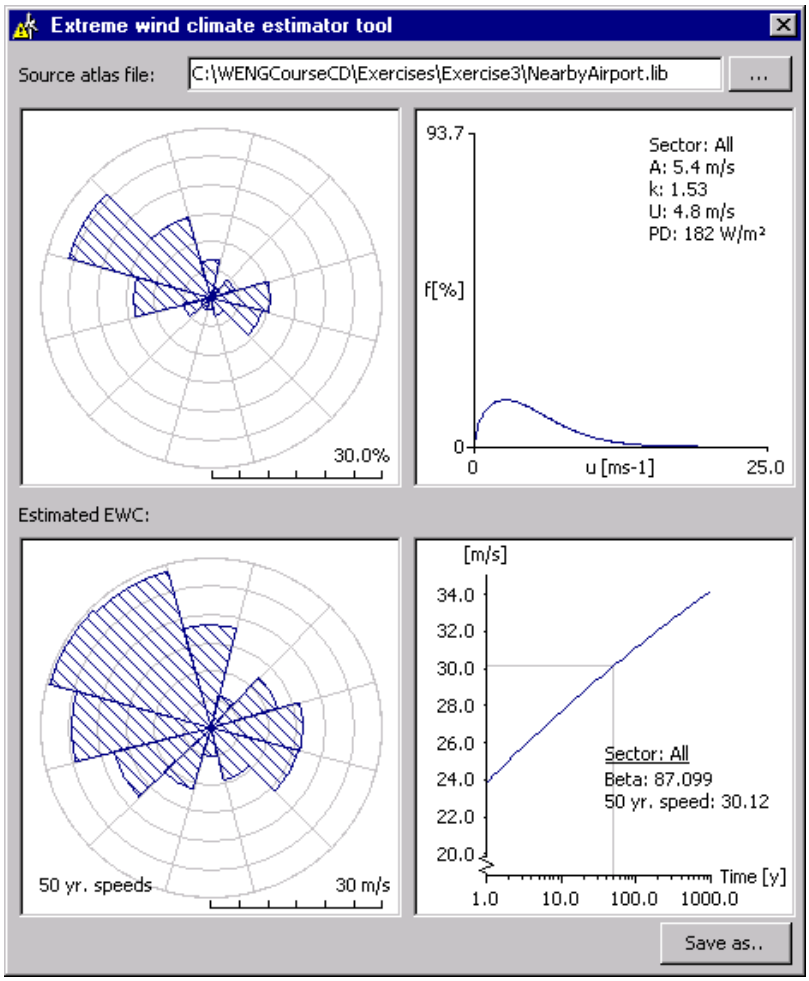

Figure 64. User interface of the EWCEstimator implemented in WAsP Engineering

```
<RveaExtremeWindClimate Height="10" Roughness="0.05" RecurrenceInterval="50" NumberSectors="12" LatitudeDegrees="56">
            <EwcSectorData CentreAngle="0"   WindSpeed="17.610" Alpha="0.1267"/>
            <EwcSectorData CentreAngle="30"  WindSpeed="17.002" Alpha="0.1207"/>
            <EwcSectorData CentreAngle="60"  WindSpeed="18.581" Alpha="0.1407"/>
            <EwcSectorData CentreAngle="90"  WindSpeed="19.223" Alpha="0.1417"/>
            <EwcSectorData CentreAngle="120" WindSpeed="17.323" Alpha="0.1077"/>
            <EwcSectorData CentreAngle="150" WindSpeed="19.113" Alpha="0.1453"/>
            <EwcSectorData CentreAngle="180" WindSpeed="20.668" Alpha="0.1657"/>
            <EwcSectorData CentreAngle="210" WindSpeed="21.132" Alpha="0.1677"/>
            <EwcSectorData CentreAngle="240" WindSpeed="21.918" Alpha="0.1833"/>
            <EwcSectorData CentreAngle="270" WindSpeed="22.754" Alpha="0.1960"/>
            <EwcSectorData CentreAngle="300" WindSpeed="22.779" Alpha="0.2020"/>
            <EwcSectorData CentreAngle="330" WindSpeed="19.764" Alpha="0.1553"/>
        </RveaExtremeWindClimate>
```

The `WindSpeed` in each sector refers to a ten minute average wind speed with a return period (also called recurrence interval) of 50 years, measured over a flat homogeneous terrain with a roughness length of 0.05 m at a height of 10 m above the terrain. There are 12 sectors and the latitude, on which the WAsP Engineering calculations are only weakly dependent, is 56°.

From the wind speed of each sector the 50 year friction velocity pressure β_q can be calculated from (159) using the standard density for sea level atmosphere of $\rho = 1.25\,\mathrm{kg/m^3}$. The parameter `Alpha` is α_q^{-1}.

5.3.3 The EWC Estimator

In Dekker and Pierik (1999) it is shown that if N independent measurements of U are given and if these are Weibull distributed with identical parameters A and k, then it is possible to calculate the exact distribution of the maximal value. This distribution is well approximated with a Gumbel distribution with the parameters

$$\beta \approx A(\ln N)^{1/k} \tag{167}$$

and

$$\alpha = \frac{k}{A}(\ln N)^{1-1/k} \tag{168}$$

The problem with these expressions is that it is difficult to estimate how many *independent* measurements are available. 50 years can be divided into 2.63×10^6 10 minute periods, but they are certainly not independent. Dekker and Pierik (1999) cites Berström and recommends multiplying the number of 10 minute periods with 0.438. This number may seem to be rather large. It implies that there are more than two independent 10 minute values *every hour*. One could expect only of the order one *per day* which corresponds roughly to the so-called synoptic time scale. However, we use Dekker and Pierik's (1999) value, which may be conservative, but it is based on empirical evidence.

In the EWC Estimator the degrees of freedom N are divided into the n_s sectors $N = \sum_{i=1}^{n_s} N_i$ where $N_i = p_i N$ (see eq. 151). Then the Gumbel parameters for each sector are calculated according to (167) and (168).

The parameters are then transformed to refer to friction velocity pressure as described in section 5.3.1.

The resulting extreme wind climate is generally conservative and examples of extreme wind speeds predicted from wind atlas files are compared to the proper wind speeds in table 8.

Table 8. The 50 year 10 minute average wind speed estimated from long time series directly (data) and estimated from a WAsP wind atlas file (lib file).

	Zaragoza Airport, Spain	Denmark, Eastern part
U_{50} [m/s] (data)	25.6	24
U_{50} (lib file)	30.1	23.2

References

Abild, J.: 1994, Application of the Wind Atlas Method to extremes of wind climatology, *Technical Report Risø–R–722(EN)*, Risø National Laboratory.

Adrian, G.: 1994, Zur Dynamik des Windfeldes über orographisch gegeliedertem Gelände, *Ber. Deutscher Wetterdienst* **188**, 1–142.

Adrian, G.: 1998, Das Karlsruher Atmospherische Mesoskalige Modell KAMM, *in* K. D. Beheng (ed.), *Prof. Dr. Franz Fiedler zum 60. Geburtstag*, Vol. 21, IMK, Karlsruhe, Germany.

Adrian, G. and Fiedler, F.: 1991, Simulation of unsteady wind and temperature fields over complex terrain and comparison with observations, *Beitr. Phys. Atmos.* **64**, 27–48.

Antonia, R. A. and Luxton, R. E.: 1971, The response of a turbulent boundary layer to a step change in surface roughness Part 1. Smooth to rough, *J. Fluid Mech.* **48**(4), 721–761.

Antonia, R. A. and Luxton, R. E.: 1972, The response of a turbulent boundary layer to a step change in surface roughness Part 1. Rough-to-smooth, *J. Fluid Mech.* **53**(4), 737–757.

Astrup, P., Jensen, N. O. and Mikkelsen, T.: 1996, Surface roughness model for lincom, *Technical Report RISØ-R–900(EN)*, Risø National Lab.

Astrup, P. and Larsen, S. E.: 1999, WAsP Engineering – Flow model for wind over land and sea, *Technical Report RISØ-R–1107(EN)*, Risø National Lab.

Astrup, P., Larsen, S. E., Rathmann, O. and Madsen, P. H.: 1999, WAsP Engineering – Wind flow modelling overf land and sea, *in* A. L. G. L. Larose and F. M. Livesey (eds), *Wind Engineering into the 21st Century*, Balkema, Rotterdam, pp. 179–184.

Astrup, P., Mikkelsen, T. and Jensen, N. O.: 1997, A fast model for mean and turbulent wind characteristics over terrain with mixed surface roughness, *Radiation Protection Dosimetry* **73**(1–4), 257–260.

Athanassiadou, M. and Castro, I. P.: 2001, Neutral flow over a series of rough hills: A laboratory experiment, *Boundary-Layer Meteorol.* **101**(1), 1–30.

Banke, J. R. T., Broe, B. R., Damberg, C. and Knudsen, B.: 2001, *Ekstremvindsanalysis*, Master's thesis, University of Copenhagen. Batchlor project, in Danish.

Barthelmie, R. J., Courtney, M. S., Lange, B., Nielsen, M., Sempreviva, A. M., Svenson, J. and Christensen, T.: 1998, Offshore wind resources at danish measuremnt sites, *Technical Report RISØ-I–1339(EN)*, Risø National Lab.

Batchelor, G. K.: 1953, *The theory of homogeneous turbulence*, Cambridge University.

Batchelor, G. K. and Proudman, I.: 1954, The effect of rapid distortion of a fluid in turbulent motion, *Quart. J. Mech. Appl. Math.* **7**, 83–103.

Bendat, J. S. and Piersol, A. G.: 1971, *Random data: Analysis and Measurement Procedures*, Wiley-Interscience.

Bendat, J. S. and Piersol, A. G.: 1986, *Random data: Analysis and Measurement Procedures*, 2 edn, Wiley-Interscience.

Britter, R. E., Hunt, J. C. R. and Richards, K. J.: 1981, Air flow over a two-dimensional hill: studies of velocity speed-up, roughness effects and turbulence, *Q. J. R. Meteorol. Soc.* **107**, 91–110.

Brown, R. D. and Swail, V. R.: 1991, Over-water gust factors, *Ocean Engng* **18**(4), 363–394.

Carruthers, D. and Hunt, J.: 1986, Velocity fluctuations near an interface between a turbulent region and a stably stratified layer, *J. Fluid Mech.* **165**, 475–501.

Charnock, H.: 1955, Wind stress on a water surface, *QJRMS* **81**, 639–640.

Comte-Bellot, G. and Corrsin, S.: 1971, Simple Eulerian time correlation of full- and narrow-band velocity signals in grid generated, 'isotropic' turbulence, *J. Fluid Mech.* **48**, 273–337.

Dekker, J. W. M. and Pierik, J. T. G.: 1999, European wind turbine standard II, *Technical Report ECN-C–99-073*, ECN.

Derbyshire, S. H. and Hunt, J. C. R.: 1993, Structure of turbulence in stably stratified atmospheric boundary layers; comparison of large eddy simulations and theoretical models, *in* S. D. Moobs and J. C. King (eds), *Waves and Turbulence in Stably Stratified Flows*, Clarendon, Oxford, pp. 23–59.

Dorman, J. L. and Sellers, P. J.: 1989, A global climatology of albedo, roughness length and stomatal-resistance for atmospheric general-circulation models as represented by the simple biosphere model (SiB), *J. Appl. Meteor.* **28**, 833–855.

ESDU International: 1982, *Characteristics of wind speed in the lower layers of the atmosphere near the ground: strong winds (neutral atmosphere)*, ESDU International, London.

ESDU International: 1985, *Characteristics of atmospheric turbulence near the ground. Part II: single point data for strong winds (neutral atmosphere)*, ESDU International, London.

Frank, H. P.: 1996, A simple spectral model for the modification of turbulence in flow over gentle hills, *Boundary-Layer Meteorol.* **79**(4), 345–373.

Frank, H. P.: 2001, Extreme winds over denmark from the NCEP/NCAR reanalysis, *Technical Report Risø–R–1238(EN)*, Risø National Laboratory.

Garratt, J. R.: 1977, Review of drag coefficients over oceans and continents, *Monthly Weather Review* **105**, 915–929.

Geernaert, G. L.: 1987, On the importance of the drag coefficient in air-sea interactions, *Dynamics of Atmospheres and Oceans* **11**, 19–38.

Grigoriu, M.: 1993, On the spectral representation method in simulation, *Probabilistic Engineering Mechanics* **8**, 75–90.

Gumbel, E. J.: 1958, *Statistics of Extremes*, Columbia University Press.

Højstrup, J.: 1981, A simple model for the adjustment of velocity spectra in unstable conditions downstream of an abrupt change in roughness and heat, *Boundary-Layer Meteorol.* **21**, 341–356.

Højstrup, J., Larsen, S. E. and Madsen, P. H.: 1990, Power spectra of horizontal wind components in the neutral atmospheric boundary layer, *in* N. O. Jensen, L. Kristensen and S. E. Larsen (eds), *Ninth Symposium on Turbulence and Diffusion*, American Meteorological Society, pp. 305–308.

Hoskins, B. J.: 1982, The mathematical theory of frontogenesis, *Ann. Rev. Fluid Mech.* **14**, 131–151.

Hunt, J. C. R.: 1973, A theory of turbulent flow round two-dimensional bluff bodies, *J. Fluid Mech.* **61**, 625–706.

Hunt, J. C. R.: 1984, Turbulence structure in thermal convection and shear-free boundary layers, *J. Fluid Mech.* **138**, 161–184.

Hunt, J. C. R. and Carruthers, D. J.: 1990, Rapid distortion theory and the 'problems' of turbulence, *J. Fluid Mech.* **212**, 497–532.

Jackson, P. S. and Hunt, J. C. R.: 1975, Turbulent flow over a low hill, *QJRMS* **101**, 929–955.

Jensen, M. and Franck, N.: 1970, The climate of strong winds in Denmark, *Technical report*, Danish Technical Press.

Jensen, N. O., Petersen, E. L. and Troen, I.: 1984, Extrapolation of mean wind statistics with special regard to wind energy applications, *Technical Report WCP-86*, World Meteorol. Organ., Geneva.

Kaimal, J. C. and Finnigan, J. J.: 1994, *Atmospheric Boundary Layer Flows, Their Structure and Measurement*, Oxford University Press, New York.

Kaimal, J. C., Wyngaard, J. C., Izumi, Y. and Coté, O. R.: 1972, Spectral charcteristics of surface-layer turbulence, *Q. J. R. Meteorol. Soc.* **98**, 563–589.

Kalnay, E., Kanamitsu, M., Kistler, R., Collins, W., Deaven, D., Gandin, L., Iredell, M., Saha, S., White, G., Woollen, J., Zhu, Y., Leetmaa, A., Reynolds, R., Chelliah, M., Ebisuzaki, W., Higgins, W., Janowiak, J., Mo, K. C., Ropelewski, C., Wang, J., Jenne, R. and Joseph, D.: 1996, The NCEP/NCAR 40-year reanalysis project, *Bull. Amer. Meteor. Soc.* **77**, 437–471.

Kim, J. and Hussain, F.: 1993, Propagation velocity of pertubations in turbulent channel flow, *Phys. Fluids A* **5**(3), 695–706.

Koopmans, L. H.: 1974, *The Spectral Analysis of Time Series*, Academic Press.

Kristensen, L.: 1999, The perennial cup anemometer, *Wind Energy* **2**, 59–75.

Kristensen, L. and Kirkegaard, P.: 1987, Puff kinematics, *Technical Report R–548*, Risø National Laboratory.

Kristensen, L., Rathmann, O. and Hansen, S. O.: 1999, Extreme winds in Denmark, *Technical Report Risø–R–1068(EN)*, Risø National Laboratory.

Kristensen, L., Rathmann, O. and Hansen, S. O.: 2000, Extreme winds in Denmark, *J. Wind Eng. Ind. Aerodyn.* **87**(2–3), 147–166.

Landau, L. D. and Lifshitz, E. M.: 1987, *Fluid Mechanics*, Pergamon Press.

Lesieur, M.: 1987, *Turbulence in fluids*, Martinus Nijhoff Publishers.

Mann, J.: 1992, Investigation of atmospheric low-frequency turbulence over the ocean, *Technical Report I–634(EN)*, Risø National Laboratoty.

Mann, J.: 1994, The spatial structure of neutral atmospheric surface-layer turbulence, *J. Fluid Mech.* **273**, 141–168.

Mann, J.: 1998, Wind field simulation, *Prob. Engng. Mech.* **13**(4), 269–282.

Mann, J.: 2000, The spectral velocity tensor in moderately complex terrain, *J. Wind Engineering and Industrial Aerodynamics* . To appear in.

Mann, J., Astrup, P., Kristensen, L., Rathmann, O., Madsen, P. H. and Heathfield, D.: 2000, WAsP Engineering DK, *Technical Report R–1179(EN)*, Risø National Laboratoty.

Mann, J. and Hansen, S. O.: 2000, Én storm gør ingen norm, *Vejret* **82**, 28 – 34. In Danish.

Mann, J., Kristensen, L. and Courtney, M. S.: 1991, The great belt coherence experiment – a study of atmospheric turbulence over water, *Technical Report R–596*, Risø National Laboratory.

Mann, J., Kristensen, L. and Jensen, N. O.: 1998, Uncertainties of extreme winds, spectra, and coherences, *in* A. Larsen and S. Esdahl (eds), *Bridge Aerodynamics*, COWI, A. A. Balkema, Rotterdam, pp. 49–56.

Maxey, M. R.: 1982, Distortion of turbulence in flows with parallel streamlines, *J. Fluid Mech.* **124**, 261–282.

Mizuno, T. and Panofsky, H. A.: 1975, The validity of Taylor's hypothesis in the atmospheric surface layer, *Boundary-Layer Meteorol.* **9**, 375–380.

NDP: 1998, *Acts, regulations and provisions for the petroleum activities, Vol. 2,*, Norwegian Petroleum Directorate.

Panofsky, H. A. and Dutton, J. A.: 1984, *Atmospheric Turbulence*, John Wiley & Sons, New York.

Panofsky, H. A., Larko, D., Lipschutz, R., Stone, G., Bradley, E. F., Bowen, A. J. and Højstrup, J.: 1982, Spectra of velocity components over complex terrain, *Q. J. R. Meteorol. Soc.* **108**, 215–230.

Press, W. H., Flannery, B. P., Teukolsky, S. A. and Vetterling, W. T.: 1992, *Numerical Recipes*, 2nd edn, Cambridge University Press.

Savill, A. M.: 1987, Recent developments in rapid-distortion theory, *Ann. Rev. Fluid Mech.* **19**, 531–575.

Shinozuka, M. and Deodatis, G.: 1991, Simulation of stochastic processes by spectral representation, *Appl. Mech. Rev.* **44**(4), 191–203.

Shinozuka, M. and Deodatis, G.: 1996, Simulation of multi-dimensional gaussian stochastic fields by spectral representation, *Appl. Mech. Rev.* **49**(1), 29–53.

Shinozuka, M. and Jan, C.-M.: 1972, Digital simulation of random processes and its applications, *Journal of Sound and Vibration* **25**(1), 111–128.

Simiu, E. and Scanlan, R. H.: 1996, *Wind Effects on Structures, 3. ed.*, John Wiley & Sons.

Taylor, P. A. and Teunissen, H. W.: 1983, Askervein '82: Report on the September/October 1982 experiment to study boundary-layer flow over Askervein, South Uist, *Technical Report Research Report MSRB-83-8*, Atmospheric Environment Service, Toronto, Canada.

Taylor, P. A. and Teunissen, H. W.: 1985, The Askervein hill project: Report on the Sept./Oct. 1983 main field experiment, *Technical Report Research Report MSRB-84-6*, Atmospheric Environment Service, Toronto, Canada.

Townsend, A. A.: 1972, Flow in a deep turbulent boundary layer over a surface distorted by water waves, *J. Fluid Mech.* **55**(4), 719–735.

Townsend, A. A.: 1976, *The Structure of Turbulent Shear Flow*, 2nd edn, Cambridge University Press.

Townsend, A. A.: 1980, The response of sheared turbulence to additional distortion, *J. Fluid Mech.* **98**, 171–191.

Troen, I. and de Baas, A.: 1986, A spectral diagnostic model for wind flow simulation in complex terrain, *Proceedings of the European Wind Energy Association Conference & Exhibition*, Rome, pp. 37–41.

Troen, I. and Petersen, E. L.: 1989, *European Wind Atlas*, Risø National Laboratory.

Walmsley, J. L. and Taylor, P. A.: 1996, Boundary-layer flow over topography: Impacts of the Askervein study, *Boundary-Layer Meteorol.* **78**, 291–320.

Wilson, D. K.: 1998, On the propagation of turbulence spectral/correlation models to sound propagation in the atmosphere, *Eighth International Symposium on Long-Range Sound Propagation*, pp. 296–312.

Wood, N.: 2000, Wind flow over complex terrain: A historical perspective and the prospect for large-eddy modelling, *BLM* **96**(1–2), 11–32.

Bibliographic Data Sheet **Risø–R–1356(EN)**

Title and author(s)

WAsP Engineering 2000

Jakob Mann, Søren Ott, Bo Hoffmann Jørgensen & Helmuth P. Frank

ISBN	ISSN
87–550–3094–7; 87–550–3095–5 (Internet)	0106–2840

Dept. or group	Date
Wind Energy	August 2, 2002

Groups own reg. number(s)	Project/contract No.
1105049–01	ENS–1363/00–0015

Pages	Tables	Illustrations	References
90	8	64	82

Abstract (Max. 2000 char.)

This report summarizes the findings of the EFP project *WAsP Engineering Version 2000*. The main product of this project is the computer program *WAsP Engineering* which is used for the estimation of extreme wind speeds, wind shears, profiles, and turbulence in complex terrain. At the web page `http://www.waspengineering.dk` more information of the program can be obtained and a copy of the manual can be downloaded.
The reports contains a complete description of the turbulence modelling in moderately complex terrain, implemented in *WAsP Engineering*. Also experimental validation of the model together with comparison with spectra from engineering codes is done.
Some shortcomings of the linear flow model LINCOM, which is at the core of WAsP Engineering, is pointed out and modifications to eliminate the problem are presented.
The global database of meteorological “reanalysis” data from NCAP/NCEP are used to estimate the extreme wind climate around Denmark. Among various alternative physical parameters in the database, such as surface winds, wind at various pressure levels or geostrophic winds at various heights, the surface geostrophic wind seems to give the most realistic results. Because of spatial filtering and intermittent temporal sampling the 50 year winds are underestimated by approximately 12%. Whether the method applies to larger areas of the world remains to be seen.
The 50 year winds in Denmark is estimated from data using the flow model in *WAsP Engineering* and the values are approximately 1 m/s larger than previous analysis (Kristensen et al. 2000). A tool is developed to estimate crudely an extreme wind climate from a WAsP lib file.

Descriptors

COMPLEX TERRAIN; FLOW MODELS; SEAS; TURBULENCE; VELOCITY; W CODES; WIND; WIND LOADS

Available on request from:
Information Service Department, Risø National Laboratory
(Afdelingen for Informationsservice, Forskningscenter Risø)
P.O. Box 49, DK–4000 Roskilde, Denmark
Phone (+45) 46 77 46 77, ext. 4004/4005 · Fax (+45) 46 77 40 13
E-mail: risoe@risoe.dk